AKAP79 enables calcineurin to directly suppress protein kinase A activity

Timothy W. Church[a], Parul Tewatia[b,c], Saad Hannan[a], João Antunes[b], Olivia Eriksson[b], Trevor G. Smart[a], Jeanette Hellgren Kotaleski[b,c], Matthew G. Gold[a,1]

[a]Department of Neuroscience, Physiology & Pharmacology, University College London, Gower Street, LONDON, WC1E 6BT, UK

[b]Science for Life Laboratory, School of Electrical Engineering and Computer Science, KTH Royal Institute of Technology, Stockholm, Sweden

[c]Department of Neuroscience, Karolinska Institute, Stockholm, Sweden

[1]Correspondence: m.gold@ucl.ac.uk

Abstract

Interplay between the second messengers cAMP and Ca^{2+} is a hallmark of dynamic cellular processes. A common motif is the opposition of the Ca^{2+}-sensitive phosphatase calcineurin and the major cAMP receptor, protein kinase A (PKA). Calcineurin dephosphorylates sites primed by PKA to bring about changes including synaptic long-term depression (LTD). AKAP79 supports signaling of this type by anchoring PKA and calcineurin in tandem. In this study, we discovered that AKAP79 increases the rate of calcineurin dephosphorylation of type II PKA regulatory subunits by an order of magnitude. Fluorescent PKA activity reporter assays, supported by kinetic modeling, show how AKAP79-enhanced calcineurin activity enables suppression of PKA without altering cAMP levels by increasing PKA catalytic subunit capture rate. Experiments with hippocampal neurons indicate that this mechanism contributes towards LTD. This non-canonical mode of PKA regulation may underlie many other cellular processes.

Introduction

Cyclic adenosine monophosphate (cAMP) and Ca^{2+} are ancient second messengers that are fundamental to the regulation of many dynamic cellular processes including synaptic plasticity (Huang et al., 1994), heart contraction (Bers et al., 2019), and glycogen metabolism (Roach et al., 2012). Crosstalk between the two second messengers is a common feature of cellular signaling. For example, cAMP can enhance cytosolic Ca^{2+} entry by triggering phosphorylation of key ion channels (Qian et al., 2017; Schmitt et al., 2003) by its major intracellular receptor cAMP-dependent protein kinase, also known as Protein Kinase A (PKA). Similarly, Ca^{2+} can regulate cAMP levels by altering activities of both phosphodiesterases (Baillie et al., 2019) and adenylyl cyclases (Qi et al., 2019). At the receptor level, a common signaling motif is the opposition of PKA and the highly-abundant Ca^{2+}-sensitive phosphatase calcineurin (CN), with CN triggering cellular changes by removing phosphate from substrates primed by PKA. Notable examples of this motif are the regulation of postsynaptic substrates including AMPA-type glutamate receptors in the induction of long-term depression (LTD) of synaptic strength (Bear, 2003), and control of NFAT nuclear localization in immune responses (Hogan, 2017). According to current consensus, in these cases CN dephosphorylates substrates without any requirement for directly altering PKA activity (Dittmer et al., 2014; Lu et al., 2011; Tunquist et al., 2008; Weisenhaus et al., 2010; Zhang & Shapiro, 2016). This implies that energetically-costly futile cycles of phosphate addition and removal by PKA and CN must persist to maintain dephosphorylated substrate. It would be more logical for PKA activity to be switched off when CN is activated during substrate dephosphorylation. Uncovering the mechanism to achieve this is the focus of this study.

Recent years have seen renewed interest in mechanisms for regulating the release and re-capture of PKA catalytic subunits (Bock et al., 2020; Gold, 2019; Zhang et al., 2020), including new data that hint at how CN might directly suppress PKA activity. PKA is comprised of regulatory subunit dimers that bind and sequester PKA catalytic (C) subunits in an inhibited state (Taylor et al., 2019). PKA regulatory subunits are classified into type I subunits (RIα and RIβ) that are predominantly cytosolic, and type II subunits (RIIα and RIIβ) that co-sediment with membranes (Gold, 2019). The regulatory subunit inhibitor sequence (IS) is phosphorylated upon association with C subunits for RII but not RI subunits, which bear alanine in place of serine in the phospho-acceptor site (S98 in RIIα). Quantitative immunoblotting and mass spectrometry (MS) have recently shown that PKA regulatory subunits – and particularly RII subunits – greatly outnumber PKA C subunits (Aye et al., 2010; Walker-Gray et al., 2017) throughout the body. In addition, Zhang and co-workers (Zhang et al., 2015) have extended earlier observations (Rangel-Aldao & Rosen, 1976) to quantify differences in the rate of C subunit binding to RII subunits either

phosphorylated (pRII) or dephosphorylated at the IS. Remarkably, the k_{on} rate for C subunit association is ~50 times faster for dephosphorylated RII than pRII (Zhang et al., 2015) (***Figure 1***A). In theory, rapid dephosphorylation of RII subunits by CN could directly suppress PKA activity by increasing the rate of C subunit capture thereby reducing the proportion of C subunits that are dissociated (Buxbaum & Dudai, 1989; Isensee et al., 2018; Ogreid & Doskeland, 1981; Stemmer & Klee, 1994; Zhang et al., 2015; Zhang et al., 2012). While recent observations concerning PKA subunit stoichiometry and pRII/RII binding kinetics support this notion, isolated pRII is a low affinity substrate for CN with a half-maximal substrate concentration (K_m) above 20 µM (Blumenthal et al., 1986; Perrino et al., 1992; Stemmer & Klee, 1994). Therefore, pRII dephosphorylation by CN would not be expected to occur to a meaningful degree at physiological concentrations in the absence of an additional factor.

Anchoring proteins support signal transduction by elevating effective local concentrations of signaling proteins, and therefore theoretically an AKAP might support pRII dephosphorylation by CN in cells (Gildart et al., 2020). A-kinase anchoring protein 79 (AKAP79; rodent ortholog AKAP150, gene name AKAP5) is a prototypical mammalian anchoring protein with several features that indicate it could operate in part by increasing the effective protein concentration of pRII subunits for CN. AKAP79 can simultaneously anchor both CN and PKA (Coghlan et al., 1995). It contains an amphipathic anchoring helix (Gold et al., 2006; Kinderman et al., 2006) for binding RII subunits, and a short linear 'PIAIIIT' CN anchoring motif (Dell'Acqua et al., 2002; Li et al., 2012). The two anchoring sites are separated by only ~50 amino acids in the primary sequence within the C-terminus of AKAP79 (***Figure 1***B). AKAP79 is localized in dendritic spines where it is required for anchoring RII subunits (Tunquist et al., 2008). The anchoring protein is necessary for both induction of long-term depression (LTD) of CA3-CA1 hippocampal synapses (Lu et al., 2008; Tunquist et al., 2008; Weisenhaus et al., 2010), and for CN-mediated dephosphorylation of NFAT (Kar et al., 2014; Murphy et al., 2014) – both processes that are driven by CN dephosphorylation of sites primed by PKA. Despite these characteristics, the possibility that AKAP79 could support pRII dephosphorylation by CN has been disregarded perhaps because paradoxically AKAP79 acts as a weak inhibitor for CN dephosphorylation of 20-mer peptides corresponding to the phosphorylated RII IS (Coghlan et al., 1995; Kashishian et al., 1998). We reasoned that these assays could be misleading since peptide substrates are not subject to anchoring alongside CN that occurs for full-length RII subunits. To resolve this issue, in this study we measured how AKAP79 alters CN activity towards full-length pRII subunits. We went on to determine if AKAP79 can reduce the fraction of dissociated C subunits in concert with CN using fluorescence-based assays supported by kinetic modeling, before substantiating our observations in hippocampal neurons.

Results

AKAP79 enables CN to efficiently dephosphorylate RII subunits at physiological concentrations

We set out to determine whether AKAP79 can increase CN dephosphorylation of full-length RII subunits phosphorylated at the IS. Using purified proteins (***Figure 1-figure supplement 1***), we compared ^{32}P release from either pRIIα (***Figure 1***C) or pRIIβ (***Figure 1***D). Thirty second reactions were initiated by addition of excess Ca^{2+}/calmodulin (CaM) to 10 nM CN and 400 nM pRII subunits. For pRIIα without AKAP79, phosphate was released from only 0.36±0.13 % of the subunits (black, ***Figure 1***C). Inclusion of full-length AKAP79 in the reaction mix increased phosphate release by 12.4-fold (p = 7.4x10^{-6}) to 4.52±0.26 % pRIIα subunits (light blue, ***Figure 1***C). Removing the PIAIIIT anchoring sequence in AKAP79 (ΔCN) returned dephosphorylation to a baseline level of 0.26±0.06 % (grey, ***Figure 1***C), consistent with a mechanism in which anchoring of CN adjacent to pRII subunits enhances the rate of dephosphorylation. Similar results were obtained for pRIIβ, with addition of AKAP79 increasing phosphate release 16.3-fold (p = 3.0x10^{-6}) from 0.34±0.13 % (black, ***Figure 1***D) to 5.49±0.17 % (dark blue, ***Figure 1***D). Ablating the CN anchoring site in AKAP79 also reduced phosphorylation to a baseline level of 0.2±0.02 % for this isoform (grey, ***Figure 1***D).

We next measured CN activity towards pRII over a range of pRII concentrations. We compared activity towards pRII subunits alone or in complex with a fragment of AKAP79 ($AKAP79_{c97}$) encompassing positions 331-427 that includes the CN and RII subunit anchoring sites. Working with this stable highly-expressed construct enabled us to purify sufficient quantities of pRIIα-$AKAP79_{c97}$ and pRIIβ-$AKAP79_{c97}$ complexes (***Figure 1-figure supplement 1***C & D) to sample concentrations up to 5 μM. In complex with $AKAP79_{c97}$, both pRIIα and pRIIβ acted as relatively high affinity substrates of CN. pRIIα-$AKAP79_{c97}$ (light blue, ***Figure 1***E) was dephosphorylated with a half-maximal concentration (K_m) of 1.36±0.16 μM and turnover number (k_{cat}) of 0.45±0.02 s^{-1}, and pRIIβ-$AKAP79_{c97}$ with K_m = 0.74±0.12 μM and k_{cat} = 0.24±0.01 s^{-1}. As expected, in the absence of the anchoring protein, pRIIα and pRIIβ subunits served as low affinity substrates for CN (black lines, ***Figure 1***E & F). For both isolated pRII isoforms, the relationship between phosphatase activity and pRII concentration was linear up to 20 μM (***Figure 1-figure supplement 2***) – the highest concentration tested – indicative of a K_m of greater than 20 μM. CN activity was very low (<0.03 s^{-1}) at concentrations of 5 μM pRII or lower. This is consistent with earlier studies that reported a K_m of 94 μM for CN dephosphorylation of a phosphorylated 19-mer peptide derived from the RIIα IS (Stemmer & Klee, 1994). We also compared CN activity towards para-nitrophenylphosphate (pNPP) and a peptide corresponding to the isolated phosphorylated RII inhibitor sequence (sequence DLDVPIPGRFDRRVpSVAAE) with and without variants of $AKAP79_{c97}$ (***Figure***

1-figure supplement 3). WT AKAP79$_{c97}$ enhanced CN activity towards pNPP by ~ 65 %, and reduced its activity towards pRII phosphopeptide by ~ 50 %, consistent with previous reports that AKAP79 acts as a weak inhibitor of CN activity towards this phosphopeptide (Coghlan et al., 1995; Kashishian et al., 1998). Enhanced CN activity towards pNPP in the presence of PxIxIT-type motifs that have the opposite effect on phosphopeptide dephosphorylation has also been observed previously (Grigoriu et al., 2013). Overall, our data are consistent with a mechanism in which AKAP79 enhances CN dephosphorylation of full-length RII subunits by increasing effective substrate concentration rather than by altering the inherent catalytic activity of the phosphatase.

To put our kinetic parameters for pRII dephosphorylation into a physiological context, we set out to determine accurate protein concentrations for PKA subunits in the CA1 neuropil where Schaffer collaterals from the CA3 region synapse onto CA1 dendrites (***Figure 2***A). These synapses are a leading prototype for understanding forms of LTD driven by CN following PKA priming (Bear, 2003). We collected hippocampal slices from 18-day old male Sprague-Dawley rats before micro-dissecting CA1 neuropil sections (***Figure 2***B). Following homogenization, concentrations of C, RIIα, RIIβ, and RI subunits in the extracted protein were determined using quantitative immunoblotting by running extracts (n=5) alongside reference concentrations of purified PKA subunits (***Figure 2***C, ***Figure 2-figure supplement 1***) (Walker-Gray et al., 2017). We found that RIIα was by far the most predominant PKA subunit in the CA1 neuropil, accounting for 0.32±0.029 % total protein content compared to 0.032±0.003 % for C subunits, 0.041±0.014 % for RI, and 0.06±0.006 % for RIIβ. These numbers equate to a 9.4-fold higher molar abundance of RIIα subunits (light blue, ***Figure 2***D) relative to C subunits with RI and RIIβ present at similar levels to C subunits. The predominance of the RIIα subunit is consistent with a previous imaging study of rodent hippocampus (Weisenhaus et al., 2010). Assuming that protein accounts for 8 % of total rat brain weight (Clouet & Gaitonde, 1956), we estimated RII subunit concentrations of 5.9 μM (RIIα) and 1.03 μM (RIIβ). These values fall within the range where CN efficiently dephosphorylates pRII only in the presence of AKAP79 (***Figure 1***E & F). Taken together our data therefore indicate that AKAP79 greatly enhances CN activity towards phosphorylated RII subunits at physiological concentrations.

AKAP79 enables calcineurin to suppress type II PKA activity

Given that AKAP79 supports rapid pRII dephosphorylation by CN, we hypothesized that the AKAP could enable CN to directly reduce the fraction of dissociated C subunits in mixtures of RII and C subunits. To test this hypothesis, we utilized purified A-kinase activity reporter 4 (AKAR4) (***Figure 3***A). PKA phosphorylation at threonine within the reporter's central 'LRRA**T**LVD' motif leads to a

conformational change that increases FRET efficiency between the terminal fluorescent proteins (***Figure 3***A)(Depry et al., 2011). All AKAR4 experiments were performed using purified protein mixtures in 96-well plates. For each recording, three baseline 520/485 nm emission ratios were measured prior to injection of ATP and the desired concentration of cAMP into the protein mixture to initiate phosphorylation. Emission ratios were collected once every 5 seconds (s) thereafter. In calibration experiments with AKAR4 and different concentrations of C subunit only (***Figure 3-figure supplement 1***A), we found that the initial rate of AKAR4 phosphorylation had a close to linear relationship to C subunit concentration up to 400 nM C subunit (***Figure 3-figure supplement 1***B). Full AKAR4 phosphorylation increased the emission ratio by 72 % (***Figure 3-figure supplement 1***A), consistent with previous studies (Depry et al., 2011). Importantly, supplementing these reactions with 1.5 μM activated CN had no detectable effect on AKAR4 phosphorylation rates, indicating that the phosphatase cannot efficiently dephosphorylate the reporter (Figure 3-***figure supplement 1***C & D). In comparison, supplementation with 1.5 μM PP1 reduced the phosphorylation rate by ~ 7-fold (***Figure 3-figure supplement 2***A & B). Phosphatase assays using pre-phosphorylated AKAR4 confirmed that CN exhibits very limited activity towards the reporter (***Figure 3-figure supplement 2***C & D), such that the reporter is well suited for experiments focusing on direct suppression of PKA activity by CN.

Next, we assembled purified protein mixtures with the aim of mimicking signaling involving PKA, CN, and AKAP79 in CA1 dendritic spines. RIIα, RIIβ, and C subunits were included at concentrations determined in CA1 neuropil extracts (**Figure 2)**. CaM was added at a molar excess of 5 μM, CN at 1.5 μM (Goto et al., 1986), and $AKAP79_{c97}$ – when included – at half the concentration of total RII subunits (summarized in ***Figure 3***B). RI subunits were omitted since they are not thought to be present in dendritic spines (Ilouz et al., 2017; Tunquist et al., 2008), and because the RI inhibitor site is not phosphorylated so cannot be regulated by CN. We first monitored AKAR4 phosphorylation in reactions containing RIIα, RIIβ, C, and CaM (black, ***Figure 3***C). Increasing the concentration of cAMP injected alongside ATP raised rates of AKAR4 phosphorylation as expected (black bars, ***Figure 3***D). Supplementing the reactions with CN led to small but consistent decreases in the rate of AKAR4 phosphorylation at all cAMP concentrations (blue, ***Figure 3***C & D). Rates were determined between 30-90 s in the linear early phase that followed a brief ~15 second delay, with the exception of the lowest two cAMP concentrations (0 & 100 nM), where relatively slow rates were calculated between 30-330 s. Additional supplementation with $AKAP79_{c97}$ markedly decreased the rate of AKAR4 phosphorylation (red, ***Figure 3***C). For example, with 1 μM cAMP activation, addition of both CN and the AKAP reduced the initial rate of AKAR4 phosphorylation by 2.8-fold from 18.9±0.6 to 6.7±0.8 % per minute (p = 0.0007, black and red bars, ***Figure 3***D). To confirm that AKAP79 enables CN to suppress PKA activity by anchoring it alongside RII

subunits, we investigated the effect of removing either the CN (positions 337-343) or PKA (391-400) anchoring sites. At 1 µM cAMP activation, addition of wild-type (WT) $AKAP79_{c97}$ (red, ***Figure 3***E & F) reduced the initial rate of AKAR4 phosphorylation by 2.06-fold (p = 2.7 x 10^{-11}) compared to supplementation with only CN (blue). Similar AKAR4 responses were obtained when either the AKAP was omitted altogether (blue, ***Figure 3***E & F), or if either the CN (purple) or PKA (orange) anchoring sites in the AKAP were removed. Overall, these AKAR4 measurements reveal that AKAP79 enables CN to robustly decrease type II PKA activity by anchoring the two enzymes together.

Mechanistic basis of PKA suppression by calcineurin and AKAP79

We next aimed to quantify how AKAP79 and CN changed the fraction of free C subunits in our reaction mixtures. To estimate this, we cross-referenced rates of AKAR4 phosphorylation recorded in the 'spine mimic' reaction mixtures (***Figure 3***C & E) to the reference curve (r = 0.998) obtained with only C subunits (***Figure 3-figure supplement 1***B). We focused on determining free C subunit concentrations during the early period of linear change (30-90 s for cAMP concentrations of 0.2 µM and above) where we assume the underlying kinetics are close to equilibrium. We calculated free C subunit concentrations following this approach using all available data between 0 to 2 µM cAMP (***Figure 3-figure supplement 1***E). The calculated proportion of C subunits that are dissociated at different cAMP concentrations are shown for type II PKA + CaM either alone (black, ***Figure 4***A), with CN (blue, ***Figure 4***B), or with both CN and $AKAP79_{c97}$ (red, ***Figure 4***C). Together, AKAP79 and CN reduced the proportion of free C subunits at equilibrium across the cAMP concentration range including from 47.8±1.5 to 20.2±0.8 % at 1 µM cAMP, and from 65.7±1.1 to 33.2±3.3 % at 2 µM cAMP (***Figure 4***A & C). The effect of adding CN alone was limited (***Figure 4***B), consistent with the much lower activity of the phosphatase towards pRII subunits in the low micromolar range (***Figure 1***E & F).

To understand at a deeper level how CN and AKAP79 reduce the fraction of free C subunits, we updated and extended a kinetic model (Buxbaum & Dudai, 1989) that takes into account transitions between pRII (left-hand square, ***Figure 4***D) and unphosphorylated RII subunits (right-hand square). The extended model also incorporates AKAR4 binding to and phosphorylation by free C subunits. We used a Bayesian approach (Eriksson et al., 2019) to estimate parameter sets for the model that could fit data pooled from AKAR4 recordings obtained after stimulation with 0, 0.2, 1 and 2 µM cAMP (***Figure 3***C & E). A log uniform prior parameter distribution was used as a starting point for the Bayesian method, where each parameter was allowed to vary three orders of magnitude around a default value (***Supplementary File 1***). The default values were taken from empirical data, including rates of pRII dephosphorylation determined in this study (***Figure 1***), and binding rates of C subunits to pRII and RII (Zhang et al., 2015). This

parameter estimation approach resulted in approximately 15,000 parameter sets that could explain the experimental data (***Figure 4***E-G). Simulations using these parameter sets enabled us to predict concentration changes of individual states within the model that cannot be determined experimentally (first three columns, ***Figure 4-figure supplement 1***). The model indicates that AKAP79 and CN together shift C subunit capture to the faster right-hand square sub-system (***Figure 4***D), driving down the fraction of free C subunits and thereby reducing PKA activity.

Mutation of the RIIα IS phosphorylation site occludes PKA suppression by CN

The results of the preceding sections show that AKAP79 targeting of CN for direct suppression of PKA is a viable mechanism for LTD induction. Previously published studies in hippocampal slices involving genetic manipulation of AKAP150 (the rodent ortholog of AKAP79) are also consistent with this mechanism. Full AKAP150 knock-out (Lu et al., 2008; Tunquist et al., 2008; Weisenhaus et al., 2010), or AKAP150 knock-in with variants lacking either the PKA or CN anchoring sites (Jurado et al., 2010; Sanderson et al., 2016), show that both AKAP150 anchoring sites are required for LTD induction. However, such approaches cannot distinguish between CN targeting to pRII subunits versus other substrates. If direct suppression of PKA activity by CN is essential for LTD induction, we reasoned that mutation of the IS phospho-acceptor S98 (***Figure 5***A) in the predominant RIIα isoform would be expected to disrupt LTD induction in CA1 neurons. To confirm this presupposition before undertaking experiments in neurons, we re-ran AKAR4 experiments at 1 µM cAMP substituting in either S98A or S98E RIIα. For each RIIα variant (***Figure 1-figure supplement 1***H), we compared responses with or without CN, with WT RIIβ and $AKAP79_{c97}$ present in all cases. For WT RIIα, addition of CN to the mixture decreased the peak rate of AKAR4 phosphorylation from 21.02±0.76 (light blue, ***Figure 5***B) to 8.24±0.79 % per minute (dark blue). Substituting in RIIα S98A generated slow rates of AKAR4 phosphorylation in both cases (6.30±0.44 % per min with CN, and 6.67±0.56 % without, ***Figure 5***C). Conversely, the peak rate of AKAR4 phosphorylation was high regardless of the presence of CN for the S98E RIIα variant (31.30±3.60 % per min without CN; 25.65±3.44 % with CN, ***Figure 5***D). Together, this data indicates that substituting in either mutant of RIIα in neurons would be expected to reduce LTD induction in neurons if direct suppression of PKA by CN is required in LTD induction (***Figure 5***E).

Before moving on to experiments in neurons, we used the data collected with RIIα variants to test the accuracy of our kinetic modeling. We ran simulations assuming that the S98A and S98E variants of RIIα would behave like dephosphorylated and phosphorylated forms of the regulatory subunit. Broadly, the simulations were in line with our experimental data and predicted that addition of CN would reduce PKA activity substantially more in the WT but not RIIα mutant conditions (***Figure 4-figure supplement 1***),

with low and high PKA activities regardless of CN concentration for the S98A and S98E variants, respectively. The model predictions for the extent by which AKAR4 phosphorylation was depressed in the RIIα S98A system were, however, spread out depending on the specific parameter set (column 4-5, ***Figure 4-figure supplement 1***). This implies that the WT data we used to constrain the model were not sufficient to precisely constrain the dynamics specifically for the unphosphorylated RII sub-system (right square, ***Figure 4***D) To understand the characteristics of those parameter sets that also reproduced the RIIα S98A behavior, we filtered the parameter sets returned by the parameter estimation approach into two classes depending on whether they fit closely (blue, ***Figure 4-figure supplement 1***) or not (red) to the acquired mutation data, yielding 526 parameter sets that fit closely to both the WT and mutation data. A pairwise coordinate plot (see ***Figure 5-figure supplement 1***A) shows that, except for a few parameters, the two classes do not appear to be visually distinct with regards to kinetic rates. However, analysis and subdivision of the eight model dissociation constants (K_D's) reveals interesting relationships (***Figure 5-figure supplement 1***B). Notably, as shown by the scatterplots for the K_D for interaction between RII-C and cAMP (K_D56), and RII-cAMP and C (K_D76) (***Figure 5-figure supplement 1***C), K_D56 should be relatively low within its range paired with a relatively high K_D76 (***Figure 5-figure supplement 1***D) to accurately mimic the biological workings of the PKA sub-system. This behavior may ensure that sufficient C subunit is released with increasing cAMP in our model when the kinetics are restrained to the unphosphorylated RII sub-system, i.e when the RIIα S98A mutation is introduced. Overall, simulations using unfiltered (top row, ***Figure 4-figure supplement 1***) and filtered (***Figure 5***F-H) parameter sets show that the kinetic model closely reproduces the experimental data, especially when further constrained using data collected with RIIα S98A. Furthermore, the constrained simulations reproduce the experimental data collected at different cAMP concentrations (***Figure 4-figure supplement 2***). Taken together, experiments and simulations with S98A and S98E variants of RIIα show that either of these mutations should prevent AKAP79 and CN from switching C subunit capture from the left-hand square sub-system to the faster right-hand square (***Figure 4***D). Therefore, either substitution would be expected to reduce LTD induction if the mechanism is important *in vivo*.

Disruption of RIIα phosphorylation in CA1 neurons impedes chemical LTD

To enable neuronal RIIα replacement experiments, we generated lentiviruses for shRNA-mediated knockdown of endogenous RIIα and simultaneous expression of shRNA-resistant RIIα variants in tandem with GFP. The lentiviruses contain an H1 promoter for expression of a highly-effective shRNA targeted to RIIα (***Figure 6***A). A UbC promoter drives expression of replacement RIIα sequences in tandem with GFP, with an internal ribosome entry sequence (IRES2) between the coding sequences of the two proteins enabling expression of GFP. We validated the lentiviruses in dissociated rat primary hippocampal neurons

by comparing the efficacy of five different lentiviruses. On day 7 *in vitro* (DIV7), we infected with control lentiviruses expressing either scrambled or shRIIα RNA, or with complete viruses for replacement of endogenous RIIα with either WT, S97A, or S97E (RIIα in rat is equivalent to S98 in human RIIα). Neuronal protein extracts were collected on DIV14, and analyzed using immunoblotting. Anti-RIIα immunoblotting (top row, ***Figure 6***B) confirmed effective suppression of endogenous RIIα with shRIIα (lane 3) but not scrambled RNA (lane 2), and strong expression of the replacement sequences (lanes 4-6). Expression of PKA C (row 2, ***Figure 6***B) and RIIβ subunits (row 3) was not affected by lentiviral infection in any case. Blocking PKA activity with H89 is known to prevent growth of new spines, whereas stimulating PKA with forskolin increases spine formation (Kwon & Sabatini, 2011). Replacing RIIα with the S97A variant – which has lower PKA activity regardless of CN activity (***Figure 5***F) – would therefore be expected to lead to a reduction in spines. To test this, we imaged dendritic spines on primary hippocampal neurons expressing either WT (left panel, ***Figure 6***C), S97A (middle panel), or S97E (right panel) RIIα. Consistent with a role for PKA in spinogenesis, spine density was reduced by 33.5 % (p=0.002) in neurons expressing the S97A variant to 1.17±0.11 spines per 10 μm compared to 1.76±0.12 for WT RIIα. Spine density for the S97E variant was similar to WT at 1.86±0.11 spines/10 μm.

To test whether the two substitutions at RIIα S97 affect LTD, we monitored changes in dendritic spine number during chemical LTD – a model of long-term synaptic depression that can be applied in dissociated neuronal cultures. Bath application of 20 μM NMDA for 3 minutes triggered a steady reduction in spine density (***Figure 6***E, top row) in neurons expressing WT RIIα as expected (Zhou et al., 2004), reaching a 20.4±1.6 %% reduction in spines after one hour (blue, ***Figure 6***F). In comparison, spine loss was attenuated in neurons expressing either the S97A (***Figure 6***E, middle row) or S97E (bottom row) RIIα variants. Spine numbers were reduced by only 9.07±0.96 % in neurons expressing RIIα S97A (red line, ***Figure 6***F), and by 9.90±1.8 % for the S97E variant (green line). The residual LTD in both conditions may correspond to action of CN on substrates other than pRII subunits, and limited suppression of PKA activity through CN dephosphorylation of the relatively small number of WT RIIβ subunits that are present in all cases. Overall, attenuation of spine loss in neurons expressing either S97A (p=0.00046) or S97E (p=0.0014) RIIα compared to WT subunits is consistent with an important role for direct PKA activity suppression by CN during the induction of LTD.

Discussion

The observations in this study support a revised mechanism for CN-mediated long-term depression in CA1 model synapses. AKAP79/150 is critical for anchoring PKA in dendritic spines (Tunquist et al., 2008; Weisenhaus et al., 2010) through association with RII subunits, which are the predominant neuronal PKA subunit in ~11-fold molar excess of C subunits in the CA1 neuropil (***Figure 2***D). Imaging studies (Ilouz et al., 2017; Weisenhaus et al., 2010) are consistent with our quantitative immunoblotting data, which show that RIIα is the major RII isoform in the CA1 neuropil. pRII dephosphorylation is limited prior to Ca^{2+} stimulation (***Figure 7***A), enabling a tonic level of dissociated C subunits sufficient to basally phosphorylate postsynaptic substrates in dendritic spines such as GluA1 subunits of AMPA-type glutamate receptors (Bear, 2003). LTD is brought about by CN (Mulkey et al., 1994), which is activated by Ca^{2+} entering spines through NMDA-type glutamate receptors (***Figure 7***B). AKAP79/150 contains a 'PIAIIIT' CN anchoring motif that is necessary for LTD (Jurado et al., 2010; Sanderson et al., 2012). In addition to potentially targeting CN to postsynaptic substrates including GluA1 subunits, the PIAIIIT anchoring motif positions CN adjacent to pRII subunits where it can efficiently dephosphorylate them (***Figure 7***B). This enables CN to increase the concentration of dephosphorylated RII species (blue spheres in the kinetic scheme shown in ***Figure 7***B) thereby directly suppressing PKA activity by increasing the rate of PKA C subunit capture. Consistent with this mechanism, blocking regulation of RII phosphorylation state by introducing mutations that mimic either the phosphorylated or dephosphorylated forms of the IS reduces LTD in cultured hippocampal neurons.

Our discovery that CN can directly suppress PKA activity in the AKAP79 complex reconciles three aspects of AKAP79 structure and function that had been enigmatic and paradoxical. First, previous studies showed that AKAP79 acts as a weak inhibitor of CN towards peptide substrates including a 20-mer peptide encompassing the phosphorylated RII IS (Coghlan et al., 1995; Kashishian et al., 1998), apparently at odds with the functional requirement for the anchoring protein in targeting CN to bring about LTD. We show that the key substrate for CN is likely to be full-length pRII subunits, and that in fact AKAP79 enhances the activity towards pRII at physiological concentrations by more than ten-fold. A second enigmatic feature of AKAP79 is its CN anchoring motif, PIAIIIT, which includes an additional central residue compared to the typical PxIxIT motif (Roy & Cyert, 2009). In a crystal structure of CN in complex with a peptide corresponding to AKAP79 positions 336-346, the additional leucine supports simultaneous binding of two copies of CN on either side of the motif (Li et al., 2012). Native mass spectrometry measurements of a purified AKAP79-CN-CaM-RIIα D/D complex also support a stoichiometry of 2 CN to 1 AKAP79 (Gold et al., 2011), although solution measurements indicate that when full-length RII subunits are bound to AKAP79, only one copy of CN can bind at a time (Li et al., 2012; Nygren et al., 2017). One possible explanation for this behavior is that CN binds transiently to

either side of the AKAP79 PIAIIIT motif enabling it to access both protomers of RII anchored to AKAP79 for efficient pRII dephosphorylation (cartoon representations in ***Figure 7***). This idea is consistent with data showing that mutating the PIAIIIT motif to a high-affinity canonical PxIxIT motif impairs the function of the phosphatase (Li et al., 2012), although it should be noted that it is not possible to determine whether two-sided CN binding to AKAP79 is necessary using the data presented here. Third, existing models of AKAP79 function assume that CN anchored to AKAP79 overcomes PKA phosphorylation at substrates with no reduction in PKA phosphorylation rate. In our revised mechanism, CN directly suppresses PKA activity when removing phosphate from substrates primed by PKA thereby avoiding energetically-costly ongoing futile cycling of phosphorylation and dephosphorylation by PKA and CN at these sites.

A challenge in the future will be to understand how the mechanism uncovered here relates to the full complexity of AKAP79 function. AKAP79 is directly regulated by Ca^{2+}/CaM, which binds to a 1-4-7-8 hydrophobic motif (Patel et al., 2017) starting at position W79. Binding of Ca^{2+}/CaM releases AKAP79 from the postsynaptic membrane (Dell'Acqua et al., 1998) and alters the conformation of the signaling complex by triggering formation of a second interface between CN and AKAP79 that involves an LxVP-type motif in AKAP79 (Gold et al., 2011; Nygren et al., 2017). Furthermore, metal ions including Ca^{2+} alter rates of substrate binding and product release from PKA C subunits (Knape et al., 2015; Zhang et al., 2015). Therefore, it will be important to understand the sensitivity of CN suppression of PKA activity to Ca^{2+} signals. Membrane targeting sequences regulate several components of the AKAP79 signaling complex. Myristylation of C subunits is important for limiting their diffusion rate in dendritic spines and concentrating PKA activity at the cell membrane (Tillo et al., 2017; Xiong et al., 2021). Localization of AKAP79 is also regulated by palmitoylation at C36 and C139 (Delint-Ramirez et al., 2011; Keith et al., 2012). Palmitoylation is required for endosomal localization of AKAP79, and AKAP79 depalmitoylation and synaptic removal is additionally regulated by CaMKII (Woolfrey et al., 2018). Our work suggests that removal of AKAP79 from synapses might be synchronized with accumulation of inhibited C subunits in the AKAP79 complex. Given that RII subunits greatly outnumber C subunits, movement of C subunits between different RII sub-populations, including RII subunits anchored to MAP2 in dendritic shafts (Tunquist et al., 2008), should also be considered along with PDEs that can terminate cAMP signals with high spatiotemporal precision (Bock et al., 2020; Tulsian et al., 2017). Non-dissociative activation of anchored type RII PKA has been put forward as an alternative mechanism to explain localised PKA activity (Smith et al., 2017). Current evidence indicates that C subunits do dissociate in neurons upon elevation of cAMP (Gold, 2019; Mo et al., 2017; Tillo et al., 2017), but it is important to note that suppression of PKA by pRII dephosphorylation is compatible with non-dissociative models of PKA

activation and this might occur in certain physiological settings. AKAP79 is a highly multivalent protein – other notable documented interaction partners include protein kinase C (Hoshi et al., 2010) and the Ca^{2+}-activated cyclase AC8 (Baldwin & Dessauer, 2018; Zhang et al., 2019). Oscillations of Ca^{2+}, cAMP, and PKA activity have been observed in pancreatic β-cells (Hinke et al., 2012; Ni et al., 2011), and knockout of AKAP150 leads to the loss of cAMP oscillations in β-cells upon stimulation with insulin (Hinke et al., 2012). CN dephosphorylation of pRII subunits bound to AKAP79 is likely to play a role in oscillatory patterns of PKA activity, and it will be important to understand how this mechanism underlies responses to short-lived and oscillatory changes in Ca^{2+} and cAMP concentration.

In this combined experimental-computational study, we focused on AKAP79 signaling in dendritic spines on the basis that this could serve as a prototype for understanding a potentially widespread non-canonical mechanism for altering PKA. In addition to its role in dendritic spines, AKAP79 regulates many different membrane channels and receptors following Ca^{2+} influx through a variety of sources, and the mechanism that we have uncovered here is likely to at least extend to these additional contexts. For example, AKAP79 underlies $GABA_A$ receptor regulation during LTD of GABAergic synapses (Dacher et al., 2013), and it positions PKA and CN for regulation of TRPV channels (Zhang et al., 2008), Kv7 channels (Zhang & Shapiro, 2012), and both β-adrenergic receptor isoform (Houslay & Baillie, 2005). AKAP79 is also necessary for NFAT dephosphorylation following Ca^{2+} entry through both L-type calcium channels (Wild et al., 2019) and the store-operated Ca^{2+} channel ORAI1 (Kar et al., 2014). The RII IS phosphorylation site is conserved throughout the animal kingdom, and co-anchoring of phosphatases alongside PKA is a feature of several AKAP complexes (Redden & Dodge-Kafka, 2011). Future investigations may therefore explore whether additional anchoring proteins are able to direct CN – or other cellular phosphatases – for direct suppression of PKA activity.

Methods & Materials

Key Resources Table

Key Resources Table				
Reagent type (species) or resource	**Designation**	**Source or reference**	**Identifiers**	**Additional information**
strain, strain background (*Escherichia coli*)	TOP10 chemically competent	Life Technologies	Cat# C404003	
strain, strain background (*Escherichia coli*)	BL21 (DE3)	Thermo Fisher Scientific	Cat# EC0114	
strain, strain background (*Escherichia coli*)	BL21 Tuner (DE3) pLysS	Merck	Cat# 70624	
strain, strain background (*Escherichia coli*)	BL21 Star (DE3)	Thermo Fisher Scientific	Cat# C601003	
strain, strain background (*Escherichia coli*)	*Stbl3*	Thermo Fisher Scientific	Cat# C737303	

cell line (*Homo-sapiens*)	HEK293	Horizon Discovery LTD	Cat# HCL3417	Myocplasma tested.
cell line (*Homo-sapiens*)	HEK293T	ATCC	Cat# CRL-3216	Myocplasma tested.
biological sample (*Rattus norvegicus*)	Sprague Dawley	UCL breeding colony	Not applicable	
antibody	Mouse monoclonal anti-PKA RIIα	BD Biosciences	Cat# 612243; RRID:AB_399566	0.8 µg/mL
antibody	Mouse monoclonal anti-PKA RIIβ	BD Biosciences	Cat# 610626; RRID:AB_397958	0.8 µg/mL
antibody	Mouse monoclonal anti-PKA C (pan)	BD Biosciences	Cat# 610981; RRID:AB_398294	0.5 µg/mL
antibody	Mouse monoclonal anti-PKA RI (pan)	BD Biosciences	Cat# 610166; RRID:AB_397567	0.8 µg/mL
antibody	Rabbit monoclonal anti-PKA phospho-RIIα	Abcam	Cat# ab32390; RRID:AB_779040	0.8 µg/mL
antibody	Rabbit polyclonal anti-GFP	Sigma Aldrich	Cat# SAB4301138; RRID:AB_2750576	0.5 µg/mL
antibody	Mouse monoclonal anti-β-tubulin	Biolegend	Cat# 903401; RRID: AB_2565030	0.5 µg/mL

antibody	Goat anti-rabbit HRP-linked secondary antibody	Cell Signalling Technology	Cat # 7074S; RRID:AB_2099233	1 μg/mL
antibody	Goat anti-mouse IgG (H+L) poly-HRP secondary antibody	Thermo Fisher Scientific	Cat# 32230; RRID:AB_1965958	1 μg/mL
recombinant DNA reagent	pIRES2-EGFP	Clontech	Cat# 6029-1	
recombinant DNA reagent	pFUGW-H1	Sally Temple lab/Addgene	Cat# 25870; RRID:Addgene_25870	Lentiviral entry vector.
recombinant DNA reagent	pFUGW-shRIIα-RIIα*-WT-IRES-EGFP	This study	Not applicable	Lentivral entry vector. Dr. Matthew G. Gold (University College London)
recombinant DNA reagent	pFUGW-shRIIα-RIIα*-S97A-IRES-EGFP	This study	Not applicable	Lentivral entry vector. Dr. Matthew G. Gold (University College London)
recombinant DNA reagent	pFUGW-shRIIα-RIIα*-S97E-IRES-EGFP	This study	Not applicable	Lentivral entry vector. Dr. Matthew G. Gold (University College London)
recombinant DNA reagent	pCMVdR8.74 & pMD2.G plasmids	Didier Trono lab/Addgene	Cat# 12259; RRID:Addgene_12259	Lentiviral packaging vectors
recombinant DNA reagent	pcDNA3.1-AKAR4-NES	Jin Zhang lab/Addgene	Cat# 64727; RRID:Addgene_64727	
chemical compound, drug	Lipofectamine 2000	Thermo Fisher Scientific	Cat# 11668019	

chemical compound, drug	DMEM, high glucose, pyruvate	Thermo Fisher Scientific	Cat # 41966029	
chemical compound, drug	Trypsin	Thermo Fisher Scientific	Cat# 25300054	
chemical compound, drug	Penicillin/ Streptomycin	Thermo Fisher Scientific	Cat# 15140122	
chemical compound, drug	GlutaMAX	Thermo Fisher Scientific	Cat# 35050061	
chemical compound, drug	DPBS, no calcium, no magnesium	Thermo Fisher Scientific	Cat# 14190144	
chemical compound, drug	HBSS	Thermo Fisher Scientific	Cat# 14185045	
chemical compound, drug	Heat-inactivated horse serum	Gibco	Cat# 26050088	
chemical compound, drug	Neurobasal-A medium	Thermo Fisher Scientific	Cat# 10888022	
chemical compound, drug	B27 supplement	Gibco	Cat# 17504044	
chemical compound, drug	Poly-L-Lysine	Sigma Aldrich	Cat# P2636	

chemical compound, drug	Boric acid	Sigma Aldrich	Cat# B6768-500g	
chemical compound, drug	Sodium tetraborate	Sigma Aldrich	Cat# 221732	
chemical compound, drug	cOmplete, Mini, EDTA-free Protease Inhibitor Cocktail	Roche	Cat# 11836170001	
chemical compound, drug	PhosSTOP phosphatase inhibitor tablets	Roche	Cat# 4906845001	
chemical compound, drug	Para-nitrophenylphosphate	Sigma Aldrich	Cat# N3254	
software, algorithm	Origin	OriginLab	www.originlab.com; RRID:SCR_014212	
software, algorithm	Reader Control Software for FLUOStar Omega	BMG Labtech	https://www.bmglabtech.com/reader-control-software/	
software, algorithm	MARS Data Analysis Software	BMG Labtech	https://www.bmglabtech.com/mars-data-analysis-software/	
software, algorithm	Unicorn Start 1.1 Software for controlling AKTA start system	GE Healthcare	Cat# 29225049	
software, algorithm	ImageJ (version 1.52)	NIH	RRID:SCR_003070	

software, algorithm	NeuronStudio	(Rodriguez et al., 2008)	https://icahn.mssm.edu; RRID:SCR_013798	

Protein expression and purification. Human PKA subunits were expressed and purified as described previously (Walker-Gray et al., 2017). GST-RIIα and GST-RIIβ were expressed in *Escherichia coli* BL21 Tuner (DE3) pLysS, and GST-Cβ in *E. coli* BL21 (DE3) grown in LB. In all cases, protein expression was induced by addition of 0.5 mM isopropyl β-D-1-thiogalactopyranoside (IPTG), and bacteria were harvested following overnight incubation at 20 °C. Cell pellets were thawed and sonicated in glutathione sepharose binding buffer (20 mM HEPES pH 7.5, 500 mM NaCl, 1 mM DTT, 0.5 mM EDTA, 1 mM benzamidine, 10 % glycerol) supplemented with 0.1 mg/mL lysozyme, and 0.1 % Igepal CA-630 (RII subunit preps only). Clarified lysates were incubated with glutathione sepharose 4B, and PKA subunits were eluted by overnight cleavage with PreScission protease thus removing N-terminal GST affinity tags. Finally, each subunit was purified using a HiLoad 16/600 Superdex 200 column connected in series with a GSTrap to remove residual GST using gel filtration buffer (20 mM HEPES pH 7.5, 150 mM NaCl, 5 % glycerol). S98A and S98E point mutations were introduced into RIIα subunits by site-directed mutagenesis (SDM) with primer pairs hS98A_F & R, and hS98E_F & R. RIIα variants were expressed and purified in the same way as the WT sequences.

Full-length human AKAP79 was cloned into pET28 using primers Nde1_AKAP79_1 and AKAP79_427_EcoRI for expression of N-terminally 6His-tagged protein. AKAP79 was expressed in 4 L BL21 Star (DE3) cells by overnight incubation at 37 °C in auto-induction media (AIM). PBS-washed bacterial pellets were resuspended in Talon binding buffer (30 mM Tris pH 8.0, 500 mM NaCl, 10 mM imidazole, 1 mM benzamidine) supplemented with 0.1 mg/mL lysozyme and one Complete EDTA-free protease inhibitor tablet (Roche) per 100 mL. Lysates were sonicated, clarified by centrifugation, and incubated with Talon Superflow resin for 2 hours prior to 3 x 10 mL washing in Talon binding buffer, and eluted with 2 x 2.5 mL Talon elution buffer (30 mM Tris, pH 7.0, 500 mM NaCl, 300 mM imidazole, 1 mM benzamidine). Eluted protein was exchanged into Q buffer A (20 mM Tris pH 8, 20 mM NaCl, 1 mM EDTA, 2 mM DTT) using a HiPrep 26/10 desalting column to enable purification using a 1 mL Resource Q column. Each variant was eluted using a NaCl/pH gradient with Q buffer A and a steadily increasing proportion of Q buffer B (20 mM Tris pH 7, 500 mM NaCl, 1 mM EDTA, 2mM DTT). In the final step, peak fractions were pooled and buffer exchanged into gel filtration buffer. Residues 331-427 of AKAP79 were cloned into pET28 using primers Nde1_AKAP79_331 and AKAP79_427_EcoRI for expression of the fragment AKAP79$_{c97}$ bearing an N-terminal His tag. This construct was transformed

into BL21 (DE3) cells, which were grown overnight at 37 °C in AIM. Lysis and metal affinity steps were as for full-length AKAP79 with the exception that Ni-NTA agarose (Life Technologies) was used in place of Talon resin. Following elution from Ni-NTA resin, the protein was purified by size exclusion using a HiLoad 16/600Superdex 200 pre-equilibrated in gel filtration buffer. To assemble complexes of full-length RII subunits and $AKAP79_{c97}$, mixtures of the purified proteins were incubated on ice in gel filtration buffer for 1 h with the AKAP fragment in a 2:1 molar excess. The complex was then separated from excess $AKAP79_{c97}$ by Superdex 200 size exclusion. pET28-$AKAP79_{c97}$ ΔCN was generated by performing PCR with an earlier construct lacking residues 337-343 as the template (Gold et al., 2011), whereas the ΔPKA variant (lacking residues 391-400) was generated by SDM with primers ΔPKA_F & _R. The two $AKAP79_{c97}$ deletion mutants were expressed and purified in the same way as the WT protein.

Human CN was expressed from a bicistronic pGEX6P1 vector (Gold et al., 2011) in *E. coli* BL21 Tuner (DE3) pLysS cells. Protein expression was induced by overnight incubation at 37 °C in 4L AIM. CN was purified following the same protocol as full-length PKA RII subunits, with the final size exclusion step performed using gel filtration buffer supplemented with 1 mM DTT. Human CaM was expressed and purified as described previously (Patel et al., 2017). Briefly, untagged CaM was expressed in *E. coli* BL21 (DE3) cells incubated overnight at 37 °C in AIM. CaM was initially purified using phenyl sepharose resin, then by ion exchange with a HiTrap Q HP column. Finally, CaM was exchanged into water and lyophilized prior to storage at -80 ºC. Human PP1α (7-300) was expressed in BL21 (DE3) *E. coli* in LB media supplemented with 1 mM $MnCl_2$ and purified as described previously (Kelker et al., 2009). The PP1 expression vector was a gift from Wolfgang Peti (Addgene plasmid # 26566). This vector was co-transformed with pGRO7 plasmid encoding the GroEL/GroES chaperone (Takara). PP1 expression was induced with 0.1 mM IPTG after prior induction of chaperone expression using 2 g/L arabinose. Bacteria were incubated for 20 hours at 10 °C following IPTG induction before harvesting. PP1 was purified by affinity to Ni-NTA agarose (Qiagen) followed by size exclusion with a Superdex 200 column equilibrated in PP1 gel filtration buffer (25 mM HEPES pH 7.5, 500 mM NaCl, 1 mM $MnCl_2$, 10% glycerol). For AKAR4 purification, an 8His epitope tag was ligated into pcDNA3.1-AKAR4-NES vector (Depry et al., 2011) (Addgene cat no. 64727) at the C-terminus of the sensor immediately prior to the nuclear export site using primers EcoI_8HisNLS_XbaI and XbaI_8HisNLS_EcoRI. The vector was transfected into 20 x 10 cm dishes of HEK293T cells cultured in DMEM using lipofectamine-2000 (Thermo Fisher Scientific). Cells were collected after 3 days, washed in PBS, then lysed in Talon binding buffer supplemented with 0.5 % Igepal CA-630, and sonicated briefly. AKAR4 was purified by affinity to Ni-NTA agarose following the same procedure as for AKAP79, and eluted protein was exchanged into gel filtration buffer, and aliquoted before storage at -80 ºC. All purification columns and resins were

purchased from GE Healthcare. All protein samples were concentrated using Vivaspin centrifugal concentrators (Sartorius). Denaturing gel electrophoresis was performed using NuPAGE 4-12 % Bis-Tris gels (Thermo Fisher Scientific), and protein concentrations were determined using the bicinchoninic acid (BCA) assay. Oligonucleotide primer sequences are listed in Supplementary File 2.

Phosphatase assays. For radioactive release assays, CN substrates were prepared by phosphorylating PKA RII subunits at the autoinhibitory site with PKA C subunit and ATP(γ-^{32}P). To radiolabel RIIα, RIIβ, or the purified complexes of each isoform with AKAP79$_{c97}$, 50 μg of the relevant sample was incubated in 100 μL with phosphorylation buffer (20 mM HEPES pH 7.5, 150 mM NaCl, 100 μM cAMP, 5 mM $MgCl_2$, 0.03 μg/μL C subunit) supplemented with 42 pmol [^{32}P-γ]-ATP at 3000 Ci/mmol and 10 μM cold ATP. After 15 min incubation at 30 °C, reactions were supplemented with 10 μM additional cold ATP. Following 15 min further incubation, reactions were finally supplemented up to 1 mM cold ATP for 10 min further incubation. ^{32}P-labelled protein was immediately separated from free ^{32}P using Sephadex G-25 Medium equilibrated in phospho-substrate storage buffer (20 mM HEPES pH 7.5, 150 mM NaCl, 10 % glycerol, 0.1 mM EDTA). Additional cold phospho-labelled substrates were prepared using scaled-up reactions with 1 mM cold ATP for 30 min at 30 °C.

Phosphatase assays using ^{32}P-labelled substrate (final volume 50 μL per assay) were prepared by first mixing appropriate dilutions of pRII substrates and CN on ice in dilution buffer (25 mM Na HEPES pH 7.5, 150 mM NaCl) to a final volume of 35 μL. 10 μL of reaction buffer (25 mM Na HEPES pH 7.5, 150 mM NaCl, 25 mM $MgCl_2$, 5 mM DTT, 0.5 mg/mL BSA, 1 mM EDTA) was then added before initiation of CN activity by addition of 5 μL activator mix (25 mM Na HEPES pH 7.5, 150 mM NaCl, 10 mM $CaCl_2$, 50 μM CaM). Assays was terminated after 30-60 s at 30 °C by addition of 350 μL 30 % trichloroacetic acid (TCA). Samples were then incubated on ice for 1 h, and protein was pelleted by centrifugation at 31,360 × *g* for 15 min at 2 °C. The separated supernatant and pellet were analyzed using a Beckman LS 6000SC scintillation counter to determine the fraction of phosphate released from the pRII substrate. Reaction conditions were optimized so that less than 10 % pRII was dephosphorylated in each assay. Assays were generally performed with 10 nM CN and terminated after 30 s, with the exception of measurements for pRIIα and pRIIβ (black lines, ***Figure 1***E & F) where 60 s reactions containing 100 nM CN were used.

For pNPP hydrolysis assays, para-nitrophenol (pNP) production was monitored continuously by measuring absorbance at 405 nm in a FLUOstar Omega microplate reader. Each 50 μL assay contained 5 μL of 10 x pNPP reaction buffer (100 mM Tris, pH 8.0, 100 mM NaCl, 10 mM CaCl2, 1 mg/ml of BSA, 60 mM MgCl2, 10 mM DTT), and 35 μL solution containing proteins at the appropriate concentrations in pNPP dilution buffer (100 mM Tris pH 8.0, 100 mM NaCl). Assays were performed with 200 nM CN,

and 5 μM CaM where appropriate. Reactions were initiated by addition of 10 μL pNPP (Merck) to a final concentration of 5 mM, and pNP production was monitored at 22 °C for 1 hour at 1-minute intervals. For assays using phosphopeptide substrate, 19-mer pRII was synthesised by Biomatik at > 95 % purity. Each 50 μL assay contained 5 μL of 10 x phosphopeptide reaction buffer (25 mM Na HEPES pH 7.5, 150 mM NaCl, 25 mM MgCl2, 5 mM DTT, 0.5 mg/mL BSA, 1 mM EDTA), and 30 μL solution containing proteins at the appropriate concentrations in phosphopeptide dilution buffer (25 mM Na HEPES pH 7.5, 150 mM NaCl). Assays were performed with 100 nM CN, and 3 μM CaM where appropriate. Assays were initiated by addition of pRII phosphopeptide to a final concentration of 40 μM, and terminated by addition of 50 μL Biomol Green solution (Enzo Life Sciences) following 3 min incubation at 22 °C. Free phosphate concentration was determined by measuring absorbance at 624 nm in the FLUOstar Omega microplate reader.

Quantitative immunoblotting of CA1 neuropil extracts. Hippocampal slices were prepared from 18-day old male Sprague-Dawley rats. Rats were euthanized by cervical dislocation and 350 μm-thick hippocampal slices were collected using a Leica VT1200S microtome in ice-cold sucrose-based saline (189 mM sucrose, 10 mM glucose, 3 mM KCl, 5 mM $MgSO_4$, 26 mM $NaHCO_3$, 1.25 mM NaH_2PO_4, 0.1 mM $CaCl_2$, pH 7.4) saturated with 95% O_2/5% CO_2. Slices were next transferred to a storage chamber filled with artificial cerebrospinal fluid (aCSF; 124 mM NaCl, 3 mM KCl, 24 mM $NaHCO_3$, 1.25 mM NaH_2PO_4, 1 mM $MgSO_4$, 10 mM glucose, 2 mM $CaCl_2$, pH 7.4) saturated with 95% O_2/5% CO_2 first for one hour at ~ 31 ˚C and at room temperature thereafter. For micro-dissection, slices were transferred onto a pre-chilled Sylgard-coated 90-mm petri dish atop a dry ice/ethanol bath. The CA1 neuropil layer was micro-dissected using an angled micro-knife (Cajigas et al., 2012) by first cutting along the borders of the stratum pyramidale/stratum radiatum and the stratum lacunosum moleculare/hippocampal fissure. Subsequent lateral cuts at the CA2-CA1 and subiculum-CA1 borders completed the rectangular micro-slices. Micro-dissected neuropil slices were immediately snap frozen in liquid nitrogen and stored at -80 °C. To extract protein, neuropil slices (~ 15 per animal) were first pulverized with a micro-pestle then resuspended in a final volume of 300 μL extraction buffer (50 mM Tris-HCl, 50 mM NaF, 10 mM EGTA, 10 mM EDTA, 0.08 mM sodium molybdate, 5 mM sodium pyrophosphate, 1 mM penylmethylsulfonyl fluoride, 0.5 % mM Igepal CA-630, 0.25% mM sodium deoxycholate, 4 mM para-nitrophenylphosphate, cOmplete EDTA-free protease inhibitors and PhosStop phosphatase inhibitors (Roche) at 1 tablet each per 50 mL). The homogenate was sonicated briefly (30 s at 20 MHz) then clarified by centrifugation at 21,130 x *g* (15 min at 4 °C). Total protein concentration in each extract was determined by BCA assay. Quantitative immunoblotting was performed as described previously (Walker-Gray et al., 2017) using anti-PKA subunit primary antibodies purchased from BD Biosciences. HRP-conjugated secondary

antibodies were detected with WesternBright ECL chemiluminescent HRP substrate using a ImageQuant imaging unit (GE Healthcare). Band intensities for reference protein standards and neuropil extracts were calculated in ImageJ. For each immunoblot, a reference curve was generated by fitting reference protein concentrations and band intensities to a Hill function (with typical R^2 coefficients > 0.99) using iterative least squares refinement with the Levenberg-Marquardt algorithm in Origin (OriginLab). PKA subunit concentrations in neuropil extracts were determined by cross-referencing to reference curves derived from the same immunoblot.

AKAR4 measurements. AKAR4 fluorescence measurements were performed using black-walled 96-well plates in a FLUOstar Omega microplate reader (BMG Labtech) equipped with a 430nm excitation filter, and 485nm/520nm emission filters. Each 50 µL reaction contained 35 µL proteins mixed in dilution buffer (20 mM HEPES pH 7.5 and 100 mM NaCl) including AKAR4 reporter (0.2 µM final concentration in all cases) and 5 µL of 10 x reaction buffer (20 mM Na HEPES pH 7.5, 100 mM NaCl, 10 mM DTT, 100 mM $MgCl_2$, 10 mM $CaCl_2$, 0.5 % Igepal CA-630). After three baseline measurements, PKA phosphorylation was initiated by addition of 10 µL solution containing ATP and the desired concentration of cAMP using two injectors built into the plate reader. One injector was primed with ATP solution (20 mM Na HEPES pH 7.5, 100 mM NaCl, 25 mM ATP) and the other with ATP/cAMP solution (20 mM Na HEPES pH 7.5, 100 mM NaCl, 25 mM ATP, 2.5 or 10 µM cAMP) so that different proportions of the two injectors could be used to vary the final cAMP concentration. Measurements were collected at 5 second intervals for a minimum of 10 minutes at 22 ºC following injection of ATP. For every run, one control well was included in which AKAR4 was omitted from the protein mixture to enable baseline subtraction.

Phosphorylated AKAR4 (pAKAR4), for use in assays comparing PP1 and CN activity towards the reporter, was prepared by incubating 400 µg purified AKAR4 with 20 µg PKA C subunit in 1 mL AKAR4 phosphorylation buffer (25 mM Na Hepes pH 7.5, 150 mM NaCl, 10 mM $MgCl_2$, 5 mM ATP, 2 mM DTT). Following 30 min incubation at 30 °C, the phosphorylated reporter was exchanged into 25 mM Na Hepes pH 7.5 and 100 mM NaCl using Sephadex G-25 medium. In pAKAR4 dephosphorylation assays, each well contained 35 µL phosphatase at the appropriate concentration in dilution buffer mixed with 5 µL of 10 x reaction buffer. Reactions were initiated by injection of 10 µL AKAR4 solution to a final concentration of 0.2 µM, and measurements were collected at 5 s intervals for 15 minutes thereafter. For all AKAR4 assays, run parameters were set using Reader Control Software for FLUOstar Omega, and measurements were analyzed using MARS Data Analysis Software (BMG Labtech). Aliquots of a single AKAR4 purification were used across all experiments.

Kinetic modeling. The model scheme of PKA activation is an updated and extended version of the one published by Buxbaum and Dudai (Buxbaum & Dudai, 1989). The model was simulated in a single reaction compartment devoid of any geometry as a system of chemical reactions mimicking the experimental conditions listed above. The individual chemical reactions were modeled as ordinary differential equation (ODE) using the chemical mass-action equation, as:

$$A + B \underset{k_r}{\overset{k_f}{\Leftrightarrow}} AB$$

$$-\frac{d[A]}{dt} = -\frac{d[B]}{dt} = \frac{d[AB]}{dt} = k_f\,(x) = k_f[A][B] = k_r[AB]$$

In total, there were 16 chemical species and 16 reactions included in the model, incorporating mostly bi-molecular reactions with forward and backward reaction rates. Enzymatic reactions were represented by the three elementary steps of binding, dissociation and catalysis. All model variants were built using the MATLAB Simbiology toolbox (MathWorks). All reactions, along with initial concentrations of all chemical species and kinetic rates, are listed in ***Supplementary File 1***.

PKA activation follows a sequential binding of four cAMP molecules to the PKA regulatory RII subunit holoenzyme followed by the release (or activation) of two active catalytic subunits (Taylor et al., 2019). However, the chosen modeling approach involved some simplifications: (1) The two RII subunits within the holoenzyme were assumed to behave independently – whereas in reality, some cooperativity is observed in PKA activation due to intra-dimeric contacts within the PKA holoenzymes (Taylor et al., 2012); (2) The two cAMP binding sites on the RII subunit were modelled as a single binding event such that binding of cAMP to RII/pRII is first order with respect to cAMP (Hao et al., 2019). This simplification was incorporated as our focus here was on understanding transitions between pRII and RII subunits and not the precise mechanism of cAMP activation; (3) The respective dephosphorylation parameters for both pRII and pRII bound to cAMP were assumed to be equal; (4) Rates of RII phosphorylation by bound C subunit were assumed to be equal irrespective of whether cAMP was bound to the regulatory subunit; (5) RIIα and RIIβ were assumed to behave similarly since isoform-specific differences were not the focus here. These simplifications were used to reduce the number of model parameters.

Parameters corresponding to the reactions involving dephosphorylation by CN were modified to represent the situations ‘with’ and ‘without’ AKAP79 (***Supplementary File 1***). In total eighteen different experimental AKAR4 responses were used to estimate the model parameters. Twelve corresponded to

data shown in ***Figure 3***C & E collected with either 0, 0.2, 1 or 2 μM cAMP activation: conditions with PKA (II) + CaM either alone, with CN, or with both CN and AKAP79. The other six correspond to the calibration curves of C subunit interaction with AKAR4 (***Figure 3-figure supplement* 1**A), which were used to estimate AKAR4 parameters that were kept frozen when the other model parameters were estimated. All parameters were estimated using an approximate Bayesian computation (ABC) approach, which included copulas for merging of different experimental data sets (Eriksson et al., 2019). A Bayesian approach was used over optimization for a single parameter set, to account for the uncertainty in parameter space, and that more than one set of parameters could fit the data. The result is thus described using distributions for possible parameter values, rather than single values. Initial prior knowledge about the possible parameter values using data from this study, and previously published work from other groups (Buxbaum & Dudai, 1989; Isensee et al., 2018; Moore et al., 2003), was used to initiate the parameter fitting (details in ***Supplementary File 1***). To account for parameter uncertainty, a log uniform prior distribution for the ABC-method was used. Many of the parameters were set to have a 'prior' range which varied three orders of magnitude from a default parameter value (black bar in ***Figure 5-figure supplement 1***A), which ensured that our parameter values adopted in previous studies (Buxbaum & Dudai, 1989) were sampled. Simulations were started with initial conditions mimicking the experimental settings, thus for the WT system the initial conditions were assumed to reflect that all RII were either free or bound to C with no phosphorylated species or interactions with cAMP. Simulations were then run for the same length as time as the experiments, assuming the cAMP was added at t=0 and that autophosphorylation started at that time.

For predicting responses with mutant RIIα subunits, the base model was extended by splitting the RII into two pools, namely RIIα (85%) and RIIβ (15%) but keeping the parameter distribution received from the parameter estimation when only one isoform of RII was accounted for. Experiments with WT RII subunits were successfully re-simulated with the extended model to validate the approach. As the mutations when simulating both S98A and S98E were in the RIIα subtype (85%), the corresponding parameters depicting the mutation were only varied for this pool. Both the mutant forms, S98A and S98E, were tested as different model variants. To mimic the conditions of the S98A mutation in the model, the phosphorylation rates of RIIα and RIIα bound with cAMP were set to zero (i.e. for the RIIα partition of the model, kinetics were restricted to the right-hand square sub-system shown in ***Figure 4***D). Here the initial conditions were estimated in the same way as described above. To mimic the S98E mutation in the model, the turnover number for dephosphorylation of pRIIα and pRIIα with cAMP by CN were set to zero (i.e. for the RIIα partition of the model, kinetics were restricted to the left-hand square in ***Figure 4***D). Since S98E mimics a case where all the RII subunits are phosphorylated, in this case initial conditions were such that all RIIα were distributed between pRIIα and pRIIα-C.

All model variants were built using the MATLAB Simbiology toolbox (MathWorks). Simulations of these reaction systems were performed using the ode15s solver. All simulations were run for 605 s and the AKAR4 phosphorylation was extracted as output to compare with the experimental findings. The model equations were also exported to the statistical programming language R (https://www.r-project.org/) for implementing the parameter estimation through the ABC-copula approach (Eriksson et al., 2019) and only accept parameter sets whose simulated phosphorylated AKAR4 curves reproduced the experimental measurements. A slight modification to the distance measure ρ was introduced to include timeseries data, where $\rho = \sum_i (y_i^{exp} - y_i^{sim})^2 / n$ where y are experimental and simulated data points (normalized to be within 0 and 1) and n the number of data points for the experiment (for details see the code repository). The sampling resulted in approximately 15,000 parameter samples (a subset of which are shown in ***Figure 5-figure supplement 1***A) which all fitted the experimental data within a threshold set to $\rho < 0.01$. All parameter set samples, describing the uncertainty in the parameter estimates, were next projected onto the situations with mutant RIIα subunits. The model immediately reproduced the experimental observations with RIIα S98E subunits. Although the model correctly reproduced lower rates of AKAR4 that occur with RIIα S98A subunits, and that suppression of PKA activity by AKAP79/CN is reduced in this case, there was a substantial spread in the simulated responses in this case. This indicated that WT data had not perfectly constrained the dynamics in the unphosphorylated RII sub-system (right-hand square, ***Figure 4***B). Therefore, to better understand which parameter characteristics that were important to also account for the RIIα S98A, the parameter sets were sub-classified based on how well they fit data collected with RIIα S98A subunits and no CN (light red, ***Figure 5***C) using a threshold of 0.0. The parameter sets and its effect on different chemical species of the model were described by multi-trajectory, pairwise coordinate and boxplots, where the color schemes follow the classification described above. A code repository for this study may be accessed at https://github.com/jdgas/AKAP79_PKA. It contains the R code for the ABC method as well as MATLAB code for reproducing figures. The R code has to be run on a computer cluster. The repository also contains the models with a few example parameter sets, the full parameter sample as described above, and supplementary figures with simulations and experimental data for all 0, 0.2, 1 and 2 μM cAMP levels with either WT S98A, or S98E RIIα in the reaction mix.

Lentivirus construction. Lentiviruses were generated by inserting RIIα-IRES2-GFP expression cassettes into a pFUGW-H1 lentiviral vector (Addgene cat no. 25870) containing a shRNA sequence targeting for rat RIIα. In the first step, coding sequence for rat PKA RIIα was isolated from a cDNA library that we generated from total hippocampal RNA from a 7-day old male Sprague Dawley rat bred in the UCL

colony. RNA was extracted using an RNeasy Mini Kit before the cDNA library was generated using the first-strand cDNA synthesis kit. Coding sequence for RIIα was amplified from the library using primers Prkar2a_F & Prkar2a_R and inserted upstream of the IRES2 sequence in pIRES2-GFP (Clontech) using EcoRI and BamHI entry sites. Three pFUGW-H1-shRIIα vectors were constructed to determine an optimal targeting sequence for knockdown of rat RIIα. The targeting sequences (primer pairs shRIIα_F1/R1, shRIIα_F2/R2, and shRIIα_F3/R3) were inserted using the XbaI site of pFUGW-H1. The efficiency of each targeting sequence was determined by co-transfecting HEK293T cells with pIRES2-RIIα-EGFP and each pFUGW-H1 vector, with the pFUGW vector in a 10-fold excess. Anti-RIIα immunoblotting revealed that sequence shRIIα-1, which targets bases 134-154 in the rat RIIα coding sequence, was particularly effective at knocking down RIIα protein levels (***Figure 6***B) so this variant served as the parent pFUGW-H1-shRIIα vector in the subsequent steps. The coding sequence for RIIα in pIRES2-RIIα-GFP was rendered shRNA-resistant ('RIIα*') by SDM with primers Prkar2a_shRNA_resist_F & R. After introducing an NheI entry site into pFUGW-H1-shRIIα by SDM using primers FUGW_NheI_F & R, the dual expression cassette for RIIα-IRES2-GFP was transferred across into pFUGW-H1-shRIIα downstream of the ubiquitin promoter using NheI and AgeI sites to create the complete lentiviral vector pFUGW-H1-shRIIα-RIIα*-IRES2-EGFP.

Vectors containing RIIα replacement sequences with mutations at S97 were obtained by SDM with primers pairs rS97A_F & R and rS97E_F & R. In addition, a control vector containing a scrambled shRNA sequence was constructed using primers shScram_F & R. To produce lentivirus, pFUGW vectors were co-transfected with pCMVdR8.74 packaging vector (Addgene cat no. 12259) and pMD2.G envelope glycoprotein vector (Addgene cat no. 12259) into HEK293 cells using Lipofectamine 2000 and maintained in DMEM supplemented with 10% FBS. Cell culture media was collected at both 48 and 72 hours after transfection, subjected to 0.45 µm filtering, and centrifuged at 48,384 x *g* for 4 hours at 4°C to concentrate viral particles. Pelleted virus was resuspended in sterile PBS and stored at – 80 °C. Lentiviruses were validated by transducing dissociated hippocampal cultures on DIV7. Neurons were collected on DIV14, and protein extracted using sonication (3 x 10 s at 20 MHz) in extraction buffer. The homogenate was clarified by centrifugation at 21,130 x g for 15 minutes before analysis of protein levels in the supernatant by immunoblotting using antibodies including anti-PKA pRIIα (Abcam, RRID: AB_779040), anti-GFP (Sigma Aldrich, RRID: AB_2750576), and anti-β-tubulin antibodies (Biolegend, RRID: AB_2565030).

Lentiviral infection and imaging of dissociated primary hippocampal neurons. Primary hippocampal cultures were cultured from E18 Sprague-Dawley pups. Hippocampi were isolated and triturated with

trypsin (0.025%) before plating on poly-L-lysine-coated coverslips or 6-well plates in DMEM containing 10% heat-inactivated horse serum, and penicillin (40 U/mL)/streptomycin (40 µg/mL). Neurons were cultured at 37°C in 95% air/5% CO_2. Two hours after seeding, the plating media was replaced with Neurobasal-A supplemented with 1% B27, 0.5% (v/v) GlutaMAX, 20 mM glucose, and penicillin (100 U/mL)/streptomycin (100 µg/mL). Culture media and additives were purchased from Gibco with the exception of GlutaMAX (Thermo Fisher Scientific). Neurons were infected with lentivirus at DIV7 or DIV9 for dendritic spine density and time-lapse experiments, respectively. Concentrated viral stocks were diluted in conditioned media and incubated with neurons for 18 hours before replacing with fresh pre-conditioned media. Live-cell confocal imaging of dendritic spines was performed using an upright Zeiss LSM 510 confocal microscope equipped with an Achroplan 40x water differential interference contrast objective (numerical aperture 0.8). Transduced neurons were washed four times in HEPES-buffered Krebs solution (140 mM NaCl, 4.2 mM KCl, 1.2 mM $MgCl_2$, 2.52 mM $CaCl_2$, 5 mM Na HEPES, and 11 mM glucose, adjusted to pH 7.4 with NaOH) and placed into a chamber in this same solution at room temperature. For each dendritic segment, upper and lower bounds in the z-plane were initially determined using a rapid z-scan. A full image stack was then collected using a 488 nm Argon laser and a 505-530 nm band-pass emission filter for imaging EGFP fluorescence using 512 x 512 frames with 3-line averaging, and optical slice spacing of 1.035 µm. Time-lapse experiments were conducted to measure changes in spine density and spine-head size after the induction of chemical LTD. An optical slice spacing of 0.9 µm was used during time-lapse experiments. Z-stacks were acquired every 5 min from 15 min before to 60 min after the induction of chemical LTD. Bath application of 20 µM NMDA for 3 min was used to induce NMDAR-dependent LTD (Lee et al., 1998). Data was deconvolved using ImageJ (NIH) before automated dendrite identification and classification in NeuronStudio (Rodriguez et al., 2008). In time-lapse experiments, dendritic spine densities were normalized to the value at t=0.

Statistical analysis. All data are presented as means ± SE. Kinetic rates were statistically compared using two-tailed unpaired Student *t*-tests. Spine imaging data was compared by ANOVA with Turkey post-hoc tests (***Figure 6***D) and Bonferroni's post-hoc test (***Figure 6***G). $*p < 0.05$; $**p < 0.01$; $***p < 0.001$.

Acknowledgements

We thank Denis Yuan for assistance with protein purification, and Alexandra Jauhiainen, Andrei Kramer and Federica Milinanni for help with the parameter estimation process. MGG is a Wellcome Trust and Royal Society Sir Henry Dale fellow (104194/Z/14/A), and is grateful for support from the BBSRC (BB/N015274/1). SH is a Rett Syndrome Fellow and also supported by a Wellcome Trust Collaborative

762 award to TGS. The research was supported by the Swedish Research Council (VR-M-2017-02806; VR-
763 M-2020-01652), the Swedish e-Science Research Centre (SeRC), European Union/Horizon 2020 no.
764 945539 Human Brain Project SGA3, and an Erasmus Scholarship from Portugal. Optimizations and
765 simulations were performed on resources provided by the Swedish National Infrastructure for Computing
766 (SNIC) at Lunarc, Lund University.
767

References

Aye, T. T., Scholten, A., Taouatas, N., Varro, A., Van Veen, T. A., Vos, M. A., & Heck, A. J. (2010, Oct). Proteome-wide protein concentrations in the human heart. *Mol Biosyst, 6*(10), 1917-1927. https://doi.org/10.1039/c004495d

Baillie, G. S., Tejeda, G. S., & Kelly, M. P. (2019, Oct). Therapeutic targeting of 3',5'-cyclic nucleotide phosphodiesterases: inhibition and beyond. *Nat Rev Drug Discov, 18*(10), 770-796. https://doi.org/10.1038/s41573-019-0033-4

Baldwin, T. A., & Dessauer, C. W. (2018, Jan 16). Function of Adenylyl Cyclase in Heart: the AKAP Connection. *J Cardiovasc Dev Dis, 5*(1). https://doi.org/10.3390/jcdd5010002

Bear, M. F. (2003, Apr 29). Bidirectional synaptic plasticity: from theory to reality. *Philos Trans R Soc Lond B Biol Sci, 358*(1432), 649-655. https://doi.org/10.1098/rstb.2002.1255

Bers, D. M., Xiang, Y. K., & Zaccolo, M. (2019, Jul 1). Whole-Cell cAMP and PKA Activity are Epiphenomena, Nanodomain Signaling Matters. *Physiology (Bethesda), 34*(4), 240-249. https://doi.org/10.1152/physiol.00002.2019

Blumenthal, D. K., Takio, K., Hansen, R. S., & Krebs, E. G. (1986, Jun 25). Dephosphorylation of cAMP-dependent protein kinase regulatory subunit (type II) by calmodulin-dependent protein phosphatase. Determinants of substrate specificity. *J Biol Chem, 261*(18), 8140-8145. https://www.ncbi.nlm.nih.gov/pubmed/3013843

Bock, A., Annibale, P., Konrad, C., Hannawacker, A., Anton, S. E., Maiellaro, I., Zabel, U., Sivaramakrishnan, S., Falcke, M., & Lohse, M. J. (2020, Sep 17). Optical Mapping of cAMP Signaling at the Nanometer Scale. *Cell, 182*(6), 1519-1530 e1517. https://doi.org/10.1016/j.cell.2020.07.035

Buxbaum, J. D., & Dudai, Y. (1989, Jun 5). A quantitative model for the kinetics of cAMP-dependent protein kinase (type II) activity. Long-term activation of the kinase and its possible relevance to learning and memory. *J Biol Chem, 264*(16), 9344-9351. https://www.ncbi.nlm.nih.gov/pubmed/2722837

Cajigas, I. J., Tushev, G., Will, T. J., tom Dieck, S., Fuerst, N., & Schuman, E. M. (2012, May 10). The local transcriptome in the synaptic neuropil revealed by deep sequencing and high-resolution imaging. *Neuron, 74*(3), 453-466. https://doi.org/10.1016/j.neuron.2012.02.036

Clouet, D. H., & Gaitonde, M. K. (1956, Dec). The changes with age in the protein composition of the rat brain. *J Neurochem, 1*(2), 126-133. https://doi.org/10.1111/j.1471-4159.1956.tb12063.x

Coghlan, V. M., Perrino, B. A., Howard, M., Langeberg, L. K., Hicks, J. B., Gallatin, W. M., & Scott, J. D. (1995, Jan 6). Association of protein kinase A and protein phosphatase 2B with a common anchoring protein. *Science, 267*(5194), 108-111. http://www.ncbi.nlm.nih.gov/entrez/query.fcgi?cmd=Retrieve&db=PubMed&dopt=Citation&list_uids=7528941

Dacher, M., Gouty, S., Dash, S., Cox, B. M., & Nugent, F. S. (2013, Feb 6). A-kinase anchoring protein-calcineurin signaling in long-term depression of GABAergic synapses. *J Neurosci, 33*(6), 2650-2660. https://doi.org/10.1523/JNEUROSCI.2037-12.2013

Delint-Ramirez, I., Willoughby, D., Hammond, G. R., Ayling, L. J., & Cooper, D. M. (2011, Sep 23). Palmitoylation targets AKAP79 protein to lipid rafts and promotes its regulation of calcium-sensitive adenylyl cyclase type 8. *J Biol Chem, 286*(38), 32962-32975. https://doi.org/10.1074/jbc.M111.243899

Dell'Acqua, M. L., Dodge, K. L., Tavalin, S. J., & Scott, J. D. (2002, Dec 13). Mapping the protein phosphatase-2B anchoring site on AKAP79. Binding and inhibition of phosphatase activity are mediated by residues 315-360. *J Biol Chem, 277*(50), 48796-48802. https://doi.org/10.1074/jbc.M207833200

Dell'Acqua, M. L., Faux, M. C., Thorburn, J., Thorburn, A., & Scott, J. D. (1998, Apr 15). Membrane-targeting sequences on AKAP79 bind phosphatidylinositol-4, 5-bisphosphate. *Embo J, 17*(8), 2246-2260. http://www.ncbi.nlm.nih.gov/entrez/query.fcgi?cmd=Retrieve&db=PubMed&dopt=Citation&list_uids=9545238

Depry, C., Allen, M. D., & Zhang, J. (2011, Jan). Visualization of PKA activity in plasma membrane microdomains [Research Support, N.I.H., Extramural]. *Mol Biosyst, 7*(1), 52-58. https://doi.org/10.1039/c0mb00079e

Dittmer, P. J., Dell'Acqua, M. L., & Sather, W. A. (2014, Jun 12). Ca2+/calcineurin-dependent inactivation of neuronal L-type Ca2+ channels requires priming by AKAP-anchored protein kinase A. *Cell Rep, 7*(5), 1410-1416. https://doi.org/10.1016/j.celrep.2014.04.039

Eriksson, O., Jauhiainen, A., Maad Sasane, S., Kramer, A., Nair, A. G., Sartorius, C., & Hellgren Kotaleski, J. (2019, Jan 15). Uncertainty quantification, propagation and characterization by Bayesian analysis combined with global sensitivity analysis applied to dynamical intracellular pathway models. *Bioinformatics, 35*(2), 284-292. https://doi.org/10.1093/bioinformatics/bty607

Gildart, M., Kapiloff, M. S., & Dodge-Kafka, K. L. (2020, Jul). Calcineurin-AKAP interactions: therapeutic targeting of a pleiotropic enzyme with a little help from its friends. *J Physiol*, *598*(14), 3029-3042. https://doi.org/10.1113/JP276756

Gold, M. G. (2019, Oct 31). Swimming regulations for protein kinase A catalytic subunit. *Biochem Soc Trans*, *47*(5), 1355-1366. https://doi.org/10.1042/BST20190230

Gold, M. G., Lygren, B., Dokurno, P., Hoshi, N., McConnachie, G., Tasken, K., Carlson, C. R., Scott, J. D., & Barford, D. (2006, Nov 3). Molecular basis of AKAP specificity for PKA regulatory subunits. *Molecular cell*, *24*(3), 383-395. https://doi.org/10.1016/j.molcel.2006.09.006

Gold, M. G., Stengel, F., Nygren, P. J., Weisbrod, C. R., Bruce, J. E., Robinson, C. V., Barford, D., & Scott, J. D. (2011, Apr 19). Architecture and dynamics of an A-kinase anchoring protein 79 (AKAP79) signaling complex. *Proc Natl Acad Sci U S A*, *108*(16), 6426-6431. https://doi.org/10.1073/pnas.1014400108

Grigoriu, S., Bond, R., Cossio, P., Chen, J. A., Ly, N., Hummer, G., Page, R., Cyert, M. S., & Peti, W. (2013). The molecular mechanism of substrate engagement and immunosuppressant inhibition of calcineurin. *PLoS biology*, *11*(2), e1001492. https://doi.org/10.1371/journal.pbio.1001492

Hinke, S. A., Navedo, M. F., Ulman, A., Whiting, J. L., Nygren, P. J., Tian, G., Jimenez-Caliani, A. J., Langeberg, L. K., Cirulli, V., Tengholm, A., Dell'Acqua, M. L., Santana, L. F., & Scott, J. D. (2012, Oct 17). Anchored phosphatases modulate glucose homeostasis. *Embo J*, *31*(20), 3991-4004. https://doi.org/10.1038/emboj.2012.244

Hogan, P. G. (2017, May). Calcium-NFAT transcriptional signalling in T cell activation and T cell exhaustion. *Cell Calcium*, *63*, 66-69. https://doi.org/10.1016/j.ceca.2017.01.014

Hoshi, N., Langeberg, L. K., Gould, C. M., Newton, A. C., & Scott, J. D. (2010, Feb 26). Interaction with AKAP79 modifies the cellular pharmacology of PKC. *Molecular cell*, *37*(4), 541-550. https://doi.org/10.1016/j.molcel.2010.01.014

Houslay, M. D., & Baillie, G. S. (2005, Dec). Beta-arrestin-recruited phosphodiesterase-4 desensitizes the AKAP79/PKA-mediated switching of beta2-adrenoceptor signalling to activation of ERK. *Biochem Soc Trans*, *33*(Pt 6), 1333-1336. https://doi.org/10.1042/BST20051333

Huang, Y. Y., Li, X. C., & Kandel, E. R. (1994, Oct 7). cAMP contributes to mossy fiber LTP by initiating both a covalently mediated early phase and macromolecular synthesis-dependent late phase. *Cell*, *79*(1), 69-79. https://doi.org/10.1016/0092-8674(94)90401-4

Ilouz, R., Lev-Ram, V., Bushong, E. A., Stiles, T. L., Friedmann-Morvinski, D., Douglas, C., Goldberg, G., Ellisman, M. H., & Taylor, S. S. (2017, Jan 12). Isoform-specific subcellular localization and function of protein kinase A identified by mosaic imaging of mouse brain. *Elife*, *6*. https://doi.org/10.7554/eLife.17681

Isensee, J., Kaufholz, M., Knape, M. J., Hasenauer, J., Hammerich, H., Gonczarowska-Jorge, H., Zahedi, R. P., Schwede, F., Herberg, F. W., & Hucho, T. (2018, Jun 4). PKA-RII subunit phosphorylation precedes activation by cAMP and regulates activity termination. *J Cell Biol*, *217*(6), 2167-2184. https://doi.org/10.1083/jcb.201708053

Jurado, S., Biou, V., & Malenka, R. C. (2010, Sep). A calcineurin/AKAP complex is required for NMDA receptor-dependent long-term depression. *Nat Neurosci*, *13*(9), 1053-1055. https://doi.org/nn.2613 [pii]
10.1038/nn.2613

Kar, P., Samanta, K., Kramer, H., Morris, O., Bakowski, D., & Parekh, A. B. (2014, Jun 16). Dynamic assembly of a membrane signaling complex enables selective activation of NFAT by Orai1. *Curr Biol*, *24*(12), 1361-1368. https://doi.org/10.1016/j.cub.2014.04.046

Kashishian, A., Howard, M., Loh, C., Gallatin, W. M., Hoekstra, M. F., & Lai, Y. (1998, Oct 16). AKAP79 inhibits calcineurin through a site distinct from the immunophilin-binding region. *J Biol Chem*, *273*(42), 27412-27419. https://doi.org/10.1074/jbc.273.42.27412

Keith, D. J., Sanderson, J. L., Gibson, E. S., Woolfrey, K. M., Robertson, H. R., Olszewski, K., Kang, R., El-Husseini, A., & Dell'acqua, M. L. (2012, May 23). Palmitoylation of A-kinase anchoring protein 79/150 regulates dendritic endosomal targeting and synaptic plasticity mechanisms. *J Neurosci*, *32*(21), 7119-7136. https://doi.org/10.1523/JNEUROSCI.0784-12.2012

Kelker, M. S., Page, R., & Peti, W. (2009, Jan 9). Crystal structures of protein phosphatase-1 bound to nodularin-R and tautomycin: a novel scaffold for structure-based drug design of serine/threonine phosphatase inhibitors. *J Mol Biol*, *385*(1), 11-21. https://doi.org/10.1016/j.jmb.2008.10.053

Kinderman, F. S., Kim, C., von Daake, S., Ma, Y., Pham, B. Q., Spraggon, G., Xuong, N. H., Jennings, P. A., & Taylor, S. S. (2006, Nov 3). A dynamic mechanism for AKAP binding to RII isoforms of cAMP-dependent protein kinase. *Molecular cell*, *24*(3), 397-408. https://doi.org/10.1016/j.molcel.2006.09.015

Knape, M. J., Ahuja, L. G., Bertinetti, D., Burghardt, N. C., Zimmermann, B., Taylor, S. S., & Herberg, F. W. (2015, Oct 16). Divalent Metal Ions Mg(2)(+) and Ca(2)(+) Have Distinct Effects on Protein Kinase A Activity and Regulation. *ACS Chem Biol*, *10*(10), 2303-2315. https://doi.org/10.1021/acschembio.5b00271

Kwon, H. B., & Sabatini, B. L. (2011, Jun 2). Glutamate induces de novo growth of functional spines in developing cortex. *Nature*, *474*(7349), 100-104. https://doi.org/10.1038/nature09986

Lee, H. K., Kameyama, K., Huganir, R. L., & Bear, M. F. (1998, Nov). NMDA induces long-term synaptic depression and dephosphorylation of the GluR1 subunit of AMPA receptors in hippocampus. *Neuron*, *21*(5), 1151-1162. https://doi.org/10.1016/s0896-6273(00)80632-7

Li, H., Pink, M. D., Murphy, J. G., Stein, A., Dell'Acqua, M. L., & Hogan, P. G. (2012, Feb 19). Balanced interactions of calcineurin with AKAP79 regulate Ca2+-calcineurin-NFAT signaling. *Nat Struct Mol Biol*, *19*(3), 337-345. https://doi.org/10.1038/nsmb.2238

Lu, Y., Zha, X. M., Kim, E. Y., Schachtele, S., Dailey, M. E., Hall, D. D., Strack, S., Green, S. H., Hoffman, D. A., & Hell, J. W. (2011, Jul 29). A kinase anchor protein 150 (AKAP150)-associated protein kinase A limits dendritic spine density. *J Biol Chem*, *286*(30), 26496-26506. https://doi.org/10.1074/jbc.M111.254912

Lu, Y., Zhang, M., Lim, I. A., Hall, D. D., Allen, M., Medvedeva, Y., McKnight, G. S., Usachev, Y. M., & Hell, J. W. (2008, Sep 1). AKAP150-anchored PKA activity is important for LTD during its induction phase. *J Physiol*, *586*(17), 4155-4164. https://doi.org/10.1113/jphysiol.2008.151662

Mo, G. C., Ross, B., Hertel, F., Manna, P., Yang, X., Greenwald, E., Booth, C., Plummer, A. M., Tenner, B., Chen, Z., Wang, Y., Kennedy, E. J., Cole, P. A., Fleming, K. G., Palmer, A., Jimenez, R., Xiao, J., Dedecker, P., & Zhang, J. (2017, Apr). Genetically encoded biosensors for visualizing live-cell biochemical activity at super-resolution. *Nat Methods*, *14*(4), 427-434. https://doi.org/10.1038/nmeth.4221

Moore, M. J., Adams, J. A., & Taylor, S. S. (2003, Mar 21). Structural basis for peptide binding in protein kinase A. Role of glutamic acid 203 and tyrosine 204 in the peptide-positioning loop. *J Biol Chem*, *278*(12), 10613-10618. https://doi.org/10.1074/jbc.M210807200

Mulkey, R. M., Endo, S., Shenolikar, S., & Malenka, R. C. (1994, Jun 9). Involvement of a calcineurin/inhibitor-1 phosphatase cascade in hippocampal long-term depression. *Nature*, *369*(6480), 486-488. https://doi.org/10.1038/369486a0

Murphy, J. G., Sanderson, J. L., Gorski, J. A., Scott, J. D., Catterall, W. A., Sather, W. A., & Dell'Acqua, M. L. (2014, Jun 12). AKAP-anchored PKA maintains neuronal L-type calcium channel activity and NFAT transcriptional signaling. *Cell Rep*, *7*(5), 1577-1588. https://doi.org/10.1016/j.celrep.2014.04.027

Ni, Q., Ganesan, A., Aye-Han, N. N., Gao, X., Allen, M. D., Levchenko, A., & Zhang, J. (2011, Jan). Signaling diversity of PKA achieved via a Ca2+-cAMP-PKA oscillatory circuit. *Nat Chem Biol*, *7*(1), 34-40. https://doi.org/10.1038/nchembio.478

Nygren, P. J., Mehta, S., Schweppe, D. K., Langeberg, L. K., Whiting, J. L., Weisbrod, C. R., Bruce, J. E., Zhang, J., Veesler, D., & Scott, J. D. (2017, Oct 2). Intrinsic disorder within AKAP79 fine-tunes anchored phosphatase activity toward substrates and drug sensitivity. *Elife, 6*. https://doi.org/10.7554/eLife.30872

Ogreid, D., & Doskeland, S. O. (1981, Jul 6). The kinetics of the interaction between cyclic AMP and the regulatory moiety of protein kinase II. Evidence for interaction between the binding sites for cyclic AMP. *FEBS Lett, 129*(2), 282-286. https://www.ncbi.nlm.nih.gov/pubmed/6269881

Patel, N., Stengel, F., Aebersold, R., & Gold, M. G. (2017, Nov 22). Molecular basis of AKAP79 regulation by calmodulin. *Nat Commun, 8*(1), 1681. https://doi.org/10.1038/s41467-017-01715-w

Perrino, B. A., Fong, Y. L., Brickey, D. A., Saitoh, Y., Ushio, Y., Fukunaga, K., Miyamoto, E., & Soderling, T. R. (1992, Aug 5). Characterization of the phosphatase activity of a baculovirus-expressed calcineurin A isoform. *J Biol Chem, 267*(22), 15965-15969. https://www.ncbi.nlm.nih.gov/pubmed/1322410

Qi, C., Sorrentino, S., Medalia, O., & Korkhov, V. M. (2019, Apr 26). The structure of a membrane adenylyl cyclase bound to an activated stimulatory G protein. *Science, 364*(6438), 389-394. https://doi.org/10.1126/science.aav0778

Qian, H., Patriarchi, T., Price, J. L., Matt, L., Lee, B., Nieves-Cintron, M., Buonarati, O. R., Chowdhury, D., Nanou, E., Nystoriak, M. A., Catterall, W. A., Poomvanicha, M., Hofmann, F., Navedo, M. F., & Hell, J. W. (2017, Jan 24). Phosphorylation of Ser1928 mediates the enhanced activity of the L-type Ca2+ channel Cav1.2 by the beta2-adrenergic receptor in neurons. *Sci Signal, 10*(463). https://doi.org/10.1126/scisignal.aaf9659

Rangel-Aldao, R., & Rosen, O. M. (1976, Jun 10). Dissociation and reassociation of the phosphorylated and nonphosphorylated forms of adenosine 3':5' -monophosphate-dependent protein kinase from bovine cardiac muscle. *J Biol Chem, 251*(11), 3375-3380. https://www.ncbi.nlm.nih.gov/pubmed/179996

Redden, J. M., & Dodge-Kafka, K. L. (2011, Oct). AKAP phosphatase complexes in the heart. *J Cardiovasc Pharmacol, 58*(4), 354-362. https://doi.org/10.1097/FJC.0b013e31821e5649

Roach, P. J., Depaoli-Roach, A. A., Hurley, T. D., & Tagliabracci, V. S. (2012, Feb 1). Glycogen and its metabolism: some new developments and old themes. *Biochem J, 441*(3), 763-787. https://doi.org/10.1042/BJ20111416

Rodriguez, A., Ehlenberger, D. B., Dickstein, D. L., Hof, P. R., & Wearne, S. L. (2008, Apr 23). Automated three-dimensional detection and shape classification of dendritic spines from fluorescence microscopy images. *PLoS One, 3*(4), e1997. https://doi.org/10.1371/journal.pone.0001997

Roy, J., & Cyert, M. S. (2009, Dec 8). Cracking the phosphatase code: docking interactions determine substrate specificity. *Sci Signal, 2*(100), re9. https://doi.org/10.1126/scisignal.2100re9

Sanderson, J. L., Gorski, J. A., & Dell'Acqua, M. L. (2016, Mar 2). NMDA Receptor-Dependent LTD Requires Transient Synaptic Incorporation of Ca(2)(+)-Permeable AMPARs Mediated by AKAP150-Anchored PKA and Calcineurin. *Neuron, 89*(5), 1000-1015. https://doi.org/10.1016/j.neuron.2016.01.043

Sanderson, J. L., Gorski, J. A., Gibson, E. S., Lam, P., Freund, R. K., Chick, W. S., & Dell'Acqua, M. L. (2012, Oct 24). AKAP150-anchored calcineurin regulates synaptic plasticity by limiting synaptic incorporation of Ca2+-permeable AMPA receptors. *J Neurosci, 32*(43), 15036-15052. https://doi.org/10.1523/JNEUROSCI.3326-12.2012

Schmitt, J. P., Kamisago, M., Asahi, M., Li, G. H., Ahmad, F., Mende, U., Kranias, E. G., MacLennan, D. H., Seidman, J. G., & Seidman, C. E. (2003, Feb 28). Dilated cardiomyopathy and heart failure caused by a mutation in phospholamban. *Science, 299*(5611), 1410-1413. https://doi.org/10.1126/science.1081578

Smith, F. D., Esseltine, J. L., Nygren, P. J., Veesler, D., Byrne, D. P., Vonderach, M., Strashnov, I., Eyers, C. E., Eyers, P. A., Langeberg, L. K., & Scott, J. D. (2017, Jun 23). Local protein kinase A action proceeds through intact holoenzymes. *Science, 356*(6344), 1288-1293. https://doi.org/10.1126/science.aaj1669

Stemmer, P. M., & Klee, C. B. (1994, Jun 7). Dual calcium ion regulation of calcineurin by calmodulin and calcineurin B. *Biochemistry, 33*(22), 6859-6866. https://doi.org/10.1021/bi00188a015

Taylor, S. S., Meharena, H. S., & Kornev, A. P. (2019, Jun). Evolution of a dynamic molecular switch. *IUBMB Life, 71*(6), 672-684. https://doi.org/10.1002/iub.2059

Tillo, S. E., Xiong, W. H., Takahashi, M., Miao, S., Andrade, A. L., Fortin, D. A., Yang, G., Qin, M., Smoody, B. F., Stork, P. J. S., & Zhong, H. (2017, Apr 18). Liberated PKA Catalytic Subunits Associate with the Membrane via Myristoylation to Preferentially Phosphorylate Membrane Substrates. *Cell Rep, 19*(3), 617-629. https://doi.org/10.1016/j.celrep.2017.03.070

Tulsian, N. K., Krishnamurthy, S., & Anand, G. S. (2017, Jun 20). Channeling of cAMP in PDE-PKA Complexes Promotes Signal Adaptation. *Biophys J, 112*(12), 2552-2566. https://doi.org/10.1016/j.bpj.2017.04.045

Tunquist, B. J., Hoshi, N., Guire, E. S., Zhang, F., Mullendorff, K., Langeberg, L. K., Raber, J., & Scott, J. D. (2008, Aug 26). Loss of AKAP150 perturbs distinct neuronal processes in mice. *Proc Natl Acad Sci U S A, 105*(34), 12557-12562. https://doi.org/0805922105 [pii] 10.1073/pnas.0805922105

Walker-Gray, R., Stengel, F., & Gold, M. G. (2017, Sep 26). Mechanisms for restraining cAMP-dependent protein kinase revealed by subunit quantitation and cross-linking approaches. *Proc Natl Acad Sci U S A, 114*(39), 10414-10419. https://doi.org/10.1073/pnas.1701782114

Weisenhaus, M., Allen, M. L., Yang, L., Lu, Y., Nichols, C. B., Su, T., Hell, J. W., & McKnight, G. S. (2010, Apr 23). Mutations in AKAP5 disrupt dendritic signaling complexes and lead to electrophysiological and behavioral phenotypes in mice. *PLoS One, 5*(4), e10325. https://doi.org/10.1371/journal.pone.0010325

Wild, A. R., Sinnen, B. L., Dittmer, P. J., Kennedy, M. J., Sather, W. A., & Dell'Acqua, M. L. (2019, Mar 26). Synapse-to-Nucleus Communication through NFAT Is Mediated by L-type Ca(2+) Channel Ca(2+) Spike Propagation to the Soma. *Cell Rep, 26*(13), 3537-3550 e3534. https://doi.org/10.1016/j.celrep.2019.03.005

Woolfrey, K. M., O'Leary, H., Goodell, D. J., Robertson, H. R., Horne, E. A., Coultrap, S. J., Dell'Acqua, M. L., & Bayer, K. U. (2018, Feb 2). CaMKII regulates the depalmitoylation and synaptic removal of the scaffold protein AKAP79/150 to mediate structural long-term depression. *J Biol Chem, 293*(5), 1551-1567. https://doi.org/10.1074/jbc.M117.813808

Xiong, W. H., Qin, M., & Zhong, H. (2021, Apr 13). Myristoylation alone is sufficient for PKA catalytic subunits to associate with the plasma membrane to regulate neuronal functions. *Proc Natl Acad Sci U S A, 118*(15). https://doi.org/10.1073/pnas.2021658118

Zhang, J., & Shapiro, M. S. (2012, Dec 20). Activity-dependent transcriptional regulation of M-Type (Kv7) K(+) channels by AKAP79/150-mediated NFAT actions. *Neuron, 76*(6), 1133-1146. https://doi.org/10.1016/j.neuron.2012.10.019

Zhang, J., & Shapiro, M. S. (2016, Jan 1). Mechanisms and dynamics of AKAP79/150-orchestrated multi-protein signalling complexes in brain and peripheral nerve. *J Physiol, 594*(1), 31-37. https://doi.org/10.1113/jphysiol.2014.287698

Zhang, J. Z., Lu, T. W., Stolerman, L. M., Tenner, B., Yang, J. R., Zhang, J. F., Falcke, M., Rangamani, P., Taylor, S. S., Mehta, S., & Zhang, J. (2020, Sep 17). Phase Separation of a PKA Regulatory Subunit Controls cAMP Compartmentation and Oncogenic Signaling. *Cell, 182*(6), 1531-1544 e1515. https://doi.org/10.1016/j.cell.2020.07.043

Zhang, P., Knape, M. J., Ahuja, L. G., Keshwani, M. M., King, C. C., Sastri, M., Herberg, F. W., & Taylor, S. S. (2015, Jul). Single Turnover Autophosphorylation Cycle of the PKA RIIbeta Holoenzyme. *PLoS biology, 13*(7), e1002192. https://doi.org/10.1371/journal.pbio.1002192

Zhang, P., Smith-Nguyen, E. V., Keshwani, M. M., Deal, M. S., Kornev, A. P., & Taylor, S. S. (2012, Feb 10). Structure and allostery of the PKA RIIbeta tetrameric holoenzyme. *Science, 335*(6069), 712-716. https://doi.org/10.1126/science.1213979

Zhang, X., Li, L., & McNaughton, P. A. (2008, Aug 14). Proinflammatory mediators modulate the heat-activated ion channel TRPV1 via the scaffolding protein AKAP79/150. *Neuron, 59*(3), 450-461. https://doi.org/10.1016/j.neuron.2008.05.015

Zhang, X., Pathak, T., Yoast, R., Emrich, S., Xin, P., Nwokonko, R. M., Johnson, M., Wu, S., Delierneux, C., Gueguinou, M., Hempel, N., Putney, J. W., Jr., Gill, D. L., & Trebak, M. (2019, Apr 29). A calcium/cAMP signaling loop at the ORAI1 mouth drives channel inactivation to shape NFAT induction. *Nat Commun, 10*(1), 1971. https://doi.org/10.1038/s41467-019-09593-0

Zhou, Q., Homma, K. J., & Poo, M. M. (2004, Dec 2). Shrinkage of dendritic spines associated with long-term depression of hippocampal synapses. *Neuron, 44*(5), 749-757. https://doi.org/10.1016/j.neuron.2004.11.011

Figure Legends

Figure 1. Effect of AKAP79 on pRII dephosphorylation by CN. (**A**) Dephosphorylation of the inhibitor sequence (IS, yellow) of RII subunits enables faster PKA C subunit capture. (**B**) AKAP79 contains anchoring sites for CN (red) and PKA RII subunits (blue) in its C-terminal region. Other macromolecular interactions are mediated through elements within its tandem polybasic regions (TPRs, grey). (**C**) CN-catalyzed phosphate release from pRIIα subunits with either no AKAP79, WT AKAP79 (light blue), or AKAP79 lacking the PIAIIIT anchoring motif ('ΔCN'). (**D**) CN-catalyzed phosphate release from pRIIβ subunits with either no AKAP79, WT AKAP79 (dark blue), or AKAP79 ΔCN. (**E**) The relationship between CN activity towards pRIIα subunits and pRIIα concentration with pRIIα subunits included either alone (black circles) or in complex with $AKAP79_{c97}$ (light blue squares). (**F**) The relationship between CN activity towards pRIIβ subunits and pRIIβ concentration with pRIIβ subunits included either alone (black circles) or in complex with $AKAP79_{c97}$ (dark blue squares). For panels E & F, activities at each concentration were measured in triplicate. Statistical comparisons were performed using two-tailed unpaired Student *t*-tests. ***$p<0.001$.

Figure 2. Quantitation of PKA subunits in CA1 neuropil. Images of a P17 rat hippocampal slice before (**A**) and after (**B**) micro-dissection of the CA1 neuropil layer. (**C**) Immunoblots of CA1 neuropil extract for PKA subunits. Extracts were run alongside reference amounts of the relevant purified PKA subunit in each immunoblot (***Figure 2-figure supplement 1***). In each case, 15 μg total protein extract was run alongside the reference series, with the exception of the anti-C immunoblot (10 μg extract). (**D**) Copy numbers of PKA subunits in rat CA1 neuropil normalized to C subunits.

Figure 3. FRET-based PKA activity measurements. (**A**) AKAR4 mechanism: phosphorylation of the sensor by PKA is detected as an increase in FRET between the terminal fluorescent proteins. (**B**) Concentrations of proteins used for *in vitro* AKAR4 assays. Different experiments utilized different mixtures of these proteins but always at these concentrations. (**C**) Representative AKAR4 traces showing change in 520 nm / 485 nm (Y/C) emission ratio over time after injection of different concentrations of cAMP in tandem with 5 mM ATP. All protein mixtures included AKAR4, type II PKA (RIIα, RIIβ, C), and CaM. Experiments were performed with either no further additives (top row, black), with CN added (middle row, blue), or with both CN and $AKAP79_{c97}$ added (bottom row, red). ATP/cAMP injections are indicated by arrows. (**D**) The chart shows peak rates of emission ratio change for the recordings shown in the preceding panel. n values are stated above the columns. (**E**)

For these recordings, type II PKA, CN, and CaM were included in all cases. Phosphorylation was initiated by injection of 5 mM ATP and 1 μM cAMP at t=0. Averaged responses ± standard error (SE) are shown with no further additives (blue), or when either WT (red), ΔCN (purple), or ΔPKA (gold) variants of $AKAP79_{c97}$ were included. **(F**) Peak rates (calculated between 30-90 s) for the responses shown in the preceding panel. Statistical comparisons were performed using two-tailed unpaired Student *t*-tests. ***p<0.001.

Figure 4. Kinetic analysis of PKA-CN-AKAP79 signaling. (**A**-**C**) Estimates of the average proportion of free C subunits between 30-90 s for type II PKA alone (black), with CN (blue), and with both CN and $AKAP79_{c97}$ (red) following activation of the protein mixtures with a range of cAMP concentrations. (**D**) Reaction scheme used for modeling type II PKA regulation by CN. Each species within the scheme is numbered consistent with supporting data in figure in ***Supplementary File 1***. (**E**-**G**) Model simulations for protein mixtures activated with 1 μM cAMP are shown with the experimental data overlaid. Averaged values are shown for experimental data after pooling the data shown in ***Figure 3***. Responses are shown for type II PKA alone (**E**), with CN (**F**), and with both CN and $AKAP79_{c97}$ (**G**). A sample of the corresponding simulated responses are shown in grey. An 'error' threshold of 0.01 was used to accept curves as a good fit.

Figure 5. Characterization of RIIα IS phosphorylation site mutations. (**A**) RIIα subunit topology showing locations of the docking and dimerization domain (D/D, grey), inhibitor sequence (IS, yellow), and tandem cyclic nucleotide binding domains (dark and light blue). S98A (red) and S98E (green) mutations in the IS are highlighted. (**B**-**D**) Comparison of AKAR4 emission ratio changes following 5 mM ATP/1 μM cAMP activation of protein mixtures containing either WT (**B**), S98A (**C**), or S98E (**D**) RIIα. 1.03 μM RIIβ was included in all cases. Measurements were collected either with or without CN in the reaction mixture. Averaged responses (± SE) are shown for WT RIIα with (dark blue) and without CN (light blue), S98A RIIα with (dark red) and without (light red) CN, and RIIα S98E with (dark green) and without (light green) CN. (**E**) The upper bar chart shows peak rates (calculated between 30-90 s) for the responses shown in panels b-d. The effect of including CN in the reaction mixture for each RII variant is shown in the lower bar chart. (**F**-**H**) Model predictions in the six conditions of panels b-d are shown in grey when simulating using the 'extended' model (see Methods) and using the different parameter sets generated from the parameter estimation approach. The same parameters as retrieved using data shown in figure 4 were used as a starting point for the simulations, but parameter sets were filtered based on data collected with RIIα S98A. Model

predictions are shown alongside the corresponding experimental data collected with either WT (**F**), S98A (**G**), or S98E (**H**) RII*α* in the reaction mix.

Figure 6. Lentivirus development and spine density imaging. (**A**) Schematic of the FUGW-H1-based lentiviral vector used to knock down and replace endogenous RIIα subunits in dissociated hippocampal cultures. (**B**) To validate lentiviruses, dissociated hippocampal neurons were infected on the seventh day *in vitro* (DIV7). Immunoblots are shown comparing neuronal extracts collected on DIV14 after infection with no virus, virus expressing scrambled shRNA only, shRIIα only, and the three complete lentiviruses for knockdown/replacement with either WT, S97A, or S97E RIIα. (**C**) Representative live-cell images of lentivirus-infected primary hippocampal neurons at DIV14 expressing either WT, S97A, or S97E RIIα. Scale bars correspond to 50 μm (upper panels) and 5 μm (lower panels). **(D**) Average spine density on hippocampal dendrites following lentiviral replacement of endogenous RIIα. Data were averaged from 106 (WT), 97 (S97A), and 113 (S97E) neurons derived from 7 rats for each condition, and are represented as mean ± SE. Conditions were compared using one-way ANOVA with Turkey post-hoc tests. (**E**) Representative live-cell images showing dendritic spines in primary hippocampal neurons expressing either WT, S97A, or S97E replacement RIIα at three points before and after chem-LTD (scale bar = 2.5 μm). Chem-LTD was induced at t=0 with 20 μM NMDA for 3 minutes. The yellow asterisk indicates a spine that disappeared over the course of the protocol whereas the pink asterisks indicate spines that did not. (**F**) Plot showing average changes in spine density (± S.E) in primary hippocampal neurons expressing either WT (dark blue), S97A (red) or S97E (green) RIIα. (**G**) Average changes in spine density ± SE one hour after induction of chem-LTD are shown for neurons expressing WT (dark blue, n=5), S97A (red, n=5), and S97E (green, n=4) RIIα variants as shown in the preceding two panels. Statistical comparisons were performed by 2-way ANOVA followed by Bonferroni's post-hoc test. ** $p<0.01$, *** $P<0.001$

Figure 7. Summary model of PKA suppression by CN within the AKAP79 complex. Structural and kinetic models (upper and lower panels, respectively) of signaling within the AKAP79 complex are shown under conditions of either low (**A**) or elevated Ca^{2+} (**B**). Elevated Ca^{2+} triggers CN (red) dephosphorylation of pRII (blue) which shifts C subunit capture from the left-hand square of the kinetic scheme to the right-hand square which features dephosphorylated forms of RII. The overall effect is a reduction in the concentration of free C subunits. The most abundant forms of RII under the two conditions are highlighted by blue spheres.

Supplementary Figure Legends

Figure 1-figure supplement 1. Purified proteins. Images showing the purity of purified proteins applied in this study are shown following SDS-PAGE with 4–12% Bis-Tris NuPAGE gels. (**A**) Full-length WT PKA RIIα and RIIβ subunits. (**B**) Full-length AKAP79. (**C**) The complex of RIIα and $AKAP79_{c97}$. (**D**) The complex of RIIβ and $AKAP79_{c97}$. (**E**) The CN heterodimer. (**F**) CaM. (**G**) AKAR4 – the left-hand image shows Coomassie staining whereas the right-hand image shows anti-GFP immunoblotting of an equivalent lane after transfer to nitrocellulose. (**H**) Variants of RIIα (WT, S98A, S98E) applied in AKAR4 assays. **(I**) Variants of $AKAP79_{c97}$ (WT, ΔCN, ΔPKA) applied in AKAR4 assays. All images were scanned following Coomassie staining unless otherwise stated.

Figure 1-figure supplement 2. pRII phosphorylation by CN at supra-physiological concentrations. The relationship between CN activity towards pRII and pRII concentration in the absence of AKAP79 is linear for both pRIIα (**A**) and pRIIβ (**B**) up to at least 20 μM pRII.

Figure 1-figure supplement 3. Effect of AKAP79c97 variants on pNPP and pRII phosphopeptide dephosphorylation. (A) Bar chart showing relative rates of pNPP hydrolysis by CN with (blue) and without (black) CaM activation, and for CN+CaM in the presence of WT (red), ΔCN (purple), and ΔPKA (gold) variants of $AKAP79_{c97}$. The relative rate of pNPP hydrolysis was reduced from 1 ± 0.04 to 0.19 ± 0.002 when CaM was excluded. Inclusion of WT $AKAP79_{c97}$ resulted in relative pNPP hydrolysis of 1.61 ± 0.02 (2 μM) and 1.69 ± 0.03 (10 μM); for the ΔCN variant, the rates were 1.00 ± 0.04 (2 μM) and 1.16 ± 0.01 (10 μM); and for the ΔPKA variant, the rates were 1.37 ± 0.02 (2 μM) and 1.44 ± 0.02 (10 μM). Taken together, the data indicate that the PIAIIIT motif of AKAP79 is able to weakly enhance CN hydrolysis of pNPP. (B) Bar chart showing relative rates of 40 μM pRII 19-mer peptide dephosphorylation by CN. Conditions are colored in the same way as the preceding panel. For pRII peptide, the relative rate of dephosphoylation was reduced from 1 ± 0.10 to 0.062 ± 0.01 when CaM was excluded. Inclusion of WT $AKAP79_{c97}$ resulted in relative dephosphorylation rates of 0.51 ± 0.06 (2 μM) and 0.47 ± 0.05 (10 μM); for the ΔCN variant, the rates were 0.92 ± 0.09 (2 μM) and 0.81 ± 0.09 (10 μM); and for the ΔPKA variant, the rates were 0.70 ± 0.07 (2 μM) and 0.66 ± 0.06 (10 μM). The data is consistent with previous reports that AKAP79 weakly inhibits CN activity towards pRII phosphopeptide (Coghlan et al., 1995; Kashishian et al., 1998).

Figure 2-figure supplement 1. Reference curves for quantitation of PKA subunits in CA1 neuropil. The four panels show reference curves (red lines) that relate immunoblot band intensity to ng of PKA subunit per lane, and correspond to the data shown in ***Figure 2***C. (**A**) Anti-pan C immunoblot reference curve. The point at which the neuropil extract lane falls on the curve is denoted by a green circle. (**B**) Anti-pan RI reference curve with neuropil extract lane denoted by a purple circle. (**C**) Anti-RIIα reference curve with neuropil extract lane denoted by a light blue circle. (**D**) Anti-RIIβ reference curve with the neuropil extract lane denoted by a dark blue circle.

Figure 3-figure supplement 1. AKAR4 reference measurements with PKA catalytic subunit. (**A**) Averaged AKAR4 traces showing change in 520 nm / 485 nm (Y/C) emission ratio over time after injection of 5 mM ATP into reactions containing only PKA C subunits at a range of concentrations. (**B**) Relationship between free C subunit concentration (in the absence of CN) and emission ratio change per minute. The data was fitted to a Hill function ($y = 380*x^{1.71}/(3481^{1.71}+x^{1.71})$) with an adjusted R-square value of 0.99983. (**C**) Averaged AKAR4 traces showing data for the same experiment as the preceding panel but with 1.5 μM CN included in all reactions. (**D**) Peak 520 nm / 485 nm (Y/C) emission ratio changes at different concentrations of C subunit, either without (black bars) or with (striped bars) 1.5 μM CN. Average rates were calculated between 15-75 s, with the exception of 0 and 25 nM C subunit concentrations (30 – 330 s). (**E**) Averaged peak AKAR4 responses from all recordings for type II PKA either alone (top row), with CN (middle row), or with both CN and AKAP collected after injections of 5 mM ATP with different concentrations of cAMP. These rates were cross-referenced against the reference curve shown in panel b to estimate free C subunit concentrations (plotted in ***Figure 4***A-C). Peak rates were calculated between 30-90 s, with the exception of 0 & 100 nM cAMP responses where a wider time window (30-330 s) was applied.

Figure 3-figure supplement 2. Comparison of CN and PP1 activity towards AKAR4. (A) AKAR4 responses are shown for reactions containing 400 nM C subunits alone (black), with 1.5 μM CN (blue), or with 1.5 μM PP1 (purple). Phosphorylation was initiated by injection of ATP to a final concentration of 5 mM. (B) Peak rates (calculated between 20-50 s after ATP injection) for the responses shown in the preceding panel. Inclusion of CN did not alter the rate (relative rates of 1 ± 0.05 for C alone compared to 1.02 ± 0.08 for C + CN), whereas addition of PP1 (purple) reduced the rate to 0.14 ± 0.04 (p = 9 x 10e-6). (C) We also compared rates of dephosphorylation of AKAR4 pre-phosphorylated by PKA. Reponses are shown for pAKAR4 dephosphorylation in the presence of no phosphatase (black) or with different concentrations of CN (blue) or PP1 (purple). (D) Peak rates for the data shown in the preceding panel. Replicate numbers for each condition are shown in parentheses. Rates are normalized to the

dephosphorylation rate with 1 μM PP1. The relative rates were as follows: 0.003 ± 0.001 with no phosphatase; with CN, 0.007 ± 0.001 (0.3 μM); 0.011 ± 0.001 (1 CN), and 0.033 ± 0.001 (3 μM); and with PP1, 0.15 ± 0.02 (0.1 μM), 0.44 ± 0.01 (0.3 μM), and 1 ± 0.09 (1 μM). The data indicate that PP1 is much more active towards pAKAR4 than CN, with 5-fold faster pAKAR4 dephosphorylation at the lowest PP1 concentration tested (0.1 μM) than the highest CN concentration (3 μM). The statistical comparison was performed using a one-tailed paired Student t-test. ***p<0.001.

Figure 4-figure supplement 1. Simulations of kinetic scheme species changes in concentration over time. Each row corresponds to the concentration (μM) of an individual species simulated in seven different reaction mixtures. The first three columns correspond to experiments with WT RIIα subunits; columns four and five to experiments with RIIα S98A subunits, and the last two columns with RIIα S98E subunits. Red lines correspond to simulations whose parameter sets were classified as far from experimental data collected with mutated RIIα, but which fit well to data collected with WT RIIα subunits in reactions stimulated with 0, 0.2, 1 and 2 μM cAMP. Blue traces correspond to simulations with parameter sets that generated results close to experimental data collected with both WT and mutant RIIα subunits.

Figure 4-figure supplement 2. Simulations of responses with different concentrations of cAMP. For each condition, simulations (grey lines) are shown alongside experimental data. The first four rows show responses with different concentrations of cAMP: 0 μM (top row), 0.2 μM (second row), 1 μM (third row), 2 μM (fourth row). The bottom row corresponds to responses at 1 μM with mixtures containing RIIα mutants.

Figure 5-figure supplement 1. Space of parameters used in model fitting. (**A**) The illustration shows the marginal posterior distribution of each model parameter on a logarithmic scale for a subset of parameter samples that generated simulations that fit experimental data collected with WT RIIα subunits. Each sample in the distribution is connected across the parameters by a line, whose color indicates whether the corresponding parameter set also generated simulations fitting closely (blue) to data collected with mutant RIIα subunits or not (red). The parameter priors are indicated by the respective black horizontal bars. (**B**) Distribution of dissociation constants (K_D's). The boxplots display median values (red lines), the 50 % datapoint distribution around the median (designated by boxes) and the remaining 25% datapoint distributions (lower and upper whiskers). Boxplots are shown for all eight K_D's obtained with the model priors (left), data fitted using experiments with WT RIIα subunits (middle), and parameters selected for fitting to data collected with RIIα S98A subunits. (**C**)

Marginal histograms for K_D76 (left) and K_D56 (right) with parameter sets classified according to whether they fit well to the RIIα S98A data (blue) or not (red). (**D**) Scatterplot showing how the K_D76 and K_D56 parameters are related according to the same two classes.

Supplementary File Legends

Supplementary File 1. Kinetic modeling parameters. The table lists parameters used in the computational modeling. Parameter terminology is according to the numbers above stated in ***Figure 4***B, e.g., k12 refers to the on rate of cAMP binding to state *1* (pRII-C) to produce state *2* (pRII-C-cAMP). The prior range used to constrain parameter estimation is provided for each parameter along with links to the references used to set the default values.

Supplementary File 2. Oligonucleotide primer sequences.

Legends for source data linked to figures

Figure 1-source data. Radioactive phosphatase assays
Figure 2-source data. Quantitative immunoblotting
Figure 3-source data. Rates of AKAR4 phosphorylation in purified protein mixtures
Figure 4-source data. Free C subunit calculations
Figure 5-source data. Rates of AKAR4 phosphorylation with mutant RIIα subunits
Figure 6-source data. Spine density quantitation
Figure 1-supplement 2. Phosphatase assays without AKAP79
Figure 1-supplement 3. Colorimetric phosphatase assays
Figure 3-supplement 1. Rates of AKAR4 phosphorylation with C subunit alone
Figure 3-supplement 2. Comparison of CN and PP1 activity towards pAKAR4

Legend for source data provided under 'Additional Files'

Source data. Original images of Coomassie-stained gels and immunoblots included in the manuscript

1351

AKAP79 enables calcineurin to directly suppress protein kinase A activity

Timothy W. Church[a], Parul Tewatia[b,c], Saad Hannan[a], João Antunes[b], Olivia Eriksson[b], Trevor G. Smart[a], Jeanette Hellgren Kotaleski[b,c], Matthew G. Gold[a,1]

[a]Department of Neuroscience, Physiology & Pharmacology, University College London, Gower Street, LONDON, WC1E 6BT, UK

[b]Science for Life Laboratory, School of Electrical Engineering and Computer Science, KTH Royal Institute of Technology, Stockholm, Sweden

[c]Department of Neuroscience, Karolinska Institute, Stockholm, Sweden

[1]Correspondence: m.gold@ucl.ac.uk

Abstract

Interplay between the second messengers cAMP and Ca^{2+} is a hallmark of dynamic cellular processes. A common motif is the opposition of the Ca^{2+}-sensitive phosphatase calcineurin and the major cAMP receptor, protein kinase A (PKA). Calcineurin dephosphorylates sites primed by PKA to bring about changes including synaptic long-term depression (LTD). AKAP79 supports signaling of this type by anchoring PKA and calcineurin in tandem. In this study, we discovered that AKAP79 increases the rate of calcineurin dephosphorylation of type II PKA regulatory subunits by an order of magnitude. Fluorescent PKA activity reporter assays, supported by kinetic modeling, show how AKAP79-enhanced calcineurin activity enables suppression of PKA without altering cAMP levels by increasing PKA catalytic subunit capture rate. Experiments with hippocampal neurons indicate that this mechanism contributes towards LTD. This non-canonical mode of PKA regulation may underlie many other cellular processes.

Introduction

Cyclic adenosine monophosphate (cAMP) and Ca^{2+} are ancient second messengers that are fundamental to the regulation of many dynamic cellular processes including synaptic plasticity (Huang et al., 1994), heart contraction (Bers et al., 2019), and glycogen metabolism (Roach et al., 2012). Crosstalk between the two second messengers is a common feature of cellular signaling. For example, cAMP can enhance cytosolic Ca^{2+} entry by triggering phosphorylation of key ion channels (Qian et al., 2017; Schmitt et al., 2003) by its major intracellular receptor cAMP-dependent protein kinase, also known as Protein Kinase A (PKA). Similarly, Ca^{2+} can regulate cAMP levels by altering activities of both phosphodiesterases (Baillie et al., 2019) and adenylyl cyclases (Qi et al., 2019). At the receptor level, a common signaling motif is the opposition of PKA and the highly-abundant Ca^{2+}-sensitive phosphatase calcineurin (CN), with CN triggering cellular changes by removing phosphate from substrates primed by PKA. Notable examples of this motif are the regulation of postsynaptic substrates including AMPA-type glutamate receptors in the induction of long-term depression (LTD) of synaptic strength (Bear, 2003), and control of NFAT nuclear localization in immune responses (Hogan, 2017). According to current consensus, in these cases CN dephosphorylates substrates without any requirement for directly altering PKA activity (Dittmer et al., 2014; Lu et al., 2011; Tunquist et al., 2008; Weisenhaus et al., 2010; Zhang & Shapiro, 2016). This implies that energetically-costly futile cycles of phosphate addition and removal by PKA and CN must persist to maintain dephosphorylated substrate. It would be more logical for PKA activity to be switched off when CN is activated during substrate dephosphorylation. Uncovering the mechanism to achieve this is the focus of this study.

Recent years have seen renewed interest in mechanisms for regulating the release and re-capture of PKA catalytic subunits (Bock et al., 2020; Gold, 2019; Zhang et al., 2020), including new data that hint at how CN might directly suppress PKA activity. PKA is comprised of regulatory subunit dimers that bind and sequester PKA catalytic (C) subunits in an inhibited state (Taylor et al., 2019). PKA regulatory subunits are classified into type I subunits (RIα and RIβ) that are predominantly cytosolic, and type II subunits (RIIα and RIIβ) that co-sediment with membranes (Gold, 2019). The regulatory subunit inhibitor sequence (IS) is phosphorylated upon association with C subunits for RII but not RI subunits, which bear alanine in place of serine in the phospho-acceptor site (S98 in RIIα). Quantitative immunoblotting and mass spectrometry (MS) have recently shown that PKA regulatory subunits – and particularly RII subunits – greatly outnumber PKA C subunits (Aye et al., 2010; Walker-Gray et al., 2017) throughout the body. In addition, Zhang and co-workers (Zhang et al., 2015) have extended earlier observations (Rangel-Aldao & Rosen, 1976) to quantify differences in the rate of C subunit binding to RII subunits either

phosphorylated (pRII) or dephosphorylated at the IS. Remarkably, the k_{on} rate for C subunit association is ~50 times faster for dephosphorylated RII than pRII (Zhang et al., 2015) (***Figure 1***A). In theory, rapid dephosphorylation of RII subunits by CN could directly suppress PKA activity by increasing the rate of C subunit capture thereby reducing the proportion of C subunits that are dissociated (Buxbaum & Dudai, 1989; Isensee et al., 2018; Ogreid & Doskeland, 1981; Stemmer & Klee, 1994; Zhang et al., 2015; Zhang et al., 2012). While recent observations concerning PKA subunit stoichiometry and pRII/RII binding kinetics support this notion, isolated pRII is a low affinity substrate for CN with a half-maximal substrate concentration (K_m) above 20 µM (Blumenthal et al., 1986; Perrino et al., 1992; Stemmer & Klee, 1994). Therefore, pRII dephosphorylation by CN would not be expected to occur to a meaningful degree at physiological concentrations in the absence of an additional factor.

Anchoring proteins support signal transduction by elevating effective local concentrations of signaling proteins, and therefore theoretically an AKAP might support pRII dephosphorylation by CN in cells (Gildart et al., 2020). A-kinase anchoring protein 79 (AKAP79; rodent ortholog AKAP150, gene name AKAP5) is a prototypical mammalian anchoring protein with several features that indicate it could operate in part by increasing the effective protein concentration of pRII subunits for CN. AKAP79 can simultaneously anchor both CN and PKA (Coghlan et al., 1995). It contains an amphipathic anchoring helix (Gold et al., 2006; Kinderman et al., 2006) for binding RII subunits, and a short linear 'PIAIIIT' CN anchoring motif (Dell'Acqua et al., 2002; Li et al., 2012). The two anchoring sites are separated by only ~50 amino acids in the primary sequence within the C-terminus of AKAP79 (***Figure 1***B). AKAP79 is localized in dendritic spines where it is required for anchoring RII subunits (Tunquist et al., 2008). The anchoring protein is necessary for both induction of long-term depression (LTD) of CA3-CA1 hippocampal synapses (Lu et al., 2008; Tunquist et al., 2008; Weisenhaus et al., 2010), and for CN-mediated dephosphorylation of NFAT (Kar et al., 2014; Murphy et al., 2014) – both processes that are driven by CN dephosphorylation of sites primed by PKA. Despite these characteristics, the possibility that AKAP79 could support pRII dephosphorylation by CN has been disregarded perhaps because paradoxically AKAP79 acts as a weak inhibitor for CN dephosphorylation of 20-mer peptides corresponding to the phosphorylated RII IS (Coghlan et al., 1995; Kashishian et al., 1998). We reasoned that these assays could be misleading since peptide substrates are not subject to anchoring alongside CN that occurs for full-length RII subunits. To resolve this issue, in this study we measured how AKAP79 alters CN activity towards full-length pRII subunits. We went on to determine if AKAP79 can reduce the fraction of dissociated C subunits in concert with CN using fluorescence-based assays supported by kinetic modeling, before substantiating our observations in hippocampal neurons.

Results

AKAP79 enables CN to efficiently dephosphorylate RII subunits at physiological concentrations

We set out to determine whether AKAP79 can increase CN dephosphorylation of full-length RII subunits phosphorylated at the IS. Using purified proteins (***Figure 1-figure supplement 1***), we compared ^{32}P release from either pRIIα (***Figure 1***C) or pRIIβ (***Figure 1***D). Thirty second reactions were initiated by addition of excess Ca^{2+}/calmodulin (CaM) to 10 nM CN and 400 nM pRII subunits. For pRIIα without AKAP79, phosphate was released from only 0.36±0.13 % of the subunits (black, ***Figure 1***C). Inclusion of full-length AKAP79 in the reaction mix increased phosphate release by 12.4-fold (p = 7.4x10^{-6}) to 4.52±0.26 % pRIIα subunits (light blue, ***Figure 1***C). Removing the PIAIIIT anchoring sequence in AKAP79 (ΔCN) returned dephosphorylation to a baseline level of 0.26±0.06 % (grey, ***Figure 1***C), consistent with a mechanism in which anchoring of CN adjacent to pRII subunits enhances the rate of dephosphorylation. Similar results were obtained for pRIIβ, with addition of AKAP79 increasing phosphate release 16.3-fold (p = 3.0x10^{-6}) from 0.34±0.13 % (black, ***Figure 1***D) to 5.49±0.17 % (dark blue, ***Figure 1***D). Ablating the CN anchoring site in AKAP79 also reduced phosphorylation to a baseline level of 0.2±0.02 % for this isoform (grey, ***Figure 1***D).

We next measured CN activity towards pRII over a range of pRII concentrations. We compared activity towards pRII subunits alone or in complex with a fragment of AKAP79 ($AKAP79_{c97}$) encompassing positions 331-427 that includes the CN and RII subunit anchoring sites. Working with this stable highly-expressed construct enabled us to purify sufficient quantities of pRIIα-$AKAP79_{c97}$ and pRIIβ-$AKAP79_{c97}$ complexes (***Figure 1-figure supplement 1***C & D) to sample concentrations up to 5 μM. In complex with $AKAP79_{c97}$, both pRIIα and pRIIβ acted as relatively high affinity substrates of CN. pRIIα-$AKAP79_{c97}$ (light blue, ***Figure 1***E) was dephosphorylated with a half-maximal concentration (K_m) of 1.36±0.16 μM and turnover number (k_{cat}) of 0.45±0.02 s^{-1}, and pRIIβ-$AKAP79_{c97}$ with K_m = 0.74±0.12 μM and k_{cat} = 0.24±0.01 s^{-1}. As expected, in the absence of the anchoring protein, pRIIα and pRIIβ subunits served as low affinity substrates for CN (black lines, ***Figure 1***E & F). For both isolated pRII isoforms, the relationship between phosphatase activity and pRII concentration was linear up to 20 μM (***Figure 1-figure supplement 2***) – the highest concentration tested – indicative of a K_m of greater than 20 μM. CN activity was very low (<0.03 s^{-1}) at concentrations of 5 μM pRII or lower. This is consistent with earlier studies that reported a K_m of 94 μM for CN dephosphorylation of a phosphorylated 19-mer peptide derived from the RIIα IS (Stemmer & Klee, 1994). We also compared CN activity towards para-nitrophenylphosphate (pNPP) and a peptide corresponding to the isolated phosphorylated RII inhibitor sequence (sequence DLDVPIPGRFDRRVpSVAAE) with and without variants of $AKAP79_{c97}$ (***Figure***

1-figure supplement 3). WT AKAP79$_{c97}$ enhanced CN activity towards pNPP by ~ 65 %, and reduced its activity towards pRII phosphopeptide by ~ 50 %, consistent with previous reports that AKAP79 acts as a weak inhibitor of CN activity towards this phosphopeptide (Coghlan et al., 1995; Kashishian et al., 1998). Enhanced CN activity towards pNPP in the presence of PxIxIT-type motifs that have the opposite effect on phosphopeptide dephosphorylation has also been observed previously (Grigoriu et al., 2013). Overall, our data are consistent with a mechanism in which AKAP79 enhances CN dephosphorylation of full-length RII subunits by increasing effective substrate concentration rather than by altering the inherent catalytic activity of the phosphatase.

To put our kinetic parameters for pRII dephosphorylation into a physiological context, we set out to determine accurate protein concentrations for PKA subunits in the CA1 neuropil where Schaffer collaterals from the CA3 region synapse onto CA1 dendrites (***Figure 2***A). These synapses are a leading prototype for understanding forms of LTD driven by CN following PKA priming (Bear, 2003). We collected hippocampal slices from 18-day old male Sprague-Dawley rats before micro-dissecting CA1 neuropil sections (***Figure 2***B). Following homogenization, concentrations of C, RIIα, RIIβ, and RI subunits in the extracted protein were determined using quantitative immunoblotting by running extracts (n=5) alongside reference concentrations of purified PKA subunits (***Figure 2***C, ***Figure 2-figure supplement 1***) (Walker-Gray et al., 2017). We found that RIIα was by far the most predominant PKA subunit in the CA1 neuropil, accounting for 0.32±0.029 % total protein content compared to 0.032±0.003 % for C subunits, 0.041±0.014 % for RI, and 0.06±0.006 % for RIIβ. These numbers equate to a 9.4-fold higher molar abundance of RIIα subunits (light blue, ***Figure 2***D) relative to C subunits with RI and RIIβ present at similar levels to C subunits. The predominance of the RIIα subunit is consistent with a previous imaging study of rodent hippocampus (Weisenhaus et al., 2010). Assuming that protein accounts for 8 % of total rat brain weight (Clouet & Gaitonde, 1956), we estimated RII subunit concentrations of 5.9 μM (RIIα) and 1.03 μM (RIIβ). These values fall within the range where CN efficiently dephosphorylates pRII only in the presence of AKAP79 (***Figure 1***E & F). Taken together our data therefore indicate that AKAP79 greatly enhances CN activity towards phosphorylated RII subunits at physiological concentrations.

AKAP79 enables calcineurin to suppress type II PKA activity

Given that AKAP79 supports rapid pRII dephosphorylation by CN, we hypothesized that the AKAP could enable CN to directly reduce the fraction of dissociated C subunits in mixtures of RII and C subunits. To test this hypothesis, we utilized purified A-kinase activity reporter 4 (AKAR4) (***Figure 3***A). PKA phosphorylation at threonine within the reporter's central 'LRRA**T**LVD' motif leads to a

conformational change that increases FRET efficiency between the terminal fluorescent proteins (***Figure 3***A)(Depry et al., 2011). All AKAR4 experiments were performed using purified protein mixtures in 96-well plates. For each recording, three baseline 520/485 nm emission ratios were measured prior to injection of ATP and the desired concentration of cAMP into the protein mixture to initiate phosphorylation. Emission ratios were collected once every 5 seconds (s) thereafter. In calibration experiments with AKAR4 and different concentrations of C subunit only (***Figure 3-figure supplement 1***A), we found that the initial rate of AKAR4 phosphorylation had a close to linear relationship to C subunit concentration up to 400 nM C subunit (***Figure 3-figure supplement 1***B). Full AKAR4 phosphorylation increased the emission ratio by 72 % (***Figure 3-figure supplement 1***A), consistent with previous studies (Depry et al., 2011). Importantly, supplementing these reactions with 1.5 μM activated CN had no detectable effect on AKAR4 phosphorylation rates, indicating that the phosphatase cannot efficiently dephosphorylate the reporter (Figure 3-***figure supplement 1***C & D). In comparison, supplementation with 1.5 μM PP1 reduced the phosphorylation rate by ~ 7-fold (***Figure 3-figure supplement 2***A & B). Phosphatase assays using pre-phosphorylated AKAR4 confirmed that CN exhibits very limited activity towards the reporter (***Figure 3-figure supplement 2***C & D), such that the reporter is well suited for experiments focusing on direct suppression of PKA activity by CN.

Next, we assembled purified protein mixtures with the aim of mimicking signaling involving PKA, CN, and AKAP79 in CA1 dendritic spines. RIIα, RIIβ, and C subunits were included at concentrations determined in CA1 neuropil extracts (**Figure 2)**. CaM was added at a molar excess of 5 μM, CN at 1.5 μM (Goto et al., 1986), and $AKAP79_{c97}$ – when included – at half the concentration of total RII subunits (summarized in ***Figure 3***B). RI subunits were omitted since they are not thought to be present in dendritic spines (Ilouz et al., 2017; Tunquist et al., 2008), and because the RI inhibitor site is not phosphorylated so cannot be regulated by CN. We first monitored AKAR4 phosphorylation in reactions containing RIIα, RIIβ, C, and CaM (black, ***Figure 3***C). Increasing the concentration of cAMP injected alongside ATP raised rates of AKAR4 phosphorylation as expected (black bars, ***Figure 3***D). Supplementing the reactions with CN led to small but consistent decreases in the rate of AKAR4 phosphorylation at all cAMP concentrations (blue, ***Figure 3***C & D). Rates were determined between 30-90 s in the linear early phase that followed a brief ~15 second delay, with the exception of the lowest two cAMP concentrations (0 & 100 nM), where relatively slow rates were calculated between 30-330 s. Additional supplementation with $AKAP79_{c97}$ markedly decreased the rate of AKAR4 phosphorylation (red, ***Figure 3***C). For example, with 1 μM cAMP activation, addition of both CN and the AKAP reduced the initial rate of AKAR4 phosphorylation by 2.8-fold from 18.9±0.6 to 6.7±0.8 % per minute (p = 0.0007, black and red bars, ***Figure 3***D). To confirm that AKAP79 enables CN to suppress PKA activity by anchoring it alongside RII

subunits, we investigated the effect of removing either the CN (positions 337-343) or PKA (391-400) anchoring sites. At 1 µM cAMP activation, addition of wild-type (WT) $AKAP79_{c97}$ (red, ***Figure 3***E & F) reduced the initial rate of AKAR4 phosphorylation by 2.06-fold (p = 2.7 x 10^{-11}) compared to supplementation with only CN (blue). Similar AKAR4 responses were obtained when either the AKAP was omitted altogether (blue, ***Figure 3***E & F), or if either the CN (purple) or PKA (orange) anchoring sites in the AKAP were removed. Overall, these AKAR4 measurements reveal that AKAP79 enables CN to robustly decrease type II PKA activity by anchoring the two enzymes together.

Mechanistic basis of PKA suppression by calcineurin and AKAP79

We next aimed to quantify how AKAP79 and CN changed the fraction of free C subunits in our reaction mixtures. To estimate this, we cross-referenced rates of AKAR4 phosphorylation recorded in the 'spine mimic' reaction mixtures (***Figure 3***C & E) to the reference curve (r = 0.998) obtained with only C subunits (***Figure 3-figure supplement 1***B). We focused on determining free C subunit concentrations during the early period of linear change (30-90 s for cAMP concentrations of 0.2 µM and above) where we assume the underlying kinetics are close to equilibrium. We calculated free C subunit concentrations following this approach using all available data between 0 to 2 µM cAMP (***Figure 3-figure supplement 1***E). The calculated proportion of C subunits that are dissociated at different cAMP concentrations are shown for type II PKA + CaM either alone (black, ***Figure 4***A), with CN (blue, ***Figure 4***B), or with both CN and $AKAP79_{c97}$ (red, ***Figure 4***C). Together, AKAP79 and CN reduced the proportion of free C subunits at equilibrium across the cAMP concentration range including from 47.8±1.5 to 20.2±0.8 % at 1 µM cAMP, and from 65.7±1.1 to 33.2±3.3 % at 2 µM cAMP (***Figure 4***A & C). The effect of adding CN alone was limited (***Figure 4***B), consistent with the much lower activity of the phosphatase towards pRII subunits in the low micromolar range (***Figure 1***E & F).

To understand at a deeper level how CN and AKAP79 reduce the fraction of free C subunits, we updated and extended a kinetic model (Buxbaum & Dudai, 1989) that takes into account transitions between pRII (left-hand square, ***Figure 4***D) and unphosphorylated RII subunits (right-hand square). The extended model also incorporates AKAR4 binding to and phosphorylation by free C subunits. We used a Bayesian approach (Eriksson et al., 2019) to estimate parameter sets for the model that could fit data pooled from AKAR4 recordings obtained after stimulation with 0, 0.2, 1 and 2 µM cAMP (***Figure 3***C & E). A log uniform prior parameter distribution was used as a starting point for the Bayesian method, where each parameter was allowed to vary three orders of magnitude around a default value (***Supplementary File 1***). The default values were taken from empirical data, including rates of pRII dephosphorylation determined in this study (***Figure 1***), and binding rates of C subunits to pRII and RII (Zhang et al., 2015). This

parameter estimation approach resulted in approximately 15,000 parameter sets that could explain the experimental data (***Figure 4***E-G). Simulations using these parameter sets enabled us to predict concentration changes of individual states within the model that cannot be determined experimentally (first three columns, ***Figure 4-figure supplement 1***). The model indicates that AKAP79 and CN together shift C subunit capture to the faster right-hand square sub-system (***Figure 4***D), driving down the fraction of free C subunits and thereby reducing PKA activity.

Mutation of the RIIα IS phosphorylation site occludes PKA suppression by CN

The results of the preceding sections show that AKAP79 targeting of CN for direct suppression of PKA is a viable mechanism for LTD induction. Previously published studies in hippocampal slices involving genetic manipulation of AKAP150 (the rodent ortholog of AKAP79) are also consistent with this mechanism. Full AKAP150 knock-out (Lu et al., 2008; Tunquist et al., 2008; Weisenhaus et al., 2010), or AKAP150 knock-in with variants lacking either the PKA or CN anchoring sites (Jurado et al., 2010; Sanderson et al., 2016), show that both AKAP150 anchoring sites are required for LTD induction. However, such approaches cannot distinguish between CN targeting to pRII subunits versus other substrates. If direct suppression of PKA activity by CN is essential for LTD induction, we reasoned that mutation of the IS phospho-acceptor S98 (***Figure 5***A) in the predominant RIIα isoform would be expected to disrupt LTD induction in CA1 neurons. To confirm this presupposition before undertaking experiments in neurons, we re-ran AKAR4 experiments at 1 µM cAMP substituting in either S98A or S98E RIIα. For each RIIα variant (***Figure 1-figure supplement 1***H), we compared responses with or without CN, with WT RIIβ and $AKAP79_{c97}$ present in all cases. For WT RIIα, addition of CN to the mixture decreased the peak rate of AKAR4 phosphorylation from 21.02±0.76 (light blue, ***Figure 5***B) to 8.24±0.79 % per minute (dark blue). Substituting in RIIα S98A generated slow rates of AKAR4 phosphorylation in both cases (6.30±0.44 % per min with CN, and 6.67±0.56 % without, ***Figure 5***C). Conversely, the peak rate of AKAR4 phosphorylation was high regardless of the presence of CN for the S98E RIIα variant (31.30±3.60 % per min without CN; 25.65±3.44 % with CN, ***Figure 5***D). Together, this data indicates that substituting in either mutant of RIIα in neurons would be expected to reduce LTD induction in neurons if direct suppression of PKA by CN is required in LTD induction (***Figure 5***E).

Before moving on to experiments in neurons, we used the data collected with RIIα variants to test the accuracy of our kinetic modeling. We ran simulations assuming that the S98A and S98E variants of RIIα would behave like dephosphorylated and phosphorylated forms of the regulatory subunit. Broadly, the simulations were in line with our experimental data and predicted that addition of CN would reduce PKA activity substantially more in the WT but not RIIα mutant conditions (***Figure 4-figure supplement 1***),

with low and high PKA activities regardless of CN concentration for the S98A and S98E variants, respectively. The model predictions for the extent by which AKAR4 phosphorylation was depressed in the RIIα S98A system were, however, spread out depending on the specific parameter set (column 4-5, ***Figure 4-figure supplement 1***). This implies that the WT data we used to constrain the model were not sufficient to precisely constrain the dynamics specifically for the unphosphorylated RII sub-system (right square, ***Figure 4***D) To understand the characteristics of those parameter sets that also reproduced the RIIα S98A behavior, we filtered the parameter sets returned by the parameter estimation approach into two classes depending on whether they fit closely (blue, ***Figure 4-figure supplement 1***) or not (red) to the acquired mutation data, yielding 526 parameter sets that fit closely to both the WT and mutation data. A pairwise coordinate plot (see ***Figure 5-figure supplement 1***A) shows that, except for a few parameters, the two classes do not appear to be visually distinct with regards to kinetic rates. However, analysis and subdivision of the eight model dissociation constants (K_D's) reveals interesting relationships (***Figure 5-figure supplement 1***B). Notably, as shown by the scatterplots for the K_D for interaction between RII-C and cAMP (K_D56), and RII-cAMP and C (K_D76) (***Figure 5-figure supplement 1***C), K_D56 should be relatively low within its range paired with a relatively high K_D76 (***Figure 5-figure supplement 1***D) to accurately mimic the biological workings of the PKA sub-system. This behavior may ensure that sufficient C subunit is released with increasing cAMP in our model when the kinetics are restrained to the unphosphorylated RII sub-system, i.e when the RIIα S98A mutation is introduced. Overall, simulations using unfiltered (top row, ***Figure 4-figure supplement 1***) and filtered (***Figure 5***F-H) parameter sets show that the kinetic model closely reproduces the experimental data, especially when further constrained using data collected with RIIα S98A. Furthermore, the constrained simulations reproduce the experimental data collected at different cAMP concentrations (***Figure 4-figure supplement 2***). Taken together, experiments and simulations with S98A and S98E variants of RIIα show that either of these mutations should prevent AKAP79 and CN from switching C subunit capture from the left-hand square sub-system to the faster right-hand square (***Figure 4***D). Therefore, either substitution would be expected to reduce LTD induction if the mechanism is important *in vivo*.

Disruption of RIIα phosphorylation in CA1 neurons impedes chemical LTD

To enable neuronal RIIα replacement experiments, we generated lentiviruses for shRNA-mediated knockdown of endogenous RIIα and simultaneous expression of shRNA-resistant RIIα variants in tandem with GFP. The lentiviruses contain an H1 promoter for expression of a highly-effective shRNA targeted to RIIα (***Figure 6***A). A UbC promoter drives expression of replacement RIIα sequences in tandem with GFP, with an internal ribosome entry sequence (IRES2) between the coding sequences of the two proteins enabling expression of GFP. We validated the lentiviruses in dissociated rat primary hippocampal neurons

by comparing the efficacy of five different lentiviruses. On day 7 *in vitro* (DIV7), we infected with control lentiviruses expressing either scrambled or shRIIα RNA, or with complete viruses for replacement of endogenous RIIα with either WT, S97A, or S97E (RIIα in rat is equivalent to S98 in human RIIα). Neuronal protein extracts were collected on DIV14, and analyzed using immunoblotting. Anti-RIIα immunoblotting (top row, ***Figure 6***B) confirmed effective suppression of endogenous RIIα with shRIIα (lane 3) but not scrambled RNA (lane 2), and strong expression of the replacement sequences (lanes 4-6). Expression of PKA C (row 2, ***Figure 6***B) and RIIβ subunits (row 3) was not affected by lentiviral infection in any case. Blocking PKA activity with H89 is known to prevent growth of new spines, whereas stimulating PKA with forskolin increases spine formation (Kwon & Sabatini, 2011). Replacing RIIα with the S97A variant – which has lower PKA activity regardless of CN activity (***Figure 5***F) – would therefore be expected to lead to a reduction in spines. To test this, we imaged dendritic spines on primary hippocampal neurons expressing either WT (left panel, ***Figure 6***C), S97A (middle panel), or S97E (right panel) RIIα. Consistent with a role for PKA in spinogenesis, spine density was reduced by 33.5 % (p=0.002) in neurons expressing the S97A variant to 1.17±0.11 spines per 10 μm compared to 1.76±0.12 for WT RIIα. Spine density for the S97E variant was similar to WT at 1.86±0.11 spines/10 μm.

To test whether the two substitutions at RIIα S97 affect LTD, we monitored changes in dendritic spine number during chemical LTD – a model of long-term synaptic depression that can be applied in dissociated neuronal cultures. Bath application of 20 μM NMDA for 3 minutes triggered a steady reduction in spine density (***Figure 6***E, top row) in neurons expressing WT RIIα as expected (Zhou et al., 2004), reaching a 20.4±1.6 %% reduction in spines after one hour (blue, ***Figure 6***F). In comparison, spine loss was attenuated in neurons expressing either the S97A (***Figure 6***E, middle row) or S97E (bottom row) RIIα variants. Spine numbers were reduced by only 9.07±0.96 % in neurons expressing RIIα S97A (red line, ***Figure 6***F), and by 9.90±1.8 % for the S97E variant (green line). The residual LTD in both conditions may correspond to action of CN on substrates other than pRII subunits, and limited suppression of PKA activity through CN dephosphorylation of the relatively small number of WT RIIβ subunits that are present in all cases. Overall, attenuation of spine loss in neurons expressing either S97A (p=0.00046) or S97E (p=0.0014) RIIα compared to WT subunits is consistent with an important role for direct PKA activity suppression by CN during the induction of LTD.

Discussion

The observations in this study support a revised mechanism for CN-mediated long-term depression in CA1 model synapses. AKAP79/150 is critical for anchoring PKA in dendritic spines (Tunquist et al., 2008; Weisenhaus et al., 2010) through association with RII subunits, which are the predominant neuronal PKA subunit in ~11-fold molar excess of C subunits in the CA1 neuropil (***Figure 2***D). Imaging studies (Ilouz et al., 2017; Weisenhaus et al., 2010) are consistent with our quantitative immunoblotting data, which show that RIIα is the major RII isoform in the CA1 neuropil. pRII dephosphorylation is limited prior to Ca^{2+} stimulation (***Figure 7***A), enabling a tonic level of dissociated C subunits sufficient to basally phosphorylate postsynaptic substrates in dendritic spines such as GluA1 subunits of AMPA-type glutamate receptors (Bear, 2003). LTD is brought about by CN (Mulkey et al., 1994), which is activated by Ca^{2+} entering spines through NMDA-type glutamate receptors (***Figure 7***B). AKAP79/150 contains a 'PIAIIIT' CN anchoring motif that is necessary for LTD (Jurado et al., 2010; Sanderson et al., 2012). In addition to potentially targeting CN to postsynaptic substrates including GluA1 subunits, the PIAIIIT anchoring motif positions CN adjacent to pRII subunits where it can efficiently dephosphorylate them (***Figure 7***B). This enables CN to increase the concentration of dephosphorylated RII species (blue spheres in the kinetic scheme shown in ***Figure 7***B) thereby directly suppressing PKA activity by increasing the rate of PKA C subunit capture. Consistent with this mechanism, blocking regulation of RII phosphorylation state by introducing mutations that mimic either the phosphorylated or dephosphorylated forms of the IS reduces LTD in cultured hippocampal neurons.

Our discovery that CN can directly suppress PKA activity in the AKAP79 complex reconciles three aspects of AKAP79 structure and function that had been enigmatic and paradoxical. First, previous studies showed that AKAP79 acts as a weak inhibitor of CN towards peptide substrates including a 20-mer peptide encompassing the phosphorylated RII IS (Coghlan et al., 1995; Kashishian et al., 1998), apparently at odds with the functional requirement for the anchoring protein in targeting CN to bring about LTD. We show that the key substrate for CN is likely to be full-length pRII subunits, and that in fact AKAP79 enhances the activity towards pRII at physiological concentrations by more than ten-fold. A second enigmatic feature of AKAP79 is its CN anchoring motif, PIAIIIT, which includes an additional central residue compared to the typical PxIxIT motif (Roy & Cyert, 2009). In a crystal structure of CN in complex with a peptide corresponding to AKAP79 positions 336-346, the additional leucine supports simultaneous binding of two copies of CN on either side of the motif (Li et al., 2012). Native mass spectrometry measurements of a purified AKAP79-CN-CaM-RIIα D/D complex also support a stoichiometry of 2 CN to 1 AKAP79 (Gold et al., 2011), although solution measurements indicate that when full-length RII subunits are bound to AKAP79, only one copy of CN can bind at a time (Li et al., 2012; Nygren et al., 2017). One possible explanation for this behavior is that CN binds transiently to

either side of the AKAP79 PIAIIIT motif enabling it to access both protomers of RII anchored to AKAP79 for efficient pRII dephosphorylation (cartoon representations in ***Figure 7***). This idea is consistent with data showing that mutating the PIAIIIT motif to a high-affinity canonical PxIxIT motif impairs the function of the phosphatase (Li et al., 2012), although it should be noted that it is not possible to determine whether two-sided CN binding to AKAP79 is necessary using the data presented here. Third, existing models of AKAP79 function assume that CN anchored to AKAP79 overcomes PKA phosphorylation at substrates with no reduction in PKA phosphorylation rate. In our revised mechanism, CN directly suppresses PKA activity when removing phosphate from substrates primed by PKA thereby avoiding energetically-costly ongoing futile cycling of phosphorylation and dephosphorylation by PKA and CN at these sites.

A challenge in the future will be to understand how the mechanism uncovered here relates to the full complexity of AKAP79 function. AKAP79 is directly regulated by Ca^{2+}/CaM, which binds to a 1-4-7-8 hydrophobic motif (Patel et al., 2017) starting at position W79. Binding of Ca^{2+}/CaM releases AKAP79 from the postsynaptic membrane (Dell'Acqua et al., 1998) and alters the conformation of the signaling complex by triggering formation of a second interface between CN and AKAP79 that involves an LxVP-type motif in AKAP79 (Gold et al., 2011; Nygren et al., 2017). Furthermore, metal ions including Ca^{2+} alter rates of substrate binding and product release from PKA C subunits (Knape et al., 2015; Zhang et al., 2015). Therefore, it will be important to understand the sensitivity of CN suppression of PKA activity to Ca^{2+} signals. Membrane targeting sequences regulate several components of the AKAP79 signaling complex. Myristylation of C subunits is important for limiting their diffusion rate in dendritic spines and concentrating PKA activity at the cell membrane (Tillo et al., 2017; Xiong et al., 2021). Localization of AKAP79 is also regulated by palmitoylation at C36 and C139 (Delint-Ramirez et al., 2011; Keith et al., 2012). Palmitoylation is required for endosomal localization of AKAP79, and AKAP79 depalmitoylation and synaptic removal is additionally regulated by CaMKII (Woolfrey et al., 2018). Our work suggests that removal of AKAP79 from synapses might be synchronized with accumulation of inhibited C subunits in the AKAP79 complex. Given that RII subunits greatly outnumber C subunits, movement of C subunits between different RII sub-populations, including RII subunits anchored to MAP2 in dendritic shafts (Tunquist et al., 2008), should also be considered along with PDEs that can terminate cAMP signals with high spatiotemporal precision (Bock et al., 2020; Tulsian et al., 2017). Non-dissociative activation of anchored type RII PKA has been put forward as an alternative mechanism to explain localised PKA activity (Smith et al., 2017). Current evidence indicates that C subunits do dissociate in neurons upon elevation of cAMP (Gold, 2019; Mo et al., 2017; Tillo et al., 2017), but it is important to note that suppression of PKA by pRII dephosphorylation is compatible with non-dissociative models of PKA

activation and this might occur in certain physiological settings. AKAP79 is a highly multivalent protein – other notable documented interaction partners include protein kinase C (Hoshi et al., 2010) and the Ca^{2+}-activated cyclase AC8 (Baldwin & Dessauer, 2018; Zhang et al., 2019). Oscillations of Ca^{2+}, cAMP, and PKA activity have been observed in pancreatic β-cells (Hinke et al., 2012; Ni et al., 2011), and knockout of AKAP150 leads to the loss of cAMP oscillations in β-cells upon stimulation with insulin (Hinke et al., 2012). CN dephosphorylation of pRII subunits bound to AKAP79 is likely to play a role in oscillatory patterns of PKA activity, and it will be important to understand how this mechanism underlies responses to short-lived and oscillatory changes in Ca^{2+} and cAMP concentration.

In this combined experimental-computational study, we focused on AKAP79 signaling in dendritic spines on the basis that this could serve as a prototype for understanding a potentially widespread non-canonical mechanism for altering PKA. In addition to its role in dendritic spines, AKAP79 regulates many different membrane channels and receptors following Ca^{2+} influx through a variety of sources, and the mechanism that we have uncovered here is likely to at least extend to these additional contexts. For example, AKAP79 underlies $GABA_A$ receptor regulation during LTD of GABAergic synapses (Dacher et al., 2013), and it positions PKA and CN for regulation of TRPV channels (Zhang et al., 2008), Kv7 channels (Zhang & Shapiro, 2012), and both β-adrenergic receptor isoform (Houslay & Baillie, 2005). AKAP79 is also necessary for NFAT dephosphorylation following Ca^{2+} entry through both L-type calcium channels (Wild et al., 2019) and the store-operated Ca^{2+} channel ORAI1 (Kar et al., 2014). The RII IS phosphorylation site is conserved throughout the animal kingdom, and co-anchoring of phosphatases alongside PKA is a feature of several AKAP complexes (Redden & Dodge-Kafka, 2011). Future investigations may therefore explore whether additional anchoring proteins are able to direct CN – or other cellular phosphatases – for direct suppression of PKA activity.

Methods & Materials

Key Resources Table

Key Resources Table				
Reagent type (species) or resource	**Designation**	**Source or reference**	**Identifiers**	**Additional information**
strain, strain background (*Escherichia coli*)	TOP10 chemically competent	Life Technologies	Cat# C404003	
strain, strain background (*Escherichia coli*)	BL21 (DE3)	Thermo Fisher Scientific	Cat# EC0114	
strain, strain background (*Escherichia coli*)	BL21 Tuner (DE3) pLysS	Merck	Cat# 70624	
strain, strain background (*Escherichia coli*)	BL21 Star (DE3)	Thermo Fisher Scientific	Cat# C601003	
strain, strain background (*Escherichia coli*)	*Stbl3*	Thermo Fisher Scientific	Cat# C737303	

cell line (*Homo-sapiens*)	HEK293	Horizon Discovery LTD	Cat# HCL3417	Myocplasma tested.
cell line (*Homo-sapiens*)	HEK293T	ATCC	Cat# CRL-3216	Myocplasma tested.
biological sample (*Rattus norvegicus*)	Sprague Dawley	UCL breeding colony	Not applicable	
antibody	(Mouse monoclonal) anti-PKA RIIα	BD Biosciences	Cat# 612243; RRID:AB_399566	(0.8 µg/mL)
antibody	(Mouse monoclonal) anti-PKA RIIβ	BD Biosciences	Cat# 610626; RRID:AB_397958	(0.8 µg/mL)
antibody	(Mouse monoclonal) anti-PKA C (pan)	BD Biosciences	Cat# 610981; RRID:AB_398294	(0.5 µg/mL)
antibody	(Mouse monoclonal) anti-PKA RI (pan)	BD Biosciences	Cat# 610166; RRID:AB_397567	(0.8 µg/mL)
antibody	(Rabbit monoclonal) anti-PKA phospho-RIIα	Abcam	Cat# ab32390; RRID:AB_779040	(0.8 µg/mL)
antibody	(Rabbit polyclonal) anti-GFP	Sigma Aldrich	Cat# SAB4301138; RRID:AB_2750576	(0.5 µg/mL)
antibody	(Mouse monoclonal) anti-β-tubulin	Biolegend	Cat# 903401; RRID: AB_2565030	(0.5 µg/mL)

antibody	Goat anti-rabbit HRP-linked secondary antibody	Cell Signalling Technology	Cat # 7074S; RRID:AB_2099233	(1 μg/mL)
antibody	Goat anti-mouse IgG (H+L) poly-HRP secondary antibody	Thermo Fisher Scientific	Cat# 32230; RRID:AB_1965958	(1 μg/mL)
recombinant DNA reagent	pIRES2-EGFP	Clontech	Cat# 6029-1	
recombinant DNA reagent	pFUGW-H1	Sally Temple lab/Addgene	Cat# 25870; RRID:Addgene_25870	Lentiviral entry vector.
recombinant DNA reagent	pFUGW-shRIIα-RIIα*-WT-IRES-EGFP	This study	Not applicable	Lentivral entry vector. Dr. Matthew G. Gold (University College London)
recombinant DNA reagent	pFUGW-shRIIα-RIIα*-S97A-IRES-EGFP	This study	Not applicable	Lentivral entry vector. Dr. Matthew G. Gold (University College London)
recombinant DNA reagent	pFUGW-shRIIα-RIIα*-S97E-IRES-EGFP	This study	Not applicable	Lentivral entry vector. Dr. Matthew G. Gold (University College London)
recombinant DNA reagent	pCMVdR8.74 & pMD2.G plasmids	Didier Trono lab/Addgene	Cat# 12259; RRID:Addgene_12259	Lentiviral packaging vectors
recombinant DNA reagent	pcDNA3.1-AKAR4-NES	Jin Zhang lab/Addgene	Cat# 64727; RRID:Addgene_64727	
chemical compound, drug	Lipofectamine 2000	Thermo Fisher Scientific	Cat# 11668019	

chemical compound, drug	DMEM, high glucose, pyruvate	Thermo Fisher Scientific	Cat # 41966029	
chemical compound, drug	Trypsin	Thermo Fisher Scientific	Cat# 25300054	
chemical compound, drug	Penicillin/ Streptomycin	Thermo Fisher Scientific	Cat# 15140122	
chemical compound, drug	GlutaMAX	Thermo Fisher Scientific	Cat# 35050061	
chemical compound, drug	DPBS, no calcium, no magnesium	Thermo Fisher Scientific	Cat# 14190144	
chemical compound, drug	HBSS	Thermo Fisher Scientific	Cat# 14185045	
chemical compound, drug	Heat-inactivated horse serum	Gibco	Cat# 26050088	
chemical compound, drug	Neurobasal-A medium	Thermo Fisher Scientific	Cat# 10888022	
chemical compound, drug	B27 supplement	Gibco	Cat# 17504044	
chemical compound, drug	Poly-L-Lysine	Sigma Aldrich	Cat# P2636	

chemical compound, drug	Boric acid	Sigma Aldrich	Cat# B6768-500g	
chemical compound, drug	Sodium tetraborate	Sigma Aldrich	Cat# 221732	
chemical compound, drug	cOmplete, Mini, EDTA-free Protease Inhibitor Cocktail	Roche	Cat# 11836170001	
chemical compound, drug	PhosSTOP phosphatase inhibitor tablets	Roche	Cat# 4906845001	
chemical compound, drug	Para-nitrophenylphosphate	Sigma Aldrich	Cat# N3254	
software, algorithm	Origin	OriginLab	www.originlab.com; RRID:SCR_014212	
software, algorithm	Reader Control Software for FLUOStar Omega	BMG Labtech	https://www.bmglabtech.com/reader-control-software/	
software, algorithm	MARS Data Analysis Software	BMG Labtech	https://www.bmglabtech.com/mars-data-analysis-software/	
software, algorithm	Unicorn Start 1.1 Software for controlling AKTA start system	GE Healthcare	Cat# 29225049	
software, algorithm	ImageJ (version 1.52)	NIH	RRID:SCR_003070	

software, algorithm	NeuronStudio	(Rodriguez et al., 2008)	https://icahn.mssm.edu; RRID:SCR_013798	

Protein expression and purification. Human PKA subunits were expressed and purified as described previously (Walker-Gray et al., 2017). GST-RIIα and GST-RIIβ were expressed in *Escherichia coli* BL21 Tuner (DE3) pLysS, and GST-Cβ in *E. coli* BL21 (DE3) grown in LB. In all cases, protein expression was induced by addition of 0.5 mM isopropyl β-D-1-thiogalactopyranoside (IPTG), and bacteria were harvested following overnight incubation at 20 °C. Cell pellets were thawed and sonicated in glutathione sepharose binding buffer (20 mM HEPES pH 7.5, 500 mM NaCl, 1 mM DTT, 0.5 mM EDTA, 1 mM benzamidine, 10 % glycerol) supplemented with 0.1 mg/mL lysozyme, and 0.1 % Igepal CA-630 (RII subunit preps only). Clarified lysates were incubated with glutathione sepharose 4B, and PKA subunits were eluted by overnight cleavage with PreScission protease thus removing N-terminal GST affinity tags. Finally, each subunit was purified using a HiLoad 16/600 Superdex 200 column connected in series with a GSTrap to remove residual GST using gel filtration buffer (20 mM HEPES pH 7.5, 150 mM NaCl, 5 % glycerol). S98A and S98E point mutations were introduced into RIIα subunits by site-directed mutagenesis (SDM) with primer pairs hS98A_F & R, and hS98E_F & R. RIIα variants were expressed and purified in the same way as the WT sequences.

Full-length human AKAP79 was cloned into pET28 using primers Nde1_AKAP79_1 and AKAP79_427_EcoRI for expression of N-terminally 6His-tagged protein. AKAP79 was expressed in 4 L BL21 Star (DE3) cells by overnight incubation at 37 °C in auto-induction media (AIM). PBS-washed bacterial pellets were resuspended in Talon binding buffer (30 mM Tris pH 8.0, 500 mM NaCl, 10 mM imidazole, 1 mM benzamidine) supplemented with 0.1 mg/mL lysozyme and one Complete EDTA-free protease inhibitor tablet (Roche) per 100 mL. Lysates were sonicated, clarified by centrifugation, and incubated with Talon Superflow resin for 2 hours prior to 3 x 10 mL washing in Talon binding buffer, and eluted with 2 x 2.5 mL Talon elution buffer (30 mM Tris, pH 7.0, 500 mM NaCl, 300 mM imidazole, 1 mM benzamidine). Eluted protein was exchanged into Q buffer A (20 mM Tris pH 8, 20 mM NaCl, 1 mM EDTA, 2 mM DTT) using a HiPrep 26/10 desalting column to enable purification using a 1 mL Resource Q column. Each variant was eluted using a NaCl/pH gradient with Q buffer A and a steadily increasing proportion of Q buffer B (20 mM Tris pH 7, 500 mM NaCl, 1 mM EDTA, 2mM DTT). In the final step, peak fractions were pooled and buffer exchanged into gel filtration buffer. Residues 331-427 of AKAP79 were cloned into pET28 using primers Nde1_AKAP79_331 and AKAP79_427_EcoRI for expression of the fragment AKAP79$_{c97}$ bearing an N-terminal His tag. This construct was transformed

into BL21 (DE3) cells, which were grown overnight at 37 °C in AIM. Lysis and metal affinity steps were as for full-length AKAP79 with the exception that Ni-NTA agarose (Life Technologies) was used in place of Talon resin. Following elution from Ni-NTA resin, the protein was purified by size exclusion using a HiLoad 16/600Superdex 200 pre-equilibrated in gel filtration buffer. To assemble complexes of full-length RII subunits and $AKAP79_{c97}$, mixtures of the purified proteins were incubated on ice in gel filtration buffer for 1 h with the AKAP fragment in a 2:1 molar excess. The complex was then separated from excess $AKAP79_{c97}$ by Superdex 200 size exclusion. pET28-$AKAP79_{c97}$ ΔCN was generated by performing PCR with an earlier construct lacking residues 337-343 as the template (Gold et al., 2011), whereas the ΔPKA variant (lacking residues 391-400) was generated by SDM with primers ΔPKA_F & _R. The two $AKAP79_{c97}$ deletion mutants were expressed and purified in the same way as the WT protein.

Human CN was expressed from a bicistronic pGEX6P1 vector (Gold et al., 2011) in *E. coli* BL21 Tuner (DE3) pLysS cells. Protein expression was induced by overnight incubation at 37 °C in 4L AIM. CN was purified following the same protocol as full-length PKA RII subunits, with the final size exclusion step performed using gel filtration buffer supplemented with 1 mM DTT. Human CaM was expressed and purified as described previously (Patel et al., 2017). Briefly, untagged CaM was expressed in *E. coli* BL21 (DE3) cells incubated overnight at 37 °C in AIM. CaM was initially purified using phenyl sepharose resin, then by ion exchange with a HiTrap Q HP column. Finally, CaM was exchanged into water and lyophilized prior to storage at -80 ºC. Human PP1α (7-300) was expressed in BL21 (DE3) *E. coli* in LB media supplemented with 1 mM $MnCl_2$ and purified as described previously (Kelker et al., 2009). The PP1 expression vector was a gift from Wolfgang Peti (Addgene plasmid # 26566). This vector was co-transformed with pGRO7 plasmid encoding the GroEL/GroES chaperone (Takara). PP1 expression was induced with 0.1 mM IPTG after prior induction of chaperone expression using 2 g/L arabinose. Bacteria were incubated for 20 hours at 10 °C following IPTG induction before harvesting. PP1 was purified by affinity to Ni-NTA agarose (Qiagen) followed by size exclusion with a Superdex 200 column equilibrated in PP1 gel filtration buffer (25 mM HEPES pH 7.5, 500 mM NaCl, 1 mM $MnCl_2$, 10% glycerol). For AKAR4 purification, an 8His epitope tag was ligated into pcDNA3.1-AKAR4-NES vector (Depry et al., 2011) (Addgene cat no. 64727) at the C-terminus of the sensor immediately prior to the nuclear export site using primers EcoI_8HisNLS_XbaI and XbaI_8HisNLS_EcoRI. The vector was transfected into 20 x 10 cm dishes of HEK293T cells cultured in DMEM using lipofectamine-2000 (Thermo Fisher Scientific). Cells were collected after 3 days, washed in PBS, then lysed in Talon binding buffer supplemented with 0.5 % Igepal CA-630, and sonicated briefly. AKAR4 was purified by affinity to Ni-NTA agarose following the same procedure as for AKAP79, and eluted protein was exchanged into gel filtration buffer, and aliquoted before storage at -80 ºC. All purification columns and resins were

purchased from GE Healthcare. All protein samples were concentrated using Vivaspin centrifugal concentrators (Sartorius). Denaturing gel electrophoresis was performed using NuPAGE 4-12 % Bis-Tris gels (Thermo Fisher Scientific), and protein concentrations were determined using the bicinchoninic acid (BCA) assay. Oligonucleotide primer sequences are listed in Supplementary File 2.

Phosphatase assays. For radioactive release assays, CN substrates were prepared by phosphorylating PKA RII subunits at the autoinhibitory site with PKA C subunit and ATP(γ-^{32}P). To radiolabel RIIα, RIIβ, or the purified complexes of each isoform with AKAP79$_{c97}$, 50 μg of the relevant sample was incubated in 100 μL with phosphorylation buffer (20 mM HEPES pH 7.5, 150 mM NaCl, 100 μM cAMP, 5 mM $MgCl_2$, 0.03 μg/μL C subunit) supplemented with 42 pmol [^{32}P-γ]-ATP at 3000 Ci/mmol and 10 μM cold ATP. After 15 min incubation at 30 °C, reactions were supplemented with 10 μM additional cold ATP. Following 15 min further incubation, reactions were finally supplemented up to 1 mM cold ATP for 10 min further incubation. ^{32}P-labelled protein was immediately separated from free ^{32}P using Sephadex G-25 Medium equilibrated in phospho-substrate storage buffer (20 mM HEPES pH 7.5, 150 mM NaCl, 10 % glycerol, 0.1 mM EDTA). Additional cold phospho-labelled substrates were prepared using scaled-up reactions with 1 mM cold ATP for 30 min at 30 °C.

Phosphatase assays using ^{32}P-labelled substrate (final volume 50 μL per assay) were prepared by first mixing appropriate dilutions of pRII substrates and CN on ice in dilution buffer (25 mM Na HEPES pH 7.5, 150 mM NaCl) to a final volume of 35 μL. 10 μL of reaction buffer (25 mM Na HEPES pH 7.5, 150 mM NaCl, 25 mM $MgCl_2$, 5 mM DTT, 0.5 mg/mL BSA, 1 mM EDTA) was then added before initiation of CN activity by addition of 5 μL activator mix (25 mM Na HEPES pH 7.5, 150 mM NaCl, 10 mM $CaCl_2$, 50 μM CaM). Assays was terminated after 30-60 s at 30 °C by addition of 350 μL 30 % trichloroacetic acid (TCA). Samples were then incubated on ice for 1 h, and protein was pelleted by centrifugation at 31,360 × *g* for 15 min at 2 °C. The separated supernatant and pellet were analyzed using a Beckman LS 6000SC scintillation counter to determine the fraction of phosphate released from the pRII substrate. Reaction conditions were optimized so that less than 10 % pRII was dephosphorylated in each assay. Assays were generally performed with 10 nM CN and terminated after 30 s, with the exception of measurements for pRIIα and pRIIβ (black lines, ***Figure 1***E & F) where 60 s reactions containing 100 nM CN were used.

For pNPP hydrolysis assays, para-nitrophenol (pNP) production was monitored continuously by measuring absorbance at 405 nm in a FLUOstar Omega microplate reader. Each 50 μL assay contained 5 μL of 10 x pNPP reaction buffer (100 mM Tris, pH 8.0, 100 mM NaCl, 10 mM CaCl2, 1 mg/ml of BSA, 60 mM MgCl2, 10 mM DTT), and 35 μL solution containing proteins at the appropriate concentrations in pNPP dilution buffer (100 mM Tris pH 8.0, 100 mM NaCl). Assays were performed with 200 nM CN,

and 5 μM CaM where appropriate. Reactions were initiated by addition of 10 μL pNPP (Merck) to a final concentration of 5 mM, and pNP production was monitored at 22 °C for 1 hour at 1-minute intervals. For assays using phosphopeptide substrate, 19-mer pRII was synthesised by Biomatik at > 95 % purity. Each 50 μL assay contained 5 μL of 10 x phosphopeptide reaction buffer (25 mM Na HEPES pH 7.5, 150 mM NaCl, 25 mM MgCl2, 5 mM DTT, 0.5 mg/mL BSA, 1 mM EDTA), and 30 μL solution containing proteins at the appropriate concentrations in phosphopeptide dilution buffer (25 mM Na HEPES pH 7.5, 150 mM NaCl). Assays were performed with 100 nM CN, and 3 μM CaM where appropriate. Assays were initiated by addition of pRII phosphopeptide to a final concentration of 40 μM, and terminated by addition of 50 μL Biomol Green solution (Enzo Life Sciences) following 3 min incubation at 22 °C. Free phosphate concentration was determined by measuring absorbance at 624 nm in the FLUOstar Omega microplate reader.

Quantitative immunoblotting of CA1 neuropil extracts. Hippocampal slices were prepared from 18-day old male Sprague-Dawley rats. Rats were euthanized by cervical dislocation and 350 μm-thick hippocampal slices were collected using a Leica VT1200S microtome in ice-cold sucrose-based saline (189 mM sucrose, 10 mM glucose, 3 mM KCl, 5 mM $MgSO_4$, 26 mM $NaHCO_3$, 1.25 mM NaH_2PO_4, 0.1 mM $CaCl_2$, pH 7.4) saturated with 95% O_2/5% CO_2. Slices were next transferred to a storage chamber filled with artificial cerebrospinal fluid (aCSF; 124 mM NaCl, 3 mM KCl, 24 mM $NaHCO_3$, 1.25 mM NaH_2PO_4, 1 mM $MgSO_4$, 10 mM glucose, 2 mM $CaCl_2$, pH 7.4) saturated with 95% O_2/5% CO_2 first for one hour at ~ 31 ˚C and at room temperature thereafter. For micro-dissection, slices were transferred onto a pre-chilled Sylgard-coated 90-mm petri dish atop a dry ice/ethanol bath. The CA1 neuropil layer was micro-dissected using an angled micro-knife (Cajigas et al., 2012) by first cutting along the borders of the stratum pyramidale/stratum radiatum and the stratum lacunosum moleculare/hippocampal fissure. Subsequent lateral cuts at the CA2-CA1 and subiculum-CA1 borders completed the rectangular micro-slices. Micro-dissected neuropil slices were immediately snap frozen in liquid nitrogen and stored at -80 °C. To extract protein, neuropil slices (~ 15 per animal) were first pulverized with a micro-pestle then resuspended in a final volume of 300 μL extraction buffer (50 mM Tris-HCl, 50 mM NaF, 10 mM EGTA, 10 mM EDTA, 0.08 mM sodium molybdate, 5 mM sodium pyrophosphate, 1 mM penylmethylsulfonyl fluoride, 0.5 % mM Igepal CA-630, 0.25% mM sodium deoxycholate, 4 mM para-nitrophenylphosphate, cOmplete EDTA-free protease inhibitors and PhosStop phosphatase inhibitors (Roche) at 1 tablet each per 50 mL). The homogenate was sonicated briefly (30 s at 20 MHz) then clarified by centrifugation at 21,130 x *g* (15 min at 4 °C). Total protein concentration in each extract was determined by BCA assay. Quantitative immunoblotting was performed as described previously (Walker-Gray et al., 2017) using anti-PKA subunit primary antibodies purchased from BD Biosciences. HRP-conjugated secondary

antibodies were detected with WesternBright ECL chemiluminescent HRP substrate using a ImageQuant imaging unit (GE Healthcare). Band intensities for reference protein standards and neuropil extracts were calculated in ImageJ. For each immunoblot, a reference curve was generated by fitting reference protein concentrations and band intensities to a Hill function (with typical R^2 coefficients > 0.99) using iterative least squares refinement with the Levenberg-Marquardt algorithm in Origin (OriginLab). PKA subunit concentrations in neuropil extracts were determined by cross-referencing to reference curves derived from the same immunoblot.

AKAR4 measurements. AKAR4 fluorescence measurements were performed using black-walled 96-well plates in a FLUOstar Omega microplate reader (BMG Labtech) equipped with a 430nm excitation filter, and 485nm/520nm emission filters. Each 50 µL reaction contained 35 µL proteins mixed in dilution buffer (20 mM HEPES pH 7.5 and 100 mM NaCl) including AKAR4 reporter (0.2 µM final concentration in all cases) and 5 µL of 10 x reaction buffer (20 mM Na HEPES pH 7.5, 100 mM NaCl, 10 mM DTT, 100 mM $MgCl_2$, 10 mM $CaCl_2$, 0.5 % Igepal CA-630). After three baseline measurements, PKA phosphorylation was initiated by addition of 10 µL solution containing ATP and the desired concentration of cAMP using two injectors built into the plate reader. One injector was primed with ATP solution (20 mM Na HEPES pH 7.5, 100 mM NaCl, 25 mM ATP) and the other with ATP/cAMP solution (20 mM Na HEPES pH 7.5, 100 mM NaCl, 25 mM ATP, 2.5 or 10 µM cAMP) so that different proportions of the two injectors could be used to vary the final cAMP concentration. Measurements were collected at 5 second intervals for a minimum of 10 minutes at 22 ºC following injection of ATP. For every run, one control well was included in which AKAR4 was omitted from the protein mixture to enable baseline subtraction.

Phosphorylated AKAR4 (pAKAR4), for use in assays comparing PP1 and CN activity towards the reporter, was prepared by incubating 400 µg purified AKAR4 with 20 µg PKA C subunit in 1 mL AKAR4 phosphorylation buffer (25 mM Na Hepes pH 7.5, 150 mM NaCl, 10 mM $MgCl_2$, 5 mM ATP, 2 mM DTT). Following 30 min incubation at 30 °C, the phosphorylated reporter was exchanged into 25 mM Na Hepes pH 7.5 and 100 mM NaCl using Sephadex G-25 medium. In pAKAR4 dephosphorylation assays, each well contained 35 µL phosphatase at the appropriate concentration in dilution buffer mixed with 5 µL of 10 x reaction buffer. Reactions were initiated by injection of 10 µL AKAR4 solution to a final concentration of 0.2 µM, and measurements were collected at 5 s intervals for 15 minutes thereafter. For all AKAR4 assays, run parameters were set using Reader Control Software for FLUOstar Omega, and measurements were analyzed using MARS Data Analysis Software (BMG Labtech). Aliquots of a single AKAR4 purification were used across all experiments.

Kinetic modeling. The model scheme of PKA activation is an updated and extended version of the one published by Buxbaum and Dudai (Buxbaum & Dudai, 1989). The model was simulated in a single reaction compartment devoid of any geometry as a system of chemical reactions mimicking the experimental conditions listed above. The individual chemical reactions were modeled as ordinary differential equation (ODE) using the chemical mass-action equation, as:

$$A + B \underset{k_r}{\overset{k_f}{\Leftrightarrow}} AB$$

$$-\frac{d[A]}{dt} = -\frac{d[B]}{dt} = \frac{d[AB]}{dt} = k_f\,(x) = k_f[A][B] = k_r[AB]$$

In total, there were 16 chemical species and 16 reactions included in the model, incorporating mostly bi-molecular reactions with forward and backward reaction rates. Enzymatic reactions were represented by the three elementary steps of binding, dissociation and catalysis. All model variants were built using the MATLAB Simbiology toolbox (MathWorks). All reactions, along with initial concentrations of all chemical species and kinetic rates, are listed in ***Supplementary File 1***.

PKA activation follows a sequential binding of four cAMP molecules to the PKA regulatory RII subunit holoenzyme followed by the release (or activation) of two active catalytic subunits (Taylor et al., 2019). However, the chosen modeling approach involved some simplifications: (1) The two RII subunits within the holoenzyme were assumed to behave independently – whereas in reality, some cooperativity is observed in PKA activation due to intra-dimeric contacts within the PKA holoenzymes (Taylor et al., 2012); (2) The two cAMP binding sites on the RII subunit were modelled as a single binding event such that binding of cAMP to RII/pRII is first order with respect to cAMP (Hao et al., 2019). This simplification was incorporated as our focus here was on understanding transitions between pRII and RII subunits and not the precise mechanism of cAMP activation; (3) The respective dephosphorylation parameters for both pRII and pRII bound to cAMP were assumed to be equal; (4) Rates of RII phosphorylation by bound C subunit were assumed to be equal irrespective of whether cAMP was bound to the regulatory subunit; (5) RIIα and RIIβ were assumed to behave similarly since isoform-specific differences were not the focus here. These simplifications were used to reduce the number of model parameters.

Parameters corresponding to the reactions involving dephosphorylation by CN were modified to represent the situations ‘with’ and ‘without’ AKAP79 (***Supplementary File 1***). In total eighteen different experimental AKAR4 responses were used to estimate the model parameters. Twelve corresponded to

data shown in ***Figure 3***C & E collected with either 0, 0.2, 1 or 2 μM cAMP activation: conditions with PKA (II) + CaM either alone, with CN, or with both CN and AKAP79. The other six correspond to the calibration curves of C subunit interaction with AKAR4 (***Figure 3-figure supplement* 1**A), which were used to estimate AKAR4 parameters that were kept frozen when the other model parameters were estimated. All parameters were estimated using an approximate Bayesian computation (ABC) approach, which included copulas for merging of different experimental data sets (Eriksson et al., 2019). A Bayesian approach was used over optimization for a single parameter set, to account for the uncertainty in parameter space, and that more than one set of parameters could fit the data. The result is thus described using distributions for possible parameter values, rather than single values. Initial prior knowledge about the possible parameter values using data from this study, and previously published work from other groups (Buxbaum & Dudai, 1989; Isensee et al., 2018; Moore et al., 2003), was used to initiate the parameter fitting (details in ***Supplementary File 1***). To account for parameter uncertainty, a log uniform prior distribution for the ABC-method was used. Many of the parameters were set to have a 'prior' range which varied three orders of magnitude from a default parameter value (black bar in ***Figure 5-figure supplement 1***A), which ensured that our parameter values adopted in previous studies (Buxbaum & Dudai, 1989) were sampled. Simulations were started with initial conditions mimicking the experimental settings, thus for the WT system the initial conditions were assumed to reflect that all RII were either free or bound to C with no phosphorylated species or interactions with cAMP. Simulations were then run for the same length as time as the experiments, assuming the cAMP was added at t=0 and that autophosphorylation started at that time.

For predicting responses with mutant RIIα subunits, the base model was extended by splitting the RII into two pools, namely RIIα (85%) and RIIβ (15%) but keeping the parameter distribution received from the parameter estimation when only one isoform of RII was accounted for. Experiments with WT RII subunits were successfully re-simulated with the extended model to validate the approach. As the mutations when simulating both S98A and S98E were in the RIIα subtype (85%), the corresponding parameters depicting the mutation were only varied for this pool. Both the mutant forms, S98A and S98E, were tested as different model variants. To mimic the conditions of the S98A mutation in the model, the phosphorylation rates of RIIα and RIIα bound with cAMP were set to zero (i.e. for the RIIα partition of the model, kinetics were restricted to the right-hand square sub-system shown in ***Figure 4***D). Here the initial conditions were estimated in the same way as described above. To mimic the S98E mutation in the model, the turnover number for dephosphorylation of pRIIα and pRIIα with cAMP by CN were set to zero (i.e. for the RIIα partition of the model, kinetics were restricted to the left-hand square in ***Figure 4***D). Since S98E mimics a case where all the RII subunits are phosphorylated, in this case initial conditions were such that all RIIα were distributed between pRIIα and pRIIα-C.

All model variants were built using the MATLAB Simbiology toolbox (MathWorks). Simulations of these reaction systems were performed using the ode15s solver. All simulations were run for 605 s and the AKAR4 phosphorylation was extracted as output to compare with the experimental findings. The model equations were also exported to the statistical programming language R (https://www.r-project.org/) for implementing the parameter estimation through the ABC-copula approach (Eriksson et al., 2019) and only accept parameter sets whose simulated phosphorylated AKAR4 curves reproduced the experimental measurements. A slight modification to the distance measure ρ was introduced to include timeseries data, where $\rho = \sum_i (y_i^{exp} - y_i^{sim})^2 / n$ where y are experimental and simulated data points (normalized to be within 0 and 1) and n the number of data points for the experiment (for details see the code repository). The sampling resulted in approximately 15,000 parameter samples (a subset of which are shown in ***Figure 5-figure supplement 1***A) which all fitted the experimental data within a threshold set to $\rho < 0.01$. All parameter set samples, describing the uncertainty in the parameter estimates, were next projected onto the situations with mutant RIIα subunits. The model immediately reproduced the experimental observations with RIIα S98E subunits. Although the model correctly reproduced lower rates of AKAR4 that occur with RIIα S98A subunits, and that suppression of PKA activity by AKAP79/CN is reduced in this case, there was a substantial spread in the simulated responses in this case. This indicated that WT data had not perfectly constrained the dynamics in the unphosphorylated RII sub-system (right-hand square, ***Figure 4***B). Therefore, to better understand which parameter characteristics that were important to also account for the RIIα S98A, the parameter sets were sub-classified based on how well they fit data collected with RIIα S98A subunits and no CN (light red, ***Figure 5***C) using a threshold of 0.0. The parameter sets and its effect on different chemical species of the model were described by multi-trajectory, pairwise coordinate and boxplots, where the color schemes follow the classification described above. A code repository for this study may be accessed at https://github.com/jdgas/AKAP79_PKA. It contains the R code for the ABC method as well as MATLAB code for reproducing figures. The R code has to be run on a computer cluster. The repository also contains the models with a few example parameter sets, the full parameter sample as described above, and supplementary figures with simulations and experimental data for all 0, 0.2, 1 and 2 μM cAMP levels with either WT S98A, or S98E RIIα in the reaction mix.

Lentivirus construction. Lentiviruses were generated by inserting RIIα-IRES2-GFP expression cassettes into a pFUGW-H1 lentiviral vector (Addgene cat no. 25870) containing a shRNA sequence targeting for rat RIIα. In the first step, coding sequence for rat PKA RIIα was isolated from a cDNA library that we generated from total hippocampal RNA from a 7-day old male Sprague Dawley rat bred in the UCL

colony. RNA was extracted using an RNeasy Mini Kit before the cDNA library was generated using the first-strand cDNA synthesis kit. Coding sequence for RIIα was amplified from the library using primers Prkar2a_F & Prkar2a_R and inserted upstream of the IRES2 sequence in pIRES2-GFP (Clontech) using EcoRI and BamHI entry sites. Three pFUGW-H1-shRIIα vectors were constructed to determine an optimal targeting sequence for knockdown of rat RIIα. The targeting sequences (primer pairs shRIIα_F1/R1, shRIIα_F2/R2, and shRIIα_F3/R3) were inserted using the XbaI site of pFUGW-H1. The efficiency of each targeting sequence was determined by co-transfecting HEK293T cells with pIRES2-RIIα-EGFP and each pFUGW-H1 vector, with the pFUGW vector in a 10-fold excess. Anti-RIIα immunoblotting revealed that sequence shRIIα-1, which targets bases 134-154 in the rat RIIα coding sequence, was particularly effective at knocking down RIIα protein levels (***Figure 6***B) so this variant served as the parent pFUGW-H1-shRIIα vector in the subsequent steps. The coding sequence for RIIα in pIRES2-RIIα-GFP was rendered shRNA-resistant ('RIIα*') by SDM with primers Prkar2a_shRNA_resist_F & R. After introducing an NheI entry site into pFUGW-H1-shRIIα by SDM using primers FUGW_NheI_F & R, the dual expression cassette for RIIα-IRES2-GFP was transferred across into pFUGW-H1-shRIIα downstream of the ubiquitin promoter using NheI and AgeI sites to create the complete lentiviral vector pFUGW-H1-shRIIα-RIIα*-IRES2-EGFP.

Vectors containing RIIα replacement sequences with mutations at S97 were obtained by SDM with primers pairs rS97A_F & R and rS97E_F & R. In addition, a control vector containing a scrambled shRNA sequence was constructed using primers shScram_F & R. To produce lentivirus, pFUGW vectors were co-transfected with pCMVdR8.74 packaging vector (Addgene cat no. 12259) and pMD2.G envelope glycoprotein vector (Addgene cat no. 12259) into HEK293 cells using Lipofectamine 2000 and maintained in DMEM supplemented with 10% FBS. Cell culture media was collected at both 48 and 72 hours after transfection, subjected to 0.45 µm filtering, and centrifuged at 48,384 x *g* for 4 hours at 4°C to concentrate viral particles. Pelleted virus was resuspended in sterile PBS and stored at – 80 °C. Lentiviruses were validated by transducing dissociated hippocampal cultures on DIV7. Neurons were collected on DIV14, and protein extracted using sonication (3 x 10 s at 20 MHz) in extraction buffer. The homogenate was clarified by centrifugation at 21,130 x g for 15 minutes before analysis of protein levels in the supernatant by immunoblotting using antibodies including anti-PKA pRIIα (Abcam, RRID: AB_779040), anti-GFP (Sigma Aldrich, RRID: AB_2750576), and anti-β-tubulin antibodies (Biolegend, RRID: AB_2565030).

Lentiviral infection and imaging of dissociated primary hippocampal neurons. Primary hippocampal cultures were cultured from E18 Sprague-Dawley pups. Hippocampi were isolated and triturated with

trypsin (0.025%) before plating on poly-L-lysine-coated coverslips or 6-well plates in DMEM containing 10% heat-inactivated horse serum, and penicillin (40 U/mL)/streptomycin (40 µg/mL). Neurons were cultured at 37°C in 95% air/5% CO_2. Two hours after seeding, the plating media was replaced with Neurobasal-A supplemented with 1% B27, 0.5% (v/v) GlutaMAX, 20 mM glucose, and penicillin (100 U/mL)/streptomycin (100 µg/mL). Culture media and additives were purchased from Gibco with the exception of GlutaMAX (Thermo Fisher Scientific). Neurons were infected with lentivirus at DIV7 or DIV9 for dendritic spine density and time-lapse experiments, respectively. Concentrated viral stocks were diluted in conditioned media and incubated with neurons for 18 hours before replacing with fresh pre-conditioned media. Live-cell confocal imaging of dendritic spines was performed using an upright Zeiss LSM 510 confocal microscope equipped with an Achroplan 40x water differential interference contrast objective (numerical aperture 0.8). Transduced neurons were washed four times in HEPES-buffered Krebs solution (140 mM NaCl, 4.2 mM KCl, 1.2 mM $MgCl_2$, 2.52 mM $CaCl_2$, 5 mM Na HEPES, and 11 mM glucose, adjusted to pH 7.4 with NaOH) and placed into a chamber in this same solution at room temperature. For each dendritic segment, upper and lower bounds in the z-plane were initially determined using a rapid z-scan. A full image stack was then collected using a 488 nm Argon laser and a 505-530 nm band-pass emission filter for imaging EGFP fluorescence using 512 x 512 frames with 3-line averaging, and optical slice spacing of 1.035 µm. Time-lapse experiments were conducted to measure changes in spine density and spine-head size after the induction of chemical LTD. An optical slice spacing of 0.9 µm was used during time-lapse experiments. Z-stacks were acquired every 5 min from 15 min before to 60 min after the induction of chemical LTD. Bath application of 20 µM NMDA for 3 min was used to induce NMDAR-dependent LTD (Lee et al., 1998). Data was deconvolved using ImageJ (NIH) before automated dendrite identification and classification in NeuronStudio (Rodriguez et al., 2008). In time-lapse experiments, dendritic spine densities were normalized to the value at t=0.

Statistical analysis. All data are presented as means ± SE. Kinetic rates were statistically compared using two-tailed unpaired Student *t*-tests. Spine imaging data was compared by ANOVA with Turkey post-hoc tests (***Figure 6***D) and Bonferroni's post-hoc test (***Figure 6***G). $*p < 0.05$; $**p < 0.01$; $***p < 0.001$.

Acknowledgements

We thank Denis Yuan for assistance with protein purification, and Alexandra Jauhiainen, Andrei Kramer and Federica Milinanni for help with the parameter estimation process. MGG is a Wellcome Trust and Royal Society Sir Henry Dale fellow (104194/Z/14/A), and is grateful for support from the BBSRC (BB/N015274/1). SH is a Rett Syndrome Fellow and also supported by a Wellcome Trust Collaborative

762 award to TGS. The research was supported by the Swedish Research Council (VR-M-2017-02806; VR-
763 M-2020-01652), the Swedish e-Science Research Centre (SeRC), European Union/Horizon 2020 no.
764 945539 Human Brain Project SGA3, and an Erasmus Scholarship from Portugal. Optimizations and
765 simulations were performed on resources provided by the Swedish National Infrastructure for Computing
766 (SNIC) at Lunarc, Lund University.
767

References

Aye, T. T., Scholten, A., Taouatas, N., Varro, A., Van Veen, T. A., Vos, M. A., & Heck, A. J. (2010, Oct). Proteome-wide protein concentrations in the human heart. *Mol Biosyst, 6*(10), 1917-1927. https://doi.org/10.1039/c004495d

Baillie, G. S., Tejeda, G. S., & Kelly, M. P. (2019, Oct). Therapeutic targeting of 3',5'-cyclic nucleotide phosphodiesterases: inhibition and beyond. *Nat Rev Drug Discov, 18*(10), 770-796. https://doi.org/10.1038/s41573-019-0033-4

Baldwin, T. A., & Dessauer, C. W. (2018, Jan 16). Function of Adenylyl Cyclase in Heart: the AKAP Connection. *J Cardiovasc Dev Dis, 5*(1). https://doi.org/10.3390/jcdd5010002

Bear, M. F. (2003, Apr 29). Bidirectional synaptic plasticity: from theory to reality. *Philos Trans R Soc Lond B Biol Sci, 358*(1432), 649-655. https://doi.org/10.1098/rstb.2002.1255

Bers, D. M., Xiang, Y. K., & Zaccolo, M. (2019, Jul 1). Whole-Cell cAMP and PKA Activity are Epiphenomena, Nanodomain Signaling Matters. *Physiology (Bethesda), 34*(4), 240-249. https://doi.org/10.1152/physiol.00002.2019

Blumenthal, D. K., Takio, K., Hansen, R. S., & Krebs, E. G. (1986, Jun 25). Dephosphorylation of cAMP-dependent protein kinase regulatory subunit (type II) by calmodulin-dependent protein phosphatase. Determinants of substrate specificity. *J Biol Chem, 261*(18), 8140-8145. https://www.ncbi.nlm.nih.gov/pubmed/3013843

Bock, A., Annibale, P., Konrad, C., Hannawacker, A., Anton, S. E., Maiellaro, I., Zabel, U., Sivaramakrishnan, S., Falcke, M., & Lohse, M. J. (2020, Sep 17). Optical Mapping of cAMP Signaling at the Nanometer Scale. *Cell, 182*(6), 1519-1530 e1517. https://doi.org/10.1016/j.cell.2020.07.035

Buxbaum, J. D., & Dudai, Y. (1989, Jun 5). A quantitative model for the kinetics of cAMP-dependent protein kinase (type II) activity. Long-term activation of the kinase and its possible relevance to learning and memory. *J Biol Chem, 264*(16), 9344-9351. https://www.ncbi.nlm.nih.gov/pubmed/2722837

Cajigas, I. J., Tushev, G., Will, T. J., tom Dieck, S., Fuerst, N., & Schuman, E. M. (2012, May 10). The local transcriptome in the synaptic neuropil revealed by deep sequencing and high-resolution imaging. *Neuron, 74*(3), 453-466. https://doi.org/10.1016/j.neuron.2012.02.036

Clouet, D. H., & Gaitonde, M. K. (1956, Dec). The changes with age in the protein composition of the rat brain. *J Neurochem, 1*(2), 126-133. https://doi.org/10.1111/j.1471-4159.1956.tb12063.x

Coghlan, V. M., Perrino, B. A., Howard, M., Langeberg, L. K., Hicks, J. B., Gallatin, W. M., & Scott, J. D. (1995, Jan 6). Association of protein kinase A and protein phosphatase 2B with a common anchoring protein. *Science, 267*(5194), 108-111. http://www.ncbi.nlm.nih.gov/entrez/query.fcgi?cmd=Retrieve&db=PubMed&dopt=Citation&list_uids=7528941

Dacher, M., Gouty, S., Dash, S., Cox, B. M., & Nugent, F. S. (2013, Feb 6). A-kinase anchoring protein-calcineurin signaling in long-term depression of GABAergic synapses. *J Neurosci, 33*(6), 2650-2660. https://doi.org/10.1523/JNEUROSCI.2037-12.2013

Delint-Ramirez, I., Willoughby, D., Hammond, G. R., Ayling, L. J., & Cooper, D. M. (2011, Sep 23). Palmitoylation targets AKAP79 protein to lipid rafts and promotes its regulation of calcium-sensitive adenylyl cyclase type 8. *J Biol Chem, 286*(38), 32962-32975. https://doi.org/10.1074/jbc.M111.243899

Dell'Acqua, M. L., Dodge, K. L., Tavalin, S. J., & Scott, J. D. (2002, Dec 13). Mapping the protein phosphatase-2B anchoring site on AKAP79. Binding and inhibition of phosphatase activity are mediated by residues 315-360. *J Biol Chem, 277*(50), 48796-48802. https://doi.org/10.1074/jbc.M207833200

Dell'Acqua, M. L., Faux, M. C., Thorburn, J., Thorburn, A., & Scott, J. D. (1998, Apr 15). Membrane-targeting sequences on AKAP79 bind phosphatidylinositol-4, 5-bisphosphate. *Embo J, 17*(8), 2246-2260. http://www.ncbi.nlm.nih.gov/entrez/query.fcgi?cmd=Retrieve&db=PubMed&dopt=Citation&list_uids=9545238

Depry, C., Allen, M. D., & Zhang, J. (2011, Jan). Visualization of PKA activity in plasma membrane microdomains [Research Support, N.I.H., Extramural]. *Mol Biosyst, 7*(1), 52-58. https://doi.org/10.1039/c0mb00079e

Dittmer, P. J., Dell'Acqua, M. L., & Sather, W. A. (2014, Jun 12). Ca2+/calcineurin-dependent inactivation of neuronal L-type Ca2+ channels requires priming by AKAP-anchored protein kinase A. *Cell Rep, 7*(5), 1410-1416. https://doi.org/10.1016/j.celrep.2014.04.039

Eriksson, O., Jauhiainen, A., Maad Sasane, S., Kramer, A., Nair, A. G., Sartorius, C., & Hellgren Kotaleski, J. (2019, Jan 15). Uncertainty quantification, propagation and characterization by Bayesian analysis combined with global sensitivity analysis applied to dynamical intracellular pathway models. *Bioinformatics, 35*(2), 284-292. https://doi.org/10.1093/bioinformatics/bty607

Gildart, M., Kapiloff, M. S., & Dodge-Kafka, K. L. (2020, Jul). Calcineurin-AKAP interactions: therapeutic targeting of a pleiotropic enzyme with a little help from its friends. *J Physiol*, *598*(14), 3029-3042. https://doi.org/10.1113/JP276756

Gold, M. G. (2019, Oct 31). Swimming regulations for protein kinase A catalytic subunit. *Biochem Soc Trans*, *47*(5), 1355-1366. https://doi.org/10.1042/BST20190230

Gold, M. G., Lygren, B., Dokurno, P., Hoshi, N., McConnachie, G., Tasken, K., Carlson, C. R., Scott, J. D., & Barford, D. (2006, Nov 3). Molecular basis of AKAP specificity for PKA regulatory subunits. *Molecular cell*, *24*(3), 383-395. https://doi.org/10.1016/j.molcel.2006.09.006

Gold, M. G., Stengel, F., Nygren, P. J., Weisbrod, C. R., Bruce, J. E., Robinson, C. V., Barford, D., & Scott, J. D. (2011, Apr 19). Architecture and dynamics of an A-kinase anchoring protein 79 (AKAP79) signaling complex. *Proc Natl Acad Sci U S A*, *108*(16), 6426-6431. https://doi.org/10.1073/pnas.1014400108

Grigoriu, S., Bond, R., Cossio, P., Chen, J. A., Ly, N., Hummer, G., Page, R., Cyert, M. S., & Peti, W. (2013). The molecular mechanism of substrate engagement and immunosuppressant inhibition of calcineurin. *PLoS biology*, *11*(2), e1001492. https://doi.org/10.1371/journal.pbio.1001492

Hinke, S. A., Navedo, M. F., Ulman, A., Whiting, J. L., Nygren, P. J., Tian, G., Jimenez-Caliani, A. J., Langeberg, L. K., Cirulli, V., Tengholm, A., Dell'Acqua, M. L., Santana, L. F., & Scott, J. D. (2012, Oct 17). Anchored phosphatases modulate glucose homeostasis. *Embo J*, *31*(20), 3991-4004. https://doi.org/10.1038/emboj.2012.244

Hogan, P. G. (2017, May). Calcium-NFAT transcriptional signalling in T cell activation and T cell exhaustion. *Cell Calcium*, *63*, 66-69. https://doi.org/10.1016/j.ceca.2017.01.014

Hoshi, N., Langeberg, L. K., Gould, C. M., Newton, A. C., & Scott, J. D. (2010, Feb 26). Interaction with AKAP79 modifies the cellular pharmacology of PKC. *Molecular cell*, *37*(4), 541-550. https://doi.org/10.1016/j.molcel.2010.01.014

Houslay, M. D., & Baillie, G. S. (2005, Dec). Beta-arrestin-recruited phosphodiesterase-4 desensitizes the AKAP79/PKA-mediated switching of beta2-adrenoceptor signalling to activation of ERK. *Biochem Soc Trans*, *33*(Pt 6), 1333-1336. https://doi.org/10.1042/BST20051333

Huang, Y. Y., Li, X. C., & Kandel, E. R. (1994, Oct 7). cAMP contributes to mossy fiber LTP by initiating both a covalently mediated early phase and macromolecular synthesis-dependent late phase. *Cell*, *79*(1), 69-79. https://doi.org/10.1016/0092-8674(94)90401-4

Ilouz, R., Lev-Ram, V., Bushong, E. A., Stiles, T. L., Friedmann-Morvinski, D., Douglas, C., Goldberg, G., Ellisman, M. H., & Taylor, S. S. (2017, Jan 12). Isoform-specific subcellular localization and function of protein kinase A identified by mosaic imaging of mouse brain. *Elife*, *6*. https://doi.org/10.7554/eLife.17681

Isensee, J., Kaufholz, M., Knape, M. J., Hasenauer, J., Hammerich, H., Gonczarowska-Jorge, H., Zahedi, R. P., Schwede, F., Herberg, F. W., & Hucho, T. (2018, Jun 4). PKA-RII subunit phosphorylation precedes activation by cAMP and regulates activity termination. *J Cell Biol*, *217*(6), 2167-2184. https://doi.org/10.1083/jcb.201708053

Jurado, S., Biou, V., & Malenka, R. C. (2010, Sep). A calcineurin/AKAP complex is required for NMDA receptor-dependent long-term depression. *Nat Neurosci*, *13*(9), 1053-1055. https://doi.org/nn.2613 [pii]
10.1038/nn.2613

Kar, P., Samanta, K., Kramer, H., Morris, O., Bakowski, D., & Parekh, A. B. (2014, Jun 16). Dynamic assembly of a membrane signaling complex enables selective activation of NFAT by Orai1. *Curr Biol*, *24*(12), 1361-1368. https://doi.org/10.1016/j.cub.2014.04.046

Kashishian, A., Howard, M., Loh, C., Gallatin, W. M., Hoekstra, M. F., & Lai, Y. (1998, Oct 16). AKAP79 inhibits calcineurin through a site distinct from the immunophilin-binding region. *J Biol Chem*, *273*(42), 27412-27419. https://doi.org/10.1074/jbc.273.42.27412

Keith, D. J., Sanderson, J. L., Gibson, E. S., Woolfrey, K. M., Robertson, H. R., Olszewski, K., Kang, R., El-Husseini, A., & Dell'acqua, M. L. (2012, May 23). Palmitoylation of A-kinase anchoring protein 79/150 regulates dendritic endosomal targeting and synaptic plasticity mechanisms. *J Neurosci*, *32*(21), 7119-7136. https://doi.org/10.1523/JNEUROSCI.0784-12.2012

Kelker, M. S., Page, R., & Peti, W. (2009, Jan 9). Crystal structures of protein phosphatase-1 bound to nodularin-R and tautomycin: a novel scaffold for structure-based drug design of serine/threonine phosphatase inhibitors. *J Mol Biol*, *385*(1), 11-21. https://doi.org/10.1016/j.jmb.2008.10.053

Kinderman, F. S., Kim, C., von Daake, S., Ma, Y., Pham, B. Q., Spraggon, G., Xuong, N. H., Jennings, P. A., & Taylor, S. S. (2006, Nov 3). A dynamic mechanism for AKAP binding to RII isoforms of cAMP-dependent protein kinase. *Molecular cell*, *24*(3), 397-408. https://doi.org/10.1016/j.molcel.2006.09.015

Knape, M. J., Ahuja, L. G., Bertinetti, D., Burghardt, N. C., Zimmermann, B., Taylor, S. S., & Herberg, F. W. (2015, Oct 16). Divalent Metal Ions Mg(2)(+) and Ca(2)(+) Have Distinct Effects on Protein Kinase A Activity and Regulation. *ACS Chem Biol*, *10*(10), 2303-2315. https://doi.org/10.1021/acschembio.5b00271

Kwon, H. B., & Sabatini, B. L. (2011, Jun 2). Glutamate induces de novo growth of functional spines in developing cortex. *Nature*, *474*(7349), 100-104. https://doi.org/10.1038/nature09986

Lee, H. K., Kameyama, K., Huganir, R. L., & Bear, M. F. (1998, Nov). NMDA induces long-term synaptic depression and dephosphorylation of the GluR1 subunit of AMPA receptors in hippocampus. *Neuron*, *21*(5), 1151-1162. https://doi.org/10.1016/s0896-6273(00)80632-7

Li, H., Pink, M. D., Murphy, J. G., Stein, A., Dell'Acqua, M. L., & Hogan, P. G. (2012, Feb 19). Balanced interactions of calcineurin with AKAP79 regulate Ca2+-calcineurin-NFAT signaling. *Nat Struct Mol Biol*, *19*(3), 337-345. https://doi.org/10.1038/nsmb.2238

Lu, Y., Zha, X. M., Kim, E. Y., Schachtele, S., Dailey, M. E., Hall, D. D., Strack, S., Green, S. H., Hoffman, D. A., & Hell, J. W. (2011, Jul 29). A kinase anchor protein 150 (AKAP150)-associated protein kinase A limits dendritic spine density. *J Biol Chem*, *286*(30), 26496-26506. https://doi.org/10.1074/jbc.M111.254912

Lu, Y., Zhang, M., Lim, I. A., Hall, D. D., Allen, M., Medvedeva, Y., McKnight, G. S., Usachev, Y. M., & Hell, J. W. (2008, Sep 1). AKAP150-anchored PKA activity is important for LTD during its induction phase. *J Physiol*, *586*(17), 4155-4164. https://doi.org/10.1113/jphysiol.2008.151662

Mo, G. C., Ross, B., Hertel, F., Manna, P., Yang, X., Greenwald, E., Booth, C., Plummer, A. M., Tenner, B., Chen, Z., Wang, Y., Kennedy, E. J., Cole, P. A., Fleming, K. G., Palmer, A., Jimenez, R., Xiao, J., Dedecker, P., & Zhang, J. (2017, Apr). Genetically encoded biosensors for visualizing live-cell biochemical activity at super-resolution. *Nat Methods*, *14*(4), 427-434. https://doi.org/10.1038/nmeth.4221

Moore, M. J., Adams, J. A., & Taylor, S. S. (2003, Mar 21). Structural basis for peptide binding in protein kinase A. Role of glutamic acid 203 and tyrosine 204 in the peptide-positioning loop. *J Biol Chem*, *278*(12), 10613-10618. https://doi.org/10.1074/jbc.M210807200

Mulkey, R. M., Endo, S., Shenolikar, S., & Malenka, R. C. (1994, Jun 9). Involvement of a calcineurin/inhibitor-1 phosphatase cascade in hippocampal long-term depression. *Nature*, *369*(6480), 486-488. https://doi.org/10.1038/369486a0

Murphy, J. G., Sanderson, J. L., Gorski, J. A., Scott, J. D., Catterall, W. A., Sather, W. A., & Dell'Acqua, M. L. (2014, Jun 12). AKAP-anchored PKA maintains neuronal L-type calcium channel activity and NFAT transcriptional signaling. *Cell Rep*, *7*(5), 1577-1588. https://doi.org/10.1016/j.celrep.2014.04.027

Ni, Q., Ganesan, A., Aye-Han, N. N., Gao, X., Allen, M. D., Levchenko, A., & Zhang, J. (2011, Jan). Signaling diversity of PKA achieved via a Ca2+-cAMP-PKA oscillatory circuit. *Nat Chem Biol*, *7*(1), 34-40. https://doi.org/10.1038/nchembio.478

Nygren, P. J., Mehta, S., Schweppe, D. K., Langeberg, L. K., Whiting, J. L., Weisbrod, C. R., Bruce, J. E., Zhang, J., Veesler, D., & Scott, J. D. (2017, Oct 2). Intrinsic disorder within AKAP79 fine-tunes anchored phosphatase activity toward substrates and drug sensitivity. *Elife, 6*. https://doi.org/10.7554/eLife.30872

Ogreid, D., & Doskeland, S. O. (1981, Jul 6). The kinetics of the interaction between cyclic AMP and the regulatory moiety of protein kinase II. Evidence for interaction between the binding sites for cyclic AMP. *FEBS Lett, 129*(2), 282-286. https://www.ncbi.nlm.nih.gov/pubmed/6269881

Patel, N., Stengel, F., Aebersold, R., & Gold, M. G. (2017, Nov 22). Molecular basis of AKAP79 regulation by calmodulin. *Nat Commun, 8*(1), 1681. https://doi.org/10.1038/s41467-017-01715-w

Perrino, B. A., Fong, Y. L., Brickey, D. A., Saitoh, Y., Ushio, Y., Fukunaga, K., Miyamoto, E., & Soderling, T. R. (1992, Aug 5). Characterization of the phosphatase activity of a baculovirus-expressed calcineurin A isoform. *J Biol Chem, 267*(22), 15965-15969. https://www.ncbi.nlm.nih.gov/pubmed/1322410

Qi, C., Sorrentino, S., Medalia, O., & Korkhov, V. M. (2019, Apr 26). The structure of a membrane adenylyl cyclase bound to an activated stimulatory G protein. *Science, 364*(6438), 389-394. https://doi.org/10.1126/science.aav0778

Qian, H., Patriarchi, T., Price, J. L., Matt, L., Lee, B., Nieves-Cintron, M., Buonarati, O. R., Chowdhury, D., Nanou, E., Nystoriak, M. A., Catterall, W. A., Poomvanicha, M., Hofmann, F., Navedo, M. F., & Hell, J. W. (2017, Jan 24). Phosphorylation of Ser1928 mediates the enhanced activity of the L-type Ca2+ channel Cav1.2 by the beta2-adrenergic receptor in neurons. *Sci Signal, 10*(463). https://doi.org/10.1126/scisignal.aaf9659

Rangel-Aldao, R., & Rosen, O. M. (1976, Jun 10). Dissociation and reassociation of the phosphorylated and nonphosphorylated forms of adenosine 3':5' -monophosphate-dependent protein kinase from bovine cardiac muscle. *J Biol Chem, 251*(11), 3375-3380. https://www.ncbi.nlm.nih.gov/pubmed/179996

Redden, J. M., & Dodge-Kafka, K. L. (2011, Oct). AKAP phosphatase complexes in the heart. *J Cardiovasc Pharmacol, 58*(4), 354-362. https://doi.org/10.1097/FJC.0b013e31821e5649

Roach, P. J., Depaoli-Roach, A. A., Hurley, T. D., & Tagliabracci, V. S. (2012, Feb 1). Glycogen and its metabolism: some new developments and old themes. *Biochem J, 441*(3), 763-787. https://doi.org/10.1042/BJ20111416

Rodriguez, A., Ehlenberger, D. B., Dickstein, D. L., Hof, P. R., & Wearne, S. L. (2008, Apr 23). Automated three-dimensional detection and shape classification of dendritic spines from fluorescence microscopy images. *PLoS One, 3*(4), e1997. https://doi.org/10.1371/journal.pone.0001997

Roy, J., & Cyert, M. S. (2009, Dec 8). Cracking the phosphatase code: docking interactions determine substrate specificity. *Sci Signal, 2*(100), re9. https://doi.org/10.1126/scisignal.2100re9

Sanderson, J. L., Gorski, J. A., & Dell'Acqua, M. L. (2016, Mar 2). NMDA Receptor-Dependent LTD Requires Transient Synaptic Incorporation of Ca(2)(+)-Permeable AMPARs Mediated by AKAP150-Anchored PKA and Calcineurin. *Neuron, 89*(5), 1000-1015. https://doi.org/10.1016/j.neuron.2016.01.043

Sanderson, J. L., Gorski, J. A., Gibson, E. S., Lam, P., Freund, R. K., Chick, W. S., & Dell'Acqua, M. L. (2012, Oct 24). AKAP150-anchored calcineurin regulates synaptic plasticity by limiting synaptic incorporation of Ca2+-permeable AMPA receptors. *J Neurosci, 32*(43), 15036-15052. https://doi.org/10.1523/JNEUROSCI.3326-12.2012

Schmitt, J. P., Kamisago, M., Asahi, M., Li, G. H., Ahmad, F., Mende, U., Kranias, E. G., MacLennan, D. H., Seidman, J. G., & Seidman, C. E. (2003, Feb 28). Dilated cardiomyopathy and heart failure caused by a mutation in phospholamban. *Science, 299*(5611), 1410-1413. https://doi.org/10.1126/science.1081578

Smith, F. D., Esseltine, J. L., Nygren, P. J., Veesler, D., Byrne, D. P., Vonderach, M., Strashnov, I., Eyers, C. E., Eyers, P. A., Langeberg, L. K., & Scott, J. D. (2017, Jun 23). Local protein kinase A action proceeds through intact holoenzymes. *Science, 356*(6344), 1288-1293. https://doi.org/10.1126/science.aaj1669

Stemmer, P. M., & Klee, C. B. (1994, Jun 7). Dual calcium ion regulation of calcineurin by calmodulin and calcineurin B. *Biochemistry, 33*(22), 6859-6866. https://doi.org/10.1021/bi00188a015

Taylor, S. S., Meharena, H. S., & Kornev, A. P. (2019, Jun). Evolution of a dynamic molecular switch. *IUBMB Life, 71*(6), 672-684. https://doi.org/10.1002/iub.2059

Tillo, S. E., Xiong, W. H., Takahashi, M., Miao, S., Andrade, A. L., Fortin, D. A., Yang, G., Qin, M., Smoody, B. F., Stork, P. J. S., & Zhong, H. (2017, Apr 18). Liberated PKA Catalytic Subunits Associate with the Membrane via Myristoylation to Preferentially Phosphorylate Membrane Substrates. *Cell Rep, 19*(3), 617-629. https://doi.org/10.1016/j.celrep.2017.03.070

Tulsian, N. K., Krishnamurthy, S., & Anand, G. S. (2017, Jun 20). Channeling of cAMP in PDE-PKA Complexes Promotes Signal Adaptation. *Biophys J, 112*(12), 2552-2566. https://doi.org/10.1016/j.bpj.2017.04.045

Tunquist, B. J., Hoshi, N., Guire, E. S., Zhang, F., Mullendorff, K., Langeberg, L. K., Raber, J., & Scott, J. D. (2008, Aug 26). Loss of AKAP150 perturbs distinct neuronal processes in mice. *Proc Natl Acad Sci U S A, 105*(34), 12557-12562. https://doi.org/0805922105 [pii] 10.1073/pnas.0805922105

Walker-Gray, R., Stengel, F., & Gold, M. G. (2017, Sep 26). Mechanisms for restraining cAMP-dependent protein kinase revealed by subunit quantitation and cross-linking approaches. *Proc Natl Acad Sci U S A, 114*(39), 10414-10419. https://doi.org/10.1073/pnas.1701782114

Weisenhaus, M., Allen, M. L., Yang, L., Lu, Y., Nichols, C. B., Su, T., Hell, J. W., & McKnight, G. S. (2010, Apr 23). Mutations in AKAP5 disrupt dendritic signaling complexes and lead to electrophysiological and behavioral phenotypes in mice. *PLoS One, 5*(4), e10325. https://doi.org/10.1371/journal.pone.0010325

Wild, A. R., Sinnen, B. L., Dittmer, P. J., Kennedy, M. J., Sather, W. A., & Dell'Acqua, M. L. (2019, Mar 26). Synapse-to-Nucleus Communication through NFAT Is Mediated by L-type Ca(2+) Channel Ca(2+) Spike Propagation to the Soma. *Cell Rep, 26*(13), 3537-3550 e3534. https://doi.org/10.1016/j.celrep.2019.03.005

Woolfrey, K. M., O'Leary, H., Goodell, D. J., Robertson, H. R., Horne, E. A., Coultrap, S. J., Dell'Acqua, M. L., & Bayer, K. U. (2018, Feb 2). CaMKII regulates the depalmitoylation and synaptic removal of the scaffold protein AKAP79/150 to mediate structural long-term depression. *J Biol Chem, 293*(5), 1551-1567. https://doi.org/10.1074/jbc.M117.813808

Xiong, W. H., Qin, M., & Zhong, H. (2021, Apr 13). Myristoylation alone is sufficient for PKA catalytic subunits to associate with the plasma membrane to regulate neuronal functions. *Proc Natl Acad Sci U S A, 118*(15). https://doi.org/10.1073/pnas.2021658118

Zhang, J., & Shapiro, M. S. (2012, Dec 20). Activity-dependent transcriptional regulation of M-Type (Kv7) K(+) channels by AKAP79/150-mediated NFAT actions. *Neuron, 76*(6), 1133-1146. https://doi.org/10.1016/j.neuron.2012.10.019

Zhang, J., & Shapiro, M. S. (2016, Jan 1). Mechanisms and dynamics of AKAP79/150-orchestrated multi-protein signalling complexes in brain and peripheral nerve. *J Physiol, 594*(1), 31-37. https://doi.org/10.1113/jphysiol.2014.287698

Zhang, J. Z., Lu, T. W., Stolerman, L. M., Tenner, B., Yang, J. R., Zhang, J. F., Falcke, M., Rangamani, P., Taylor, S. S., Mehta, S., & Zhang, J. (2020, Sep 17). Phase Separation of a PKA Regulatory Subunit Controls cAMP Compartmentation and Oncogenic Signaling. *Cell, 182*(6), 1531-1544 e1515. https://doi.org/10.1016/j.cell.2020.07.043

Zhang, P., Knape, M. J., Ahuja, L. G., Keshwani, M. M., King, C. C., Sastri, M., Herberg, F. W., & Taylor, S. S. (2015, Jul). Single Turnover Autophosphorylation Cycle of the PKA RIIbeta Holoenzyme. *PLoS biology, 13*(7), e1002192. https://doi.org/10.1371/journal.pbio.1002192

Zhang, P., Smith-Nguyen, E. V., Keshwani, M. M., Deal, M. S., Kornev, A. P., & Taylor, S. S. (2012, Feb 10). Structure and allostery of the PKA RIIbeta tetrameric holoenzyme. *Science, 335*(6069), 712-716. https://doi.org/10.1126/science.1213979

Zhang, X., Li, L., & McNaughton, P. A. (2008, Aug 14). Proinflammatory mediators modulate the heat-activated ion channel TRPV1 via the scaffolding protein AKAP79/150. *Neuron, 59*(3), 450-461. https://doi.org/10.1016/j.neuron.2008.05.015

Zhang, X., Pathak, T., Yoast, R., Emrich, S., Xin, P., Nwokonko, R. M., Johnson, M., Wu, S., Delierneux, C., Gueguinou, M., Hempel, N., Putney, J. W., Jr., Gill, D. L., & Trebak, M. (2019, Apr 29). A calcium/cAMP signaling loop at the ORAI1 mouth drives channel inactivation to shape NFAT induction. *Nat Commun, 10*(1), 1971. https://doi.org/10.1038/s41467-019-09593-0

Zhou, Q., Homma, K. J., & Poo, M. M. (2004, Dec 2). Shrinkage of dendritic spines associated with long-term depression of hippocampal synapses. *Neuron, 44*(5), 749-757. https://doi.org/10.1016/j.neuron.2004.11.011

Figure Legends

Figure 1. Effect of AKAP79 on pRII dephosphorylation by CN. (**A**) Dephosphorylation of the inhibitor sequence (IS, yellow) of RII subunits enables faster PKA C subunit capture. (**B**) AKAP79 contains anchoring sites for CN (red) and PKA RII subunits (blue) in its C-terminal region. Other macromolecular interactions are mediated through elements within its tandem polybasic regions (TPRs, grey). (**C**) CN-catalyzed phosphate release from pRIIα subunits with either no AKAP79, WT AKAP79 (light blue), or AKAP79 lacking the PIAIIIT anchoring motif ('ΔCN'). (**D**) CN-catalyzed phosphate release from pRIIβ subunits with either no AKAP79, WT AKAP79 (dark blue), or AKAP79 ΔCN. (**E**) The relationship between CN activity towards pRIIα subunits and pRIIα concentration with pRIIα subunits included either alone (black circles) or in complex with $AKAP79_{c97}$ (light blue squares). (**F**) The relationship between CN activity towards pRIIβ subunits and pRIIβ concentration with pRIIβ subunits included either alone (black circles) or in complex with $AKAP79_{c97}$ (dark blue squares). For panels E & F, activities at each concentration were measured in triplicate. Statistical comparisons were performed using two-tailed unpaired Student *t*-tests. ***$p<0.001$.

Figure 2. Quantitation of PKA subunits in CA1 neuropil. Images of a P17 rat hippocampal slice before (**A**) and after (**B**) micro-dissection of the CA1 neuropil layer. (**C**) Immunoblots of CA1 neuropil extract for PKA subunits. Extracts were run alongside reference amounts of the relevant purified PKA subunit in each immunoblot (***Figure 2-figure supplement 1***). In each case, 15 μg total protein extract was run alongside the reference series, with the exception of the anti-C immunoblot (10 μg extract). (**D**) Copy numbers of PKA subunits in rat CA1 neuropil normalized to C subunits.

Figure 3. FRET-based PKA activity measurements. (**A**) AKAR4 mechanism: phosphorylation of the sensor by PKA is detected as an increase in FRET between the terminal fluorescent proteins. (**B**) Concentrations of proteins used for *in vitro* AKAR4 assays. Different experiments utilized different mixtures of these proteins but always at these concentrations. (**C**) Representative AKAR4 traces showing change in 520 nm / 485 nm (Y/C) emission ratio over time after injection of different concentrations of cAMP in tandem with 5 mM ATP. All protein mixtures included AKAR4, type II PKA (RIIα, RIIβ, C), and CaM. Experiments were performed with either no further additives (top row, black), with CN added (middle row, blue), or with both CN and $AKAP79_{c97}$ added (bottom row, red). ATP/cAMP injections are indicated by arrows. (**D**) The chart shows peak rates of emission ratio change for the recordings shown in the preceding panel. n values are stated above the columns. (**E**)

For these recordings, type II PKA, CN, and CaM were included in all cases. Phosphorylation was initiated by injection of 5 mM ATP and 1 μM cAMP at t=0. Averaged responses ± standard error (SE) are shown with no further additives (blue), or when either WT (red), ΔCN (purple), or ΔPKA (gold) variants of $AKAP79_{c97}$ were included. **(F**) Peak rates (calculated between 30-90 s) for the responses shown in the preceding panel. Statistical comparisons were performed using two-tailed unpaired Student *t*-tests. ***p<0.001.

Figure 4. Kinetic analysis of PKA-CN-AKAP79 signaling. (**A**-**C**) Estimates of the average proportion of free C subunits between 30-90 s for type II PKA alone (black), with CN (blue), and with both CN and $AKAP79_{c97}$ (red) following activation of the protein mixtures with a range of cAMP concentrations. (**D**) Reaction scheme used for modeling type II PKA regulation by CN. Each species within the scheme is numbered consistent with supporting data in figure in ***Supplementary File 1***. (**E**-**G**) Model simulations for protein mixtures activated with 1 μM cAMP are shown with the experimental data overlaid. Averaged values are shown for experimental data after pooling the data shown in ***Figure 3***. Responses are shown for type II PKA alone (**E**), with CN (**F**), and with both CN and $AKAP79_{c97}$ (**G**). A sample of the corresponding simulated responses are shown in grey. An 'error' threshold of 0.01 was used to accept curves as a good fit.

Figure 5. Characterization of RIIα IS phosphorylation site mutations. (**A**) RIIα subunit topology showing locations of the docking and dimerization domain (D/D, grey), inhibitor sequence (IS, yellow), and tandem cyclic nucleotide binding domains (dark and light blue). S98A (red) and S98E (green) mutations in the IS are highlighted. (**B**-**D**) Comparison of AKAR4 emission ratio changes following 5 mM ATP/1 μM cAMP activation of protein mixtures containing either WT (**B**), S98A (**C**), or S98E (**D**) RIIα. 1.03 μM RIIβ was included in all cases. Measurements were collected either with or without CN in the reaction mixture. Averaged responses (± SE) are shown for WT RIIα with (dark blue) and without CN (light blue), S98A RIIα with (dark red) and without (light red) CN, and RIIα S98E with (dark green) and without (light green) CN. (**E**) The upper bar chart shows peak rates (calculated between 30-90 s) for the responses shown in panels b-d. The effect of including CN in the reaction mixture for each RII variant is shown in the lower bar chart. (**F**-**H**) Model predictions in the six conditions of panels b-d are shown in grey when simulating using the 'extended' model (see Methods) and using the different parameter sets generated from the parameter estimation approach. The same parameters as retrieved using data shown in figure 4 were used as a starting point for the simulations, but parameter sets were filtered based on data collected with RIIα S98A. Model

predictions are shown alongside the corresponding experimental data collected with either WT (**F**), S98A (**G**), or S98E (**H**) RII*α* in the reaction mix.

Figure 6. Lentivirus development and spine density imaging. (**A**) Schematic of the FUGW-H1-based lentiviral vector used to knock down and replace endogenous RIIα subunits in dissociated hippocampal cultures. (**B**) To validate lentiviruses, dissociated hippocampal neurons were infected on the seventh day *in vitro* (DIV7). Immunoblots are shown comparing neuronal extracts collected on DIV14 after infection with no virus, virus expressing scrambled shRNA only, shRIIα only, and the three complete lentiviruses for knockdown/replacement with either WT, S97A, or S97E RIIα. (**C**) Representative live-cell images of lentivirus-infected primary hippocampal neurons at DIV14 expressing either WT, S97A, or S97E RIIα. Scale bars correspond to 50 μm (upper panels) and 5 μm (lower panels). **(D**) Average spine density on hippocampal dendrites following lentiviral replacement of endogenous RIIα. Data were averaged from 106 (WT), 97 (S97A), and 113 (S97E) neurons derived from 7 rats for each condition, and are represented as mean ± SE. Conditions were compared using one-way ANOVA with Turkey post-hoc tests. (**E**) Representative live-cell images showing dendritic spines in primary hippocampal neurons expressing either WT, S97A, or S97E replacement RIIα at three points before and after chem-LTD (scale bar = 2.5 μm). Chem-LTD was induced at t=0 with 20 μM NMDA for 3 minutes. The yellow asterisk indicates a spine that disappeared over the course of the protocol whereas the pink asterisks indicate spines that did not. (**F**) Plot showing average changes in spine density (± S.E) in primary hippocampal neurons expressing either WT (dark blue), S97A (red) or S97E (green) RIIα. (**G**) Average changes in spine density ± SE one hour after induction of chem-LTD are shown for neurons expressing WT (dark blue, n=5), S97A (red, n=5), and S97E (green, n=4) RIIα variants as shown in the preceding two panels. Statistical comparisons were performed by 2-way ANOVA followed by Bonferroni's post-hoc test. ** $p<0.01$, *** $P<0.001$

Figure 7. Summary model of PKA suppression by CN within the AKAP79 complex. Structural and kinetic models (upper and lower panels, respectively) of signaling within the AKAP79 complex are shown under conditions of either low (**A**) or elevated Ca^{2+} (**B**). Elevated Ca^{2+} triggers CN (red) dephosphorylation of pRII (blue) which shifts C subunit capture from the left-hand square of the kinetic scheme to the right-hand square which features dephosphorylated forms of RII. The overall effect is a reduction in the concentration of free C subunits. The most abundant forms of RII under the two conditions are highlighted by blue spheres.

Supplementary Figure Legends

Figure 1-figure supplement 1. Purified proteins. Images showing the purity of purified proteins applied in this study are shown following SDS-PAGE with 4–12% Bis-Tris NuPAGE gels. (**A**) Full-length WT PKA RIIα and RIIβ subunits. (**B**) Full-length AKAP79. (**C**) The complex of RIIα and $AKAP79_{c97}$. (**D**) The complex of RIIβ and $AKAP79_{c97}$. (**E**) The CN heterodimer. (**F**) CaM. (**G**) AKAR4 – the left-hand image shows Coomassie staining whereas the right-hand image shows anti-GFP immunoblotting of an equivalent lane after transfer to nitrocellulose. (**H**) Variants of RIIα (WT, S98A, S98E) applied in AKAR4 assays. **(I**) Variants of $AKAP79_{c97}$ (WT, ΔCN, ΔPKA) applied in AKAR4 assays. All images were scanned following Coomassie staining unless otherwise stated.

Figure 1-figure supplement 2. pRII phosphorylation by CN at supra-physiological concentrations. The relationship between CN activity towards pRII and pRII concentration in the absence of AKAP79 is linear for both pRIIα (**A**) and pRIIβ (**B**) up to at least 20 μM pRII.

Figure 1-figure supplement 3. Effect of AKAP79c97 variants on pNPP and pRII phosphopeptide dephosphorylation. (A) Bar chart showing relative rates of pNPP hydrolysis by CN with (blue) and without (black) CaM activation, and for CN+CaM in the presence of WT (red), ΔCN (purple), and ΔPKA (gold) variants of $AKAP79_{c97}$. The relative rate of pNPP hydrolysis was reduced from 1 ± 0.04 to 0.19 ± 0.002 when CaM was excluded. Inclusion of WT $AKAP79_{c97}$ resulted in relative pNPP hydrolysis of 1.61 ± 0.02 (2 μM) and 1.69 ± 0.03 (10 μM); for the ΔCN variant, the rates were 1.00 ± 0.04 (2 μM) and 1.16 ± 0.01 (10 μM); and for the ΔPKA variant, the rates were 1.37 ± 0.02 (2 μM) and 1.44 ± 0.02 (10 μM). Taken together, the data indicate that the PIAIIIT motif of AKAP79 is able to weakly enhance CN hydrolysis of pNPP. (B) Bar chart showing relative rates of 40 μM pRII 19-mer peptide dephosphorylation by CN. Conditions are colored in the same way as the preceding panel. For pRII peptide, the relative rate of dephosphoylation was reduced from 1 ± 0.10 to 0.062 ± 0.01 when CaM was excluded. Inclusion of WT $AKAP79_{c97}$ resulted in relative dephosphorylation rates of 0.51 ± 0.06 (2 μM) and 0.47 ± 0.05 (10 μM); for the ΔCN variant, the rates were 0.92 ± 0.09 (2 μM) and 0.81 ± 0.09 (10 μM); and for the ΔPKA variant, the rates were 0.70 ± 0.07 (2 μM) and 0.66 ± 0.06 (10 μM). The data is consistent with previous reports that AKAP79 weakly inhibits CN activity towards pRII phosphopeptide (Coghlan et al., 1995; Kashishian et al., 1998).

Figure 2-figure supplement 1. Reference curves for quantitation of PKA subunits in CA1 neuropil. The four panels show reference curves (red lines) that relate immunoblot band intensity to ng of PKA subunit per lane, and correspond to the data shown in ***Figure 2***C. (**A**) Anti-pan C immunoblot reference curve. The point at which the neuropil extract lane falls on the curve is denoted by a green circle. (**B**) Anti-pan RI reference curve with neuropil extract lane denoted by a purple circle. (**C**) Anti-RIIα reference curve with neuropil extract lane denoted by a light blue circle. (**D**) Anti-RIIβ reference curve with the neuropil extract lane denoted by a dark blue circle.

Figure 3-figure supplement 1. AKAR4 reference measurements with PKA catalytic subunit. (**A**) Averaged AKAR4 traces showing change in 520 nm / 485 nm (Y/C) emission ratio over time after injection of 5 mM ATP into reactions containing only PKA C subunits at a range of concentrations. (**B**) Relationship between free C subunit concentration (in the absence of CN) and emission ratio change per minute. The data was fitted to a Hill function ($y = 380*x^{1.71}/(3481^{1.71}+x^{1.71})$) with an adjusted R-square value of 0.99983. (**C**) Averaged AKAR4 traces showing data for the same experiment as the preceding panel but with 1.5 μM CN included in all reactions. (**D**) Peak 520 nm / 485 nm (Y/C) emission ratio changes at different concentrations of C subunit, either without (black bars) or with (striped bars) 1.5 μM CN. Average rates were calculated between 15-75 s, with the exception of 0 and 25 nM C subunit concentrations (30 – 330 s). (**E**) Averaged peak AKAR4 responses from all recordings for type II PKA either alone (top row), with CN (middle row), or with both CN and AKAP collected after injections of 5 mM ATP with different concentrations of cAMP. These rates were cross-referenced against the reference curve shown in panel b to estimate free C subunit concentrations (plotted in ***Figure 4***A-C). Peak rates were calculated between 30-90 s, with the exception of 0 & 100 nM cAMP responses where a wider time window (30-330 s) was applied.

Figure 3-figure supplement 2. Comparison of CN and PP1 activity towards AKAR4. (A) AKAR4 responses are shown for reactions containing 400 nM C subunits alone (black), with 1.5 μM CN (blue), or with 1.5 μM PP1 (purple). Phosphorylation was initiated by injection of ATP to a final concentration of 5 mM. (B) Peak rates (calculated between 20-50 s after ATP injection) for the responses shown in the preceding panel. Inclusion of CN did not alter the rate (relative rates of 1 ± 0.05 for C alone compared to 1.02 ± 0.08 for C + CN), whereas addition of PP1 (purple) reduced the rate to 0.14 ± 0.04 (p = 9 x 10e-6). (C) We also compared rates of dephosphorylation of AKAR4 pre-phosphorylated by PKA. Reponses are shown for pAKAR4 dephosphorylation in the presence of no phosphatase (black) or with different concentrations of CN (blue) or PP1 (purple). (D) Peak rates for the data shown in the preceding panel. Replicate numbers for each condition are shown in parentheses. Rates are normalized to the

dephosphorylation rate with 1 μM PP1. The relative rates were as follows: 0.003 ± 0.001 with no phosphatase; with CN, 0.007 ± 0.001 (0.3 μM); 0.011 ± 0.001 (1 CN), and 0.033 ± 0.001 (3 μM); and with PP1, 0.15 ± 0.02 (0.1 μM), 0.44 ± 0.01 (0.3 μM), and 1 ± 0.09 (1 μM). The data indicate that PP1 is much more active towards pAKAR4 than CN, with 5-fold faster pAKAR4 dephosphorylation at the lowest PP1 concentration tested (0.1 μM) than the highest CN concentration (3 μM). The statistical comparison was performed using a one-tailed paired Student t-test. ***p<0.001.

Figure 4-figure supplement 1. Simulations of kinetic scheme species changes in concentration over time. Each row corresponds to the concentration (μM) of an individual species simulated in seven different reaction mixtures. The first three columns correspond to experiments with WT RIIα subunits; columns four and five to experiments with RIIα S98A subunits, and the last two columns with RIIα S98E subunits. Red lines correspond to simulations whose parameter sets were classified as far from experimental data collected with mutated RIIα, but which fit well to data collected with WT RIIα subunits in reactions stimulated with 0, 0.2, 1 and 2 μM cAMP. Blue traces correspond to simulations with parameter sets that generated results close to experimental data collected with both WT and mutant RIIα subunits.

Figure 4-figure supplement 2. Simulations of responses with different concentrations of cAMP. For each condition, simulations (grey lines) are shown alongside experimental data. The first four rows show responses with different concentrations of cAMP: 0 μM (top row), 0.2 μM (second row), 1 μM (third row), 2 μM (fourth row). The bottom row corresponds to responses at 1 μM with mixtures containing RIIα mutants.

Figure 5-figure supplement 1. Space of parameters used in model fitting. (**A**) The illustration shows the marginal posterior distribution of each model parameter on a logarithmic scale for a subset of parameter samples that generated simulations that fit experimental data collected with WT RIIα subunits. Each sample in the distribution is connected across the parameters by a line, whose color indicates whether the corresponding parameter set also generated simulations fitting closely (blue) to data collected with mutant RIIα subunits or not (red). The parameter priors are indicated by the respective black horizontal bars. (**B**) Distribution of dissociation constants (K_D's). The boxplots display median values (red lines), the 50 % datapoint distribution around the median (designated by boxes) and the remaining 25% datapoint distributions (lower and upper whiskers). Boxplots are shown for all eight K_D's obtained with the model priors (left), data fitted using experiments with WT RIIα subunits (middle), and parameters selected for fitting to data collected with RIIα S98A subunits. (**C**)

Marginal histograms for K_D76 (left) and K_D56 (right) with parameter sets classified according to whether they fit well to the RIIα S98A data (blue) or not (red). (**D**) Scatterplot showing how the K_D76 and K_D56 parameters are related according to the same two classes.

Supplementary File Legends

Supplementary File 1. Kinetic modeling parameters. The table lists parameters used in the computational modeling. Parameter terminology is according to the numbers above stated in ***Figure 4***B, e.g., k12 refers to the on rate of cAMP binding to state *1* (pRII-C) to produce state *2* (pRII-C-cAMP). The prior range used to constrain parameter estimation is provided for each parameter along with links to the references used to set the default values.

Supplementary File 2. Oligonucleotide primer sequences.

Legends for source data linked to figures

Figure 1-source data. Radioactive phosphatase assays
Figure 2-source data. Quantitative immunoblotting
Figure 3-source data. Rates of AKAR4 phosphorylation in purified protein mixtures
Figure 4-source data. Free C subunit calculations
Figure 5-source data. Rates of AKAR4 phosphorylation with mutant RIIα subunits
Figure 6-source data. Spine density quantitation
Figure 1-supplement 2. Phosphatase assays without AKAP79
Figure 1-supplement 3. Colorimetric phosphatase assays
Figure 3-supplement 1. Rates of AKAR4 phosphorylation with C subunit alone
Figure 3-supplement 2. Comparison of CN and PP1 activity towards pAKAR4

Legend for source data provided under 'Additional Files'

Source data. Original images of Coomassie-stained gels and immunoblots included in the manuscript

1351

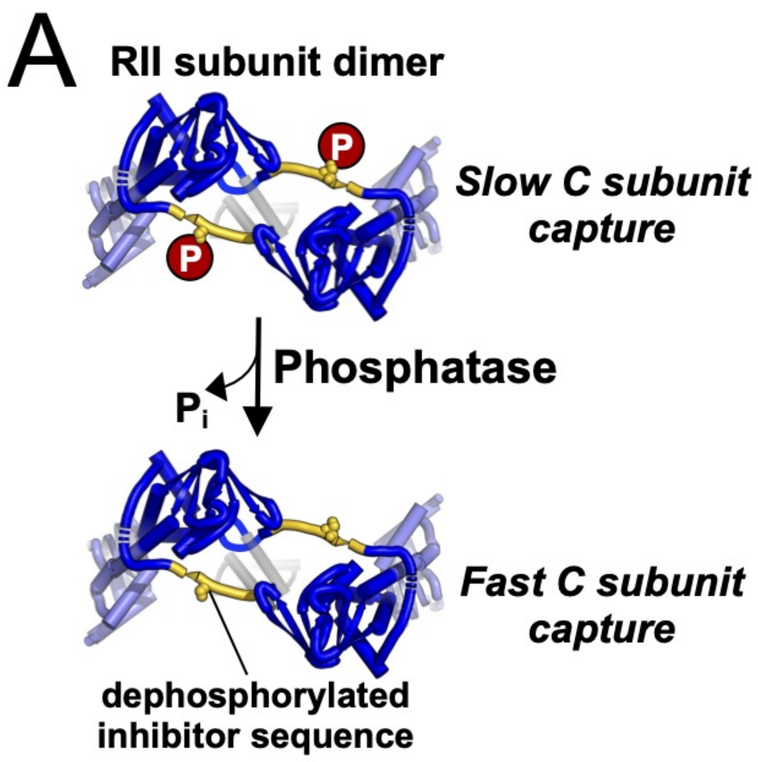
A
RII subunit dimer
P
P
Slow C subunit capture
Phosphatase
Pi
Fast C subunit capture
dephosphorylated inhibitor sequence

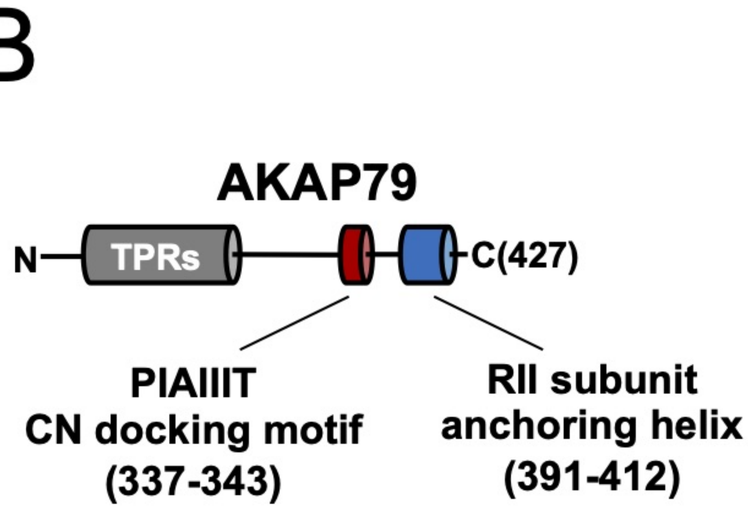
B
AKAP79
N
TPRs
C(427)
PIAIIIT
CN docking motif
(337-343)
RII subunit
anchoring helix
(391-412)

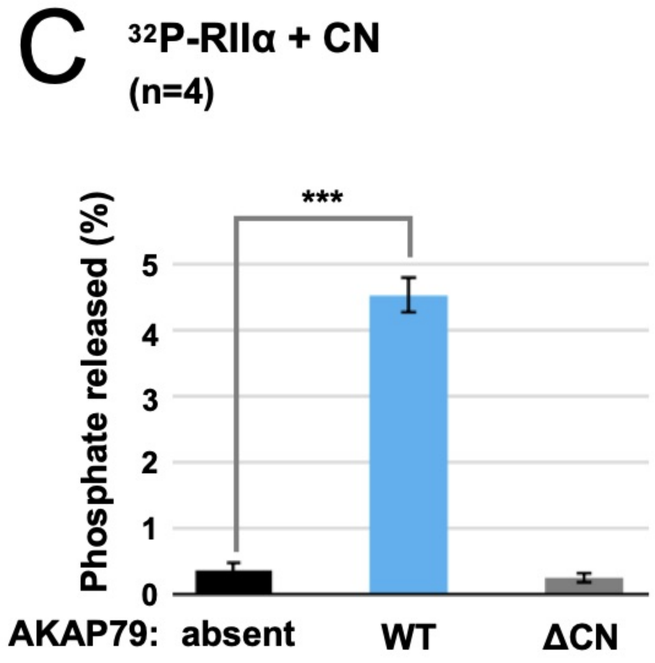
C
32P-RIIα + CN
(n=4)
***
Phosphate released (%)
0
1
2
3
4
5
AKAP79: absent
WT
ΔCN

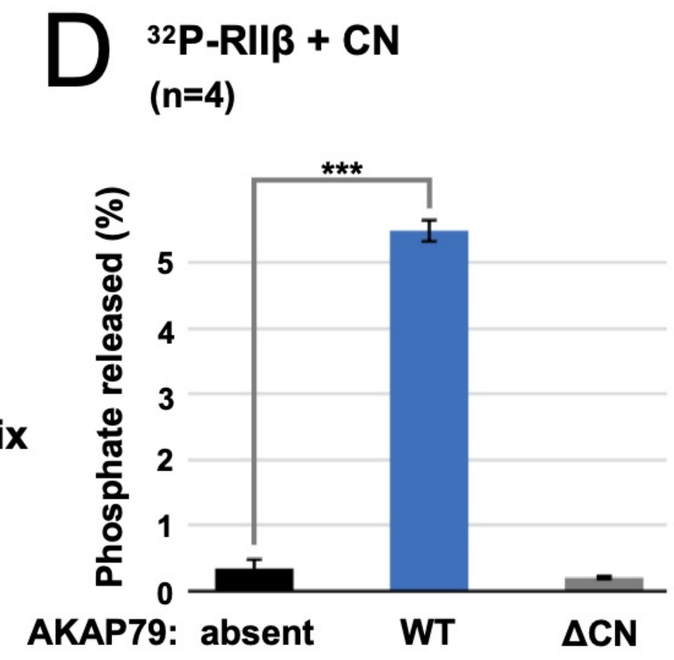
D
32P-RIIβ + CN
(n=4)
***
Phosphate released (%)
0
1
2
3
4
5
AKAP79: absent
WT
ΔCN

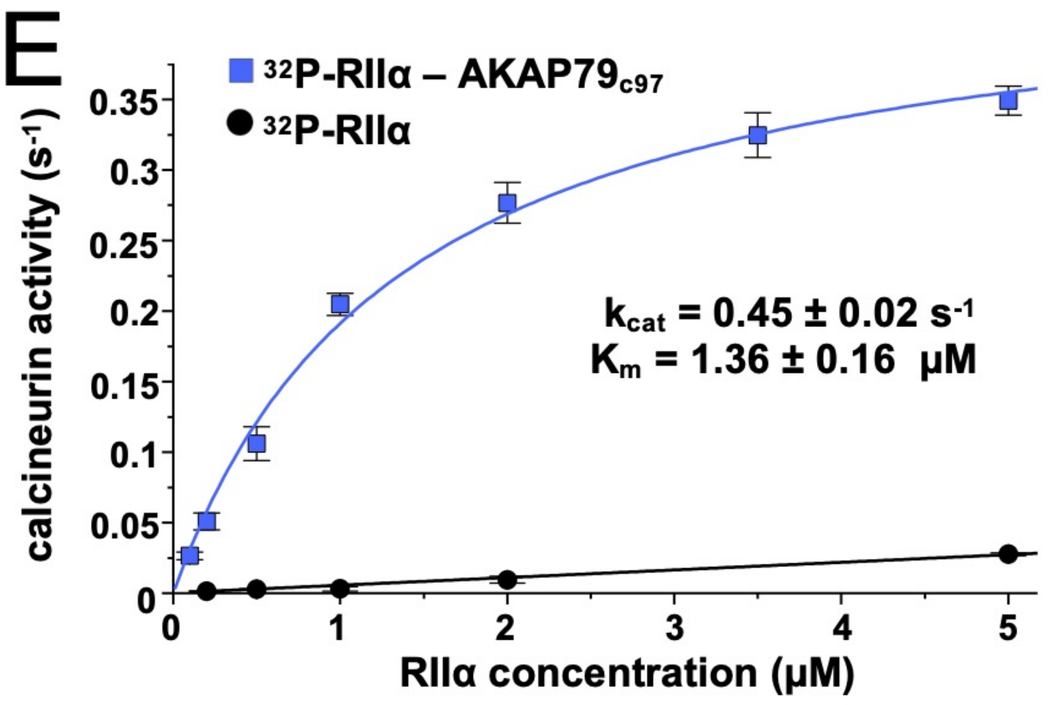
E
32P-RIIα – AKAP79c97
32P-RIIα
kcat = 0.45 ± 0.02 s-1
Km = 1.36 ± 0.16 μM
calcineurin activity (s-1)
0
0.05
0.1
0.15
0.2
0.25
0.3
0.35
0
1
2
3
4
5
RIIα concentration (μM)

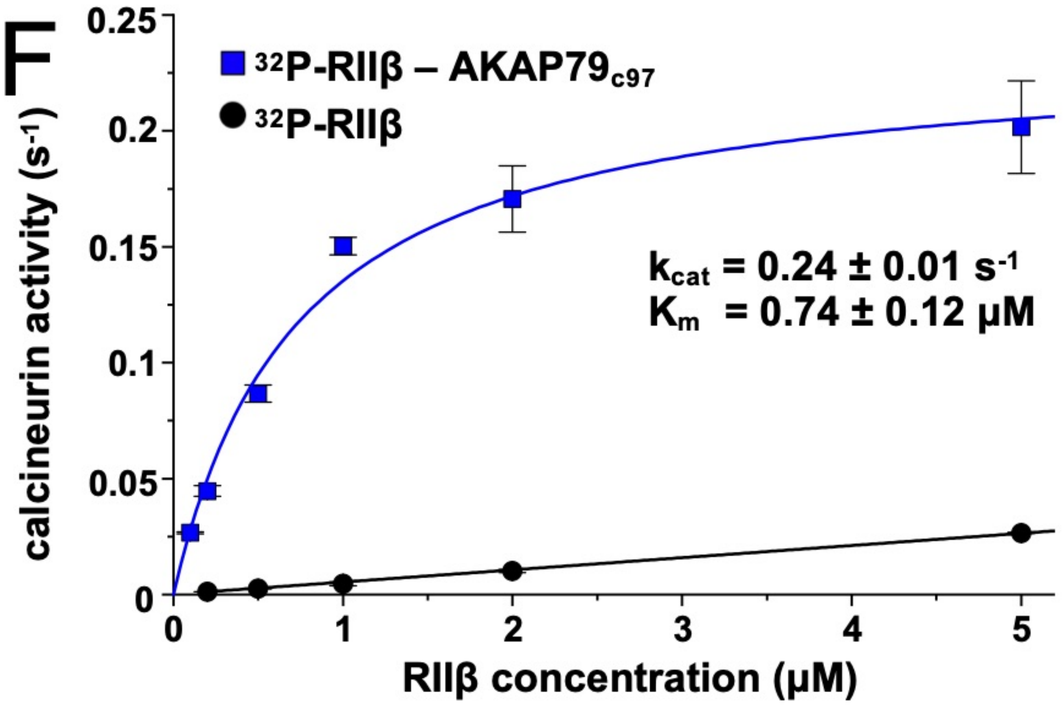
F
32P-RIIβ – AKAP79c97
32P-RIIβ
kcat = 0.24 ± 0.01 s-1
Km = 0.74 ± 0.12 μM
calcineurin activity (s-1)
0
0.05
0.1
0.15
0.2
0.25
0
1
2
3
4
5
RIIβ concentration (μM)

Figure 1

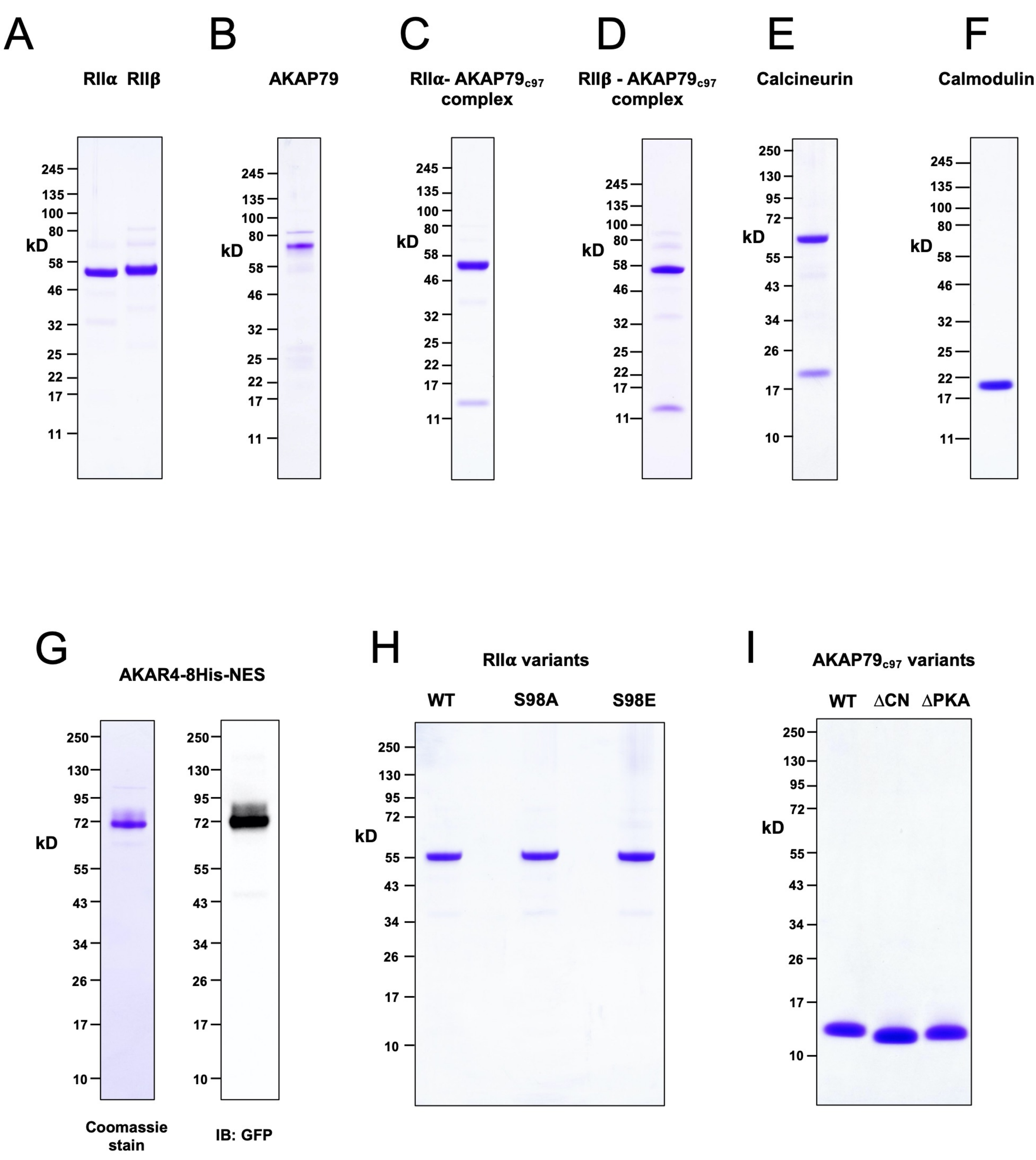

Figure 1 – figure supplement 1

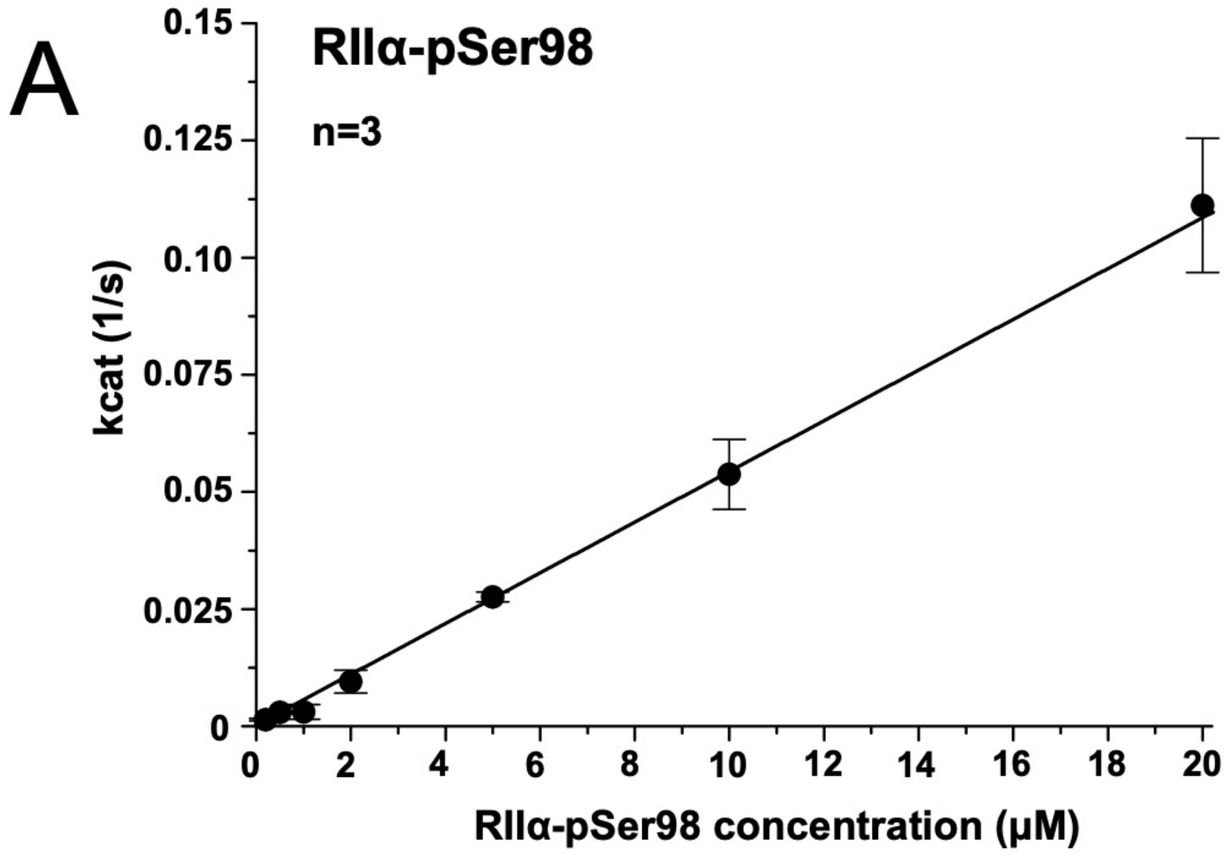

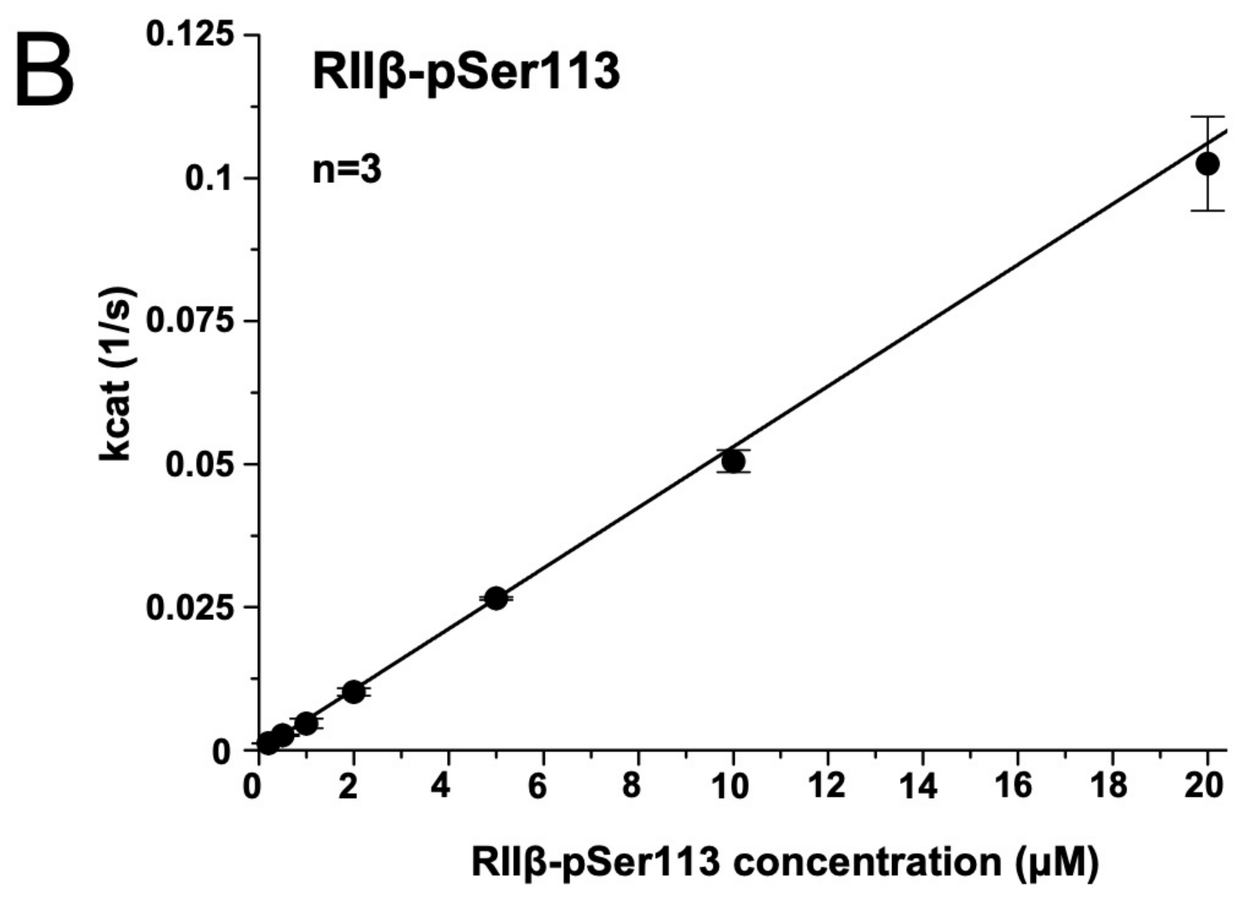

Figure 1 – figure supplement 2

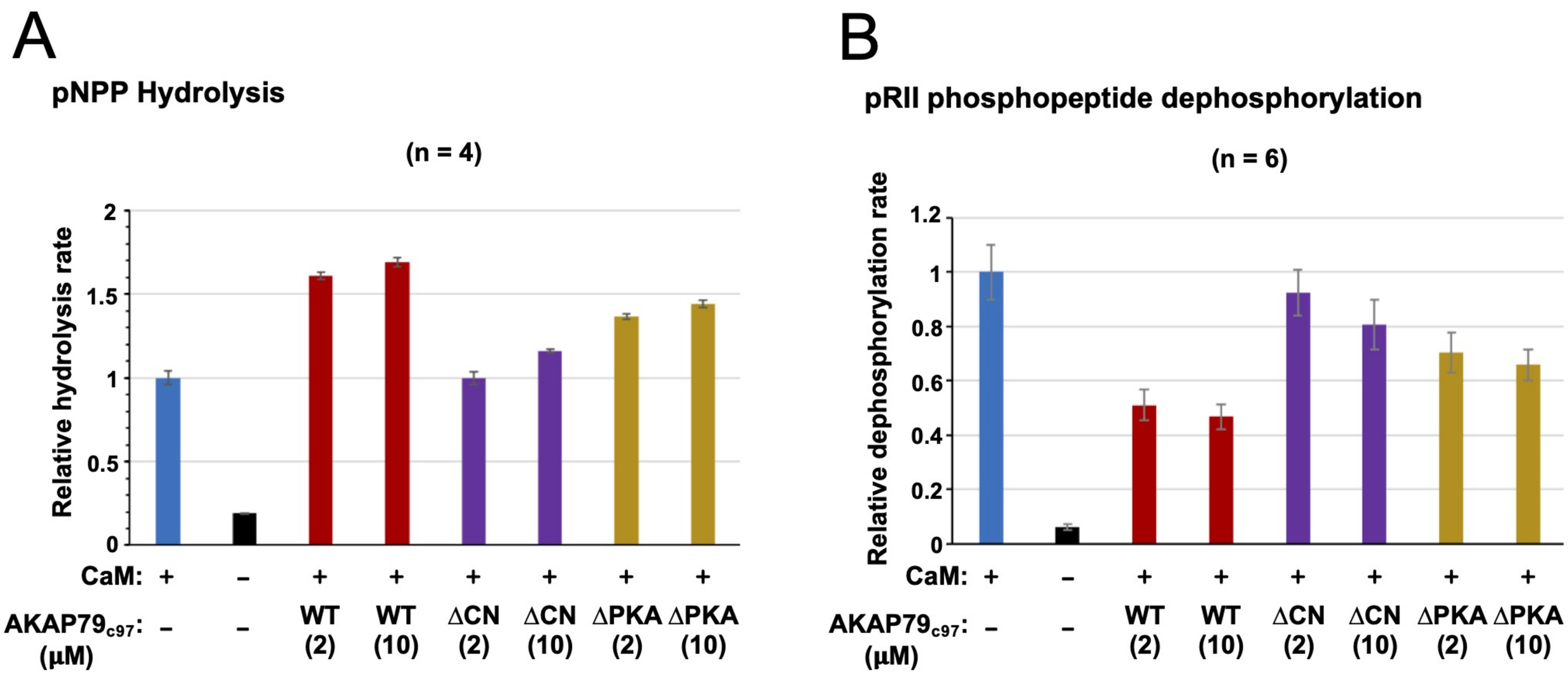

Figure 1-figure supplement 3

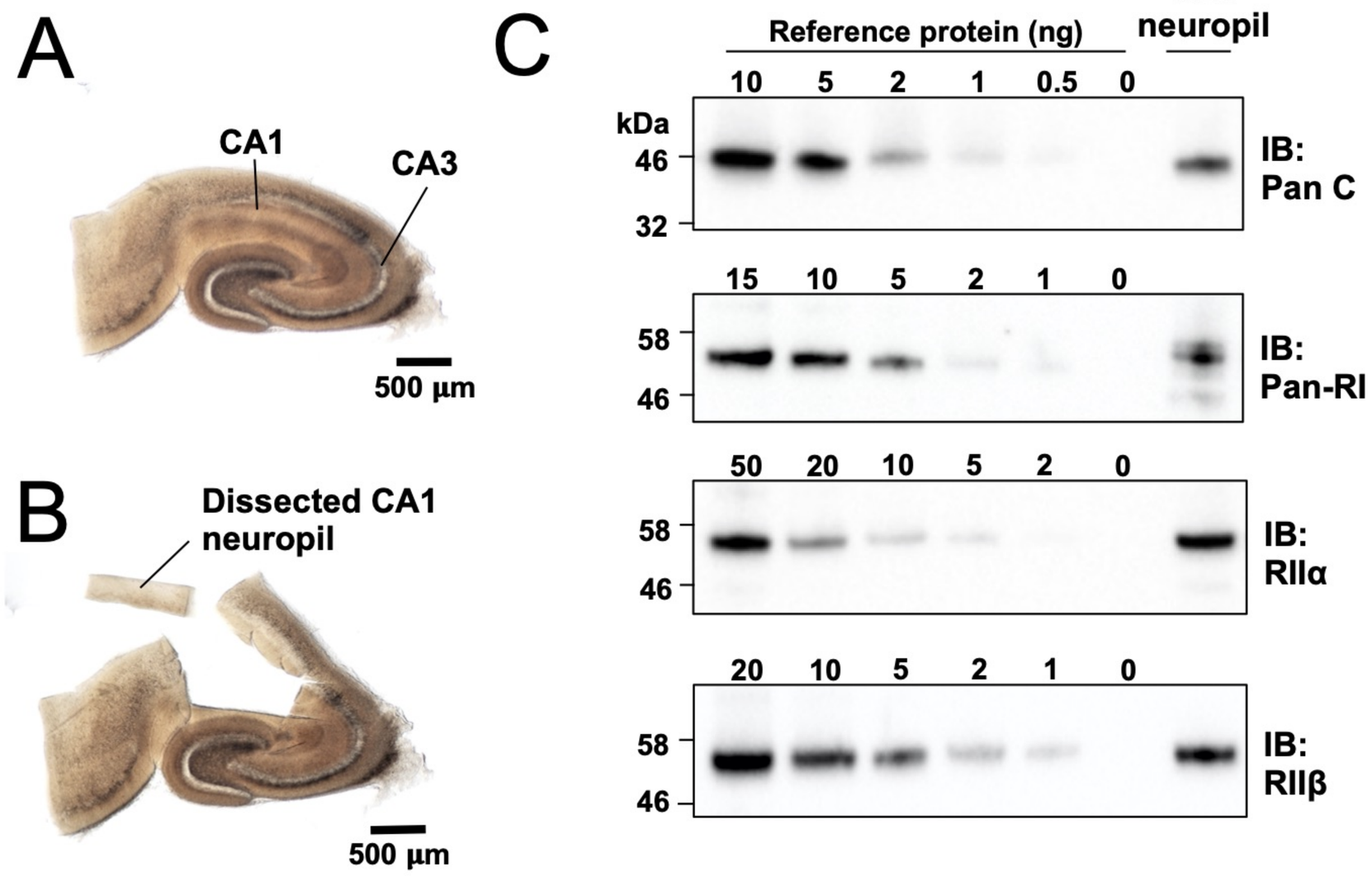
A
CA1
CA3
500 µm
B
Dissected CA1 neuropil
500 µm
C
Reference protein (ng)
CA1 neuropil
10 5 2 1 0.5 0
kDa
46
32
IB: Pan C
15 10 5 2 1 0
58
46
IB: Pan-RI
50 20 10 5 2 0
58
46
IB: RIIα
20 10 5 2 1 0
58
46
IB: RIIβ
D
PKA subunit stoichiometry in CA1 neuropil
(n=5)
Copy number relative to C
10
8
6
4
2
0
9.35
1.19
1.64
C
RI
RIIα
RIIβ

Figure 2

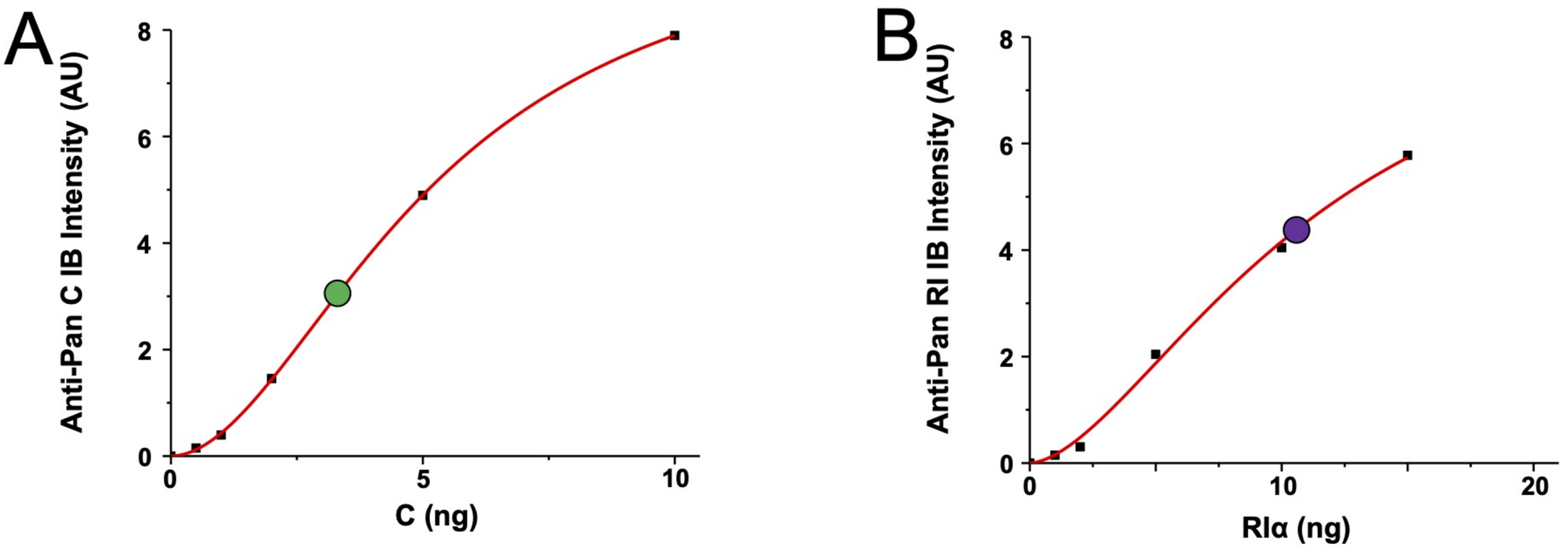

Figure 2 – figure supplement 1

A

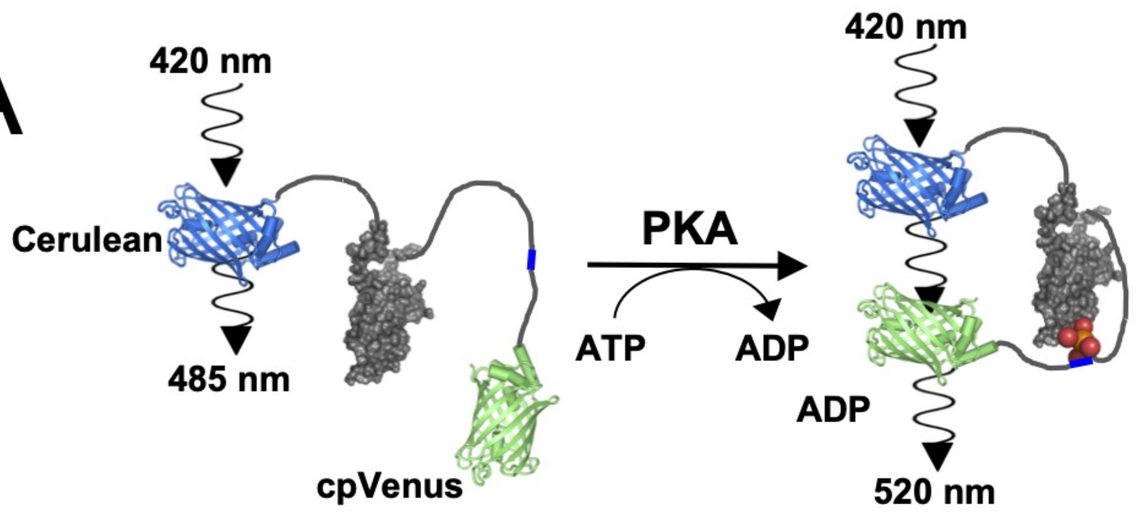

B

Protein	Molarity (μM)
PKA RIIα	5.9
PKA RIIβ	1.03
PKA Cβ	0.63
CN	1.5
CaM	5
AKAP79 c97	3.47
AKAR4 Reporter	0.2

C

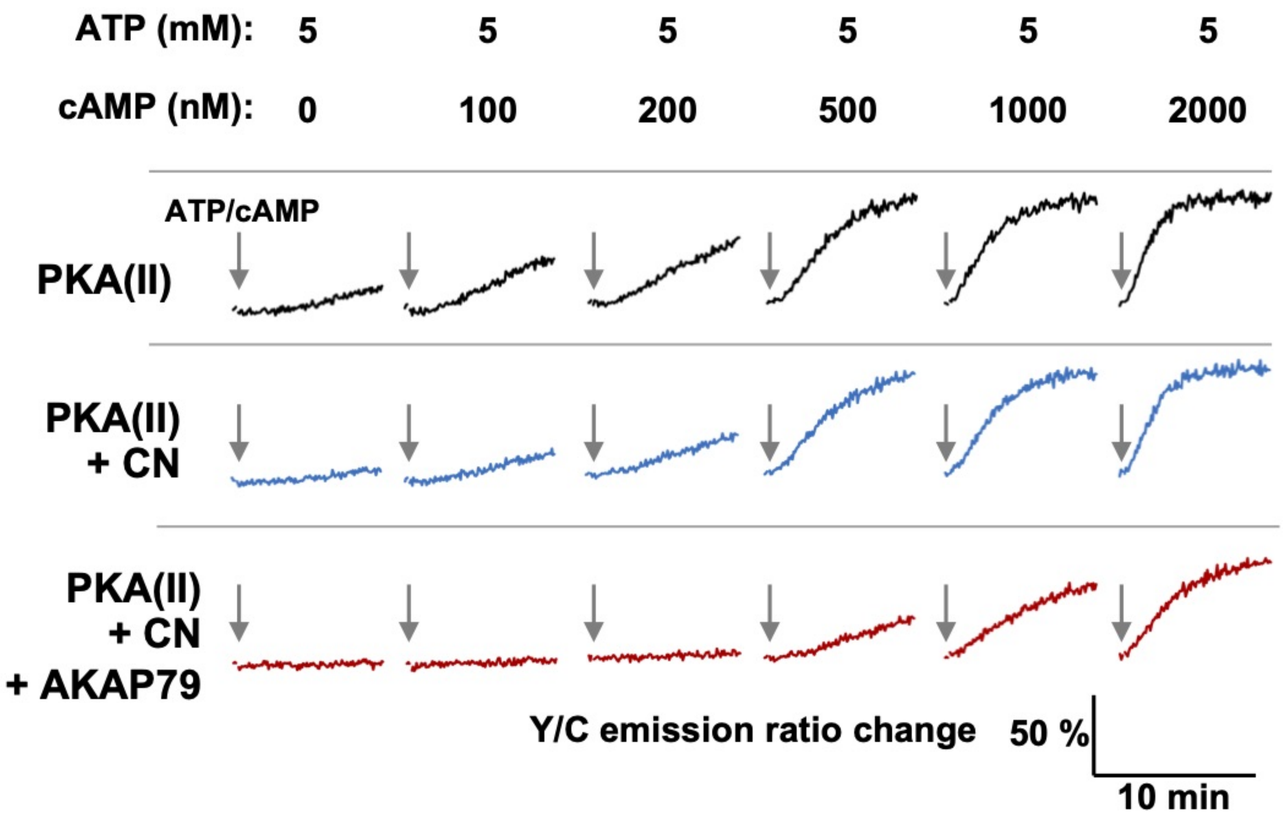

D

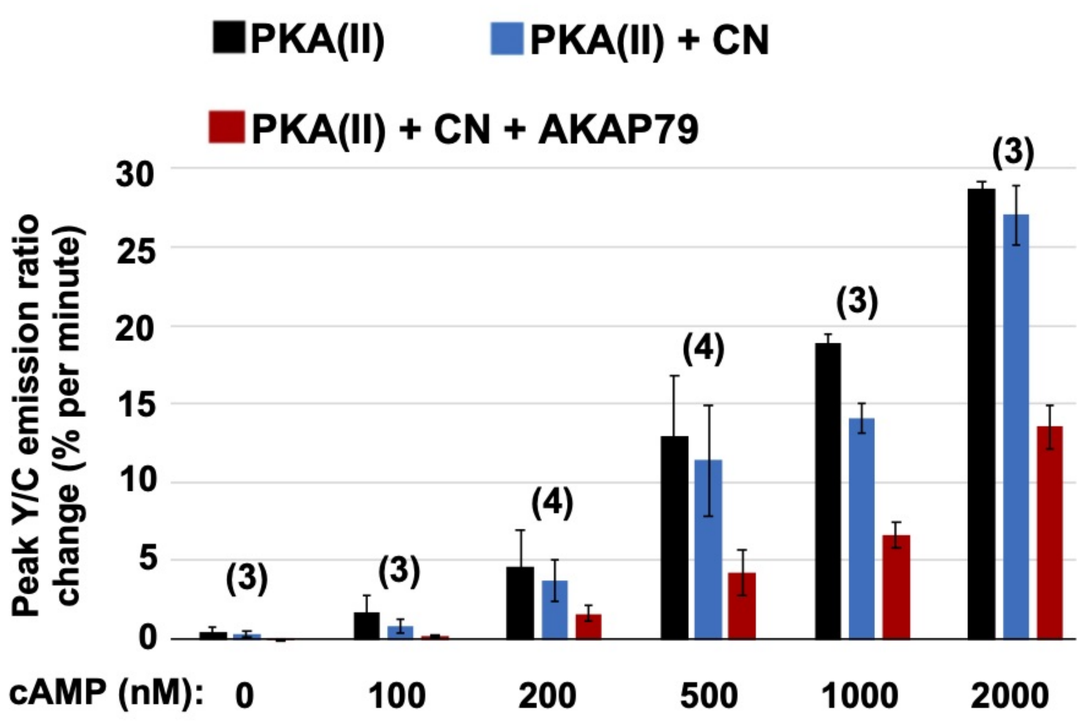

E

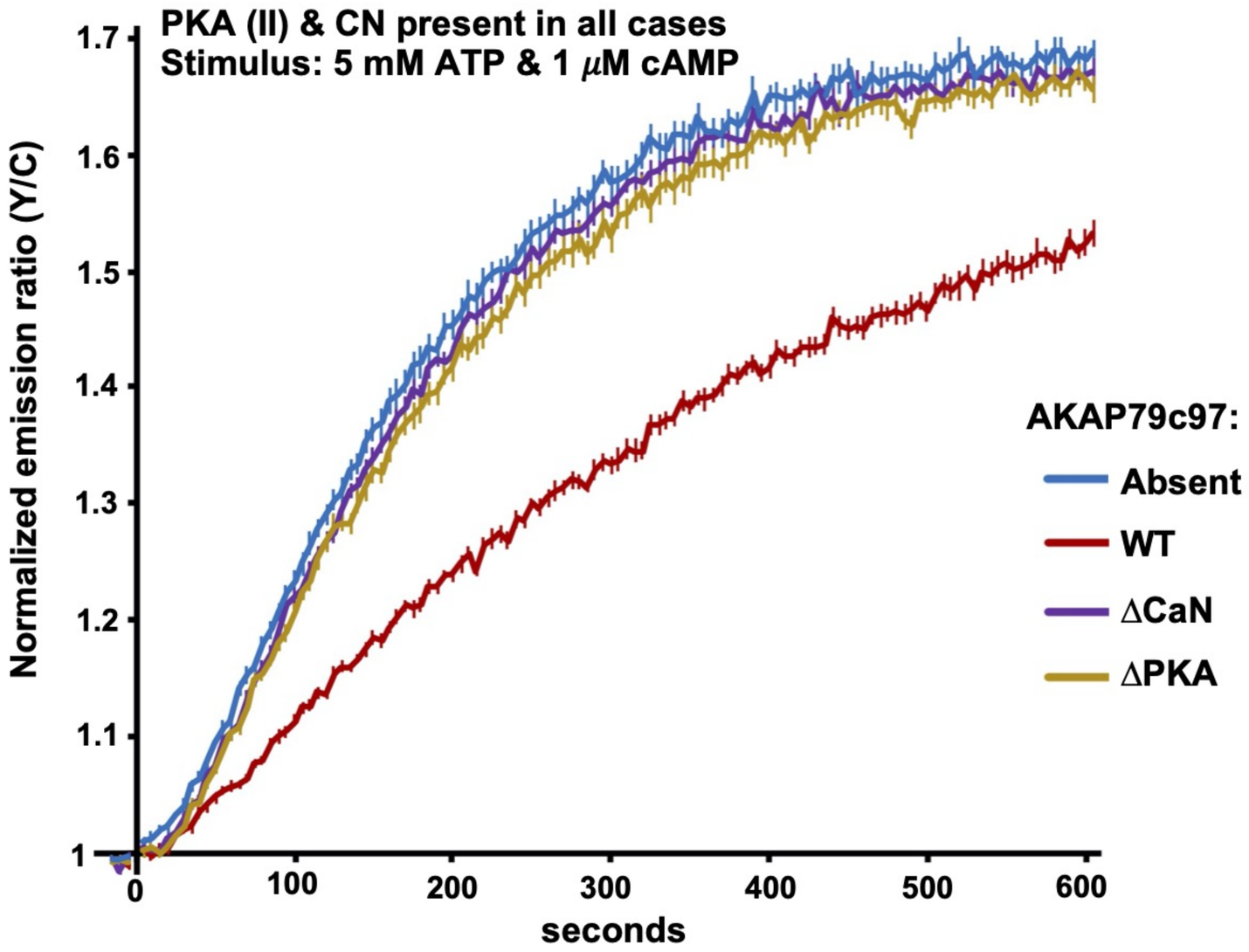

F

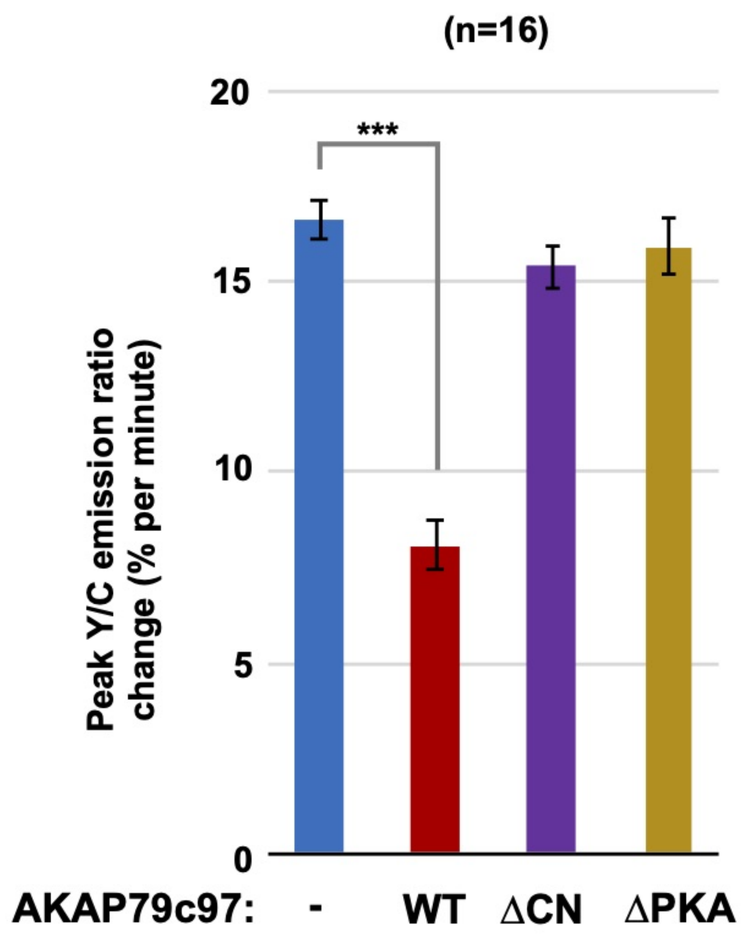

Figure 3

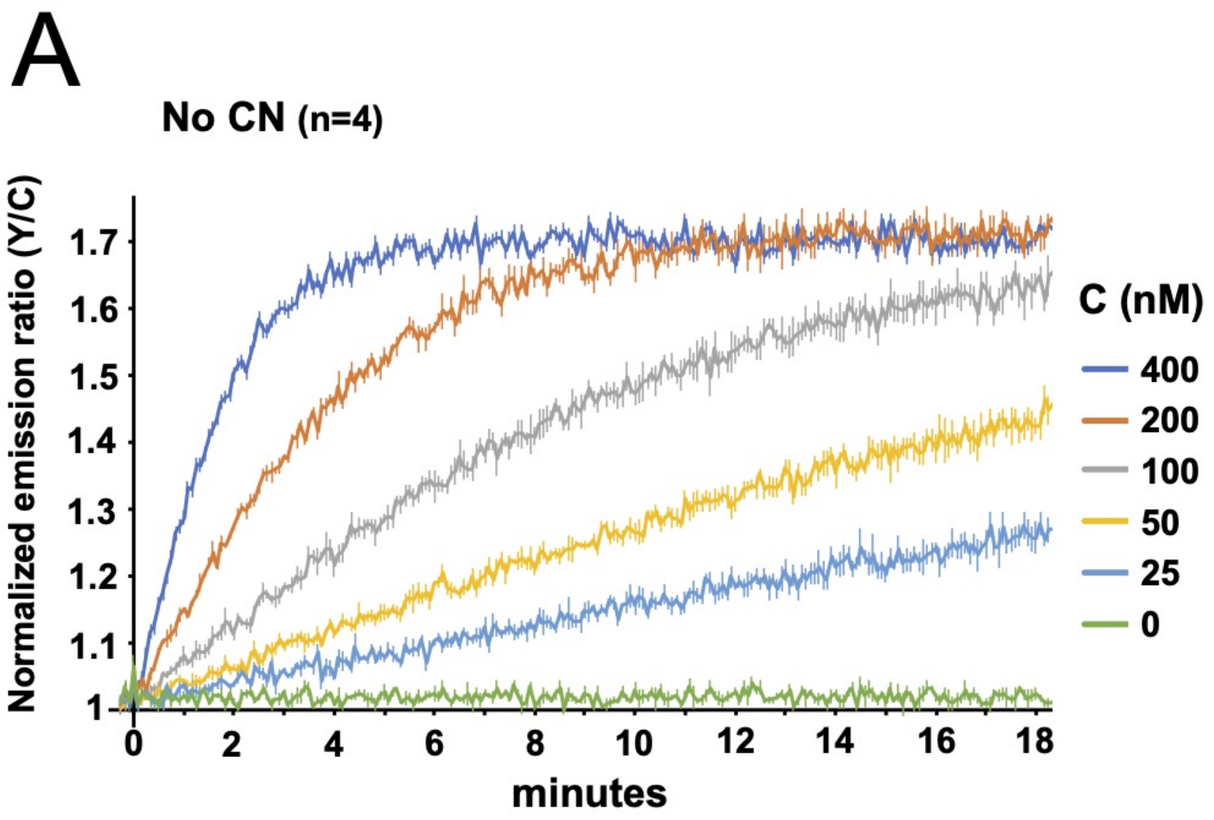

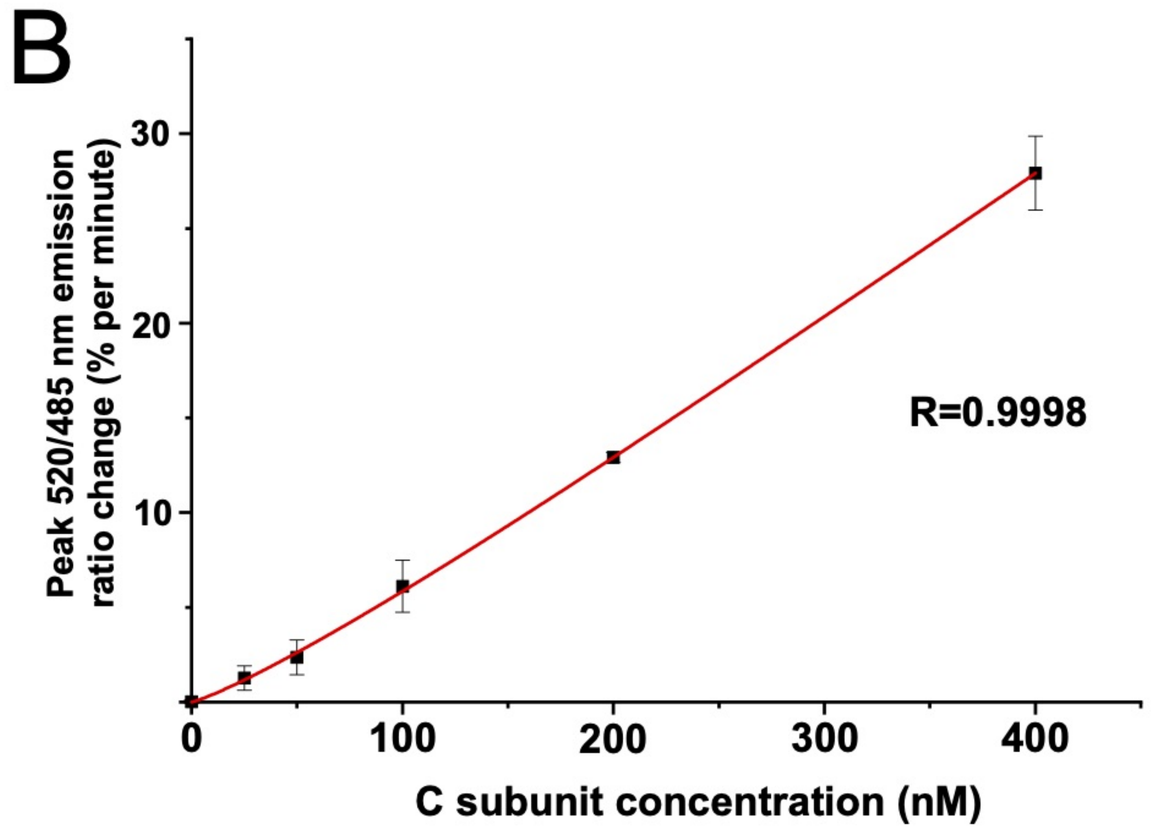

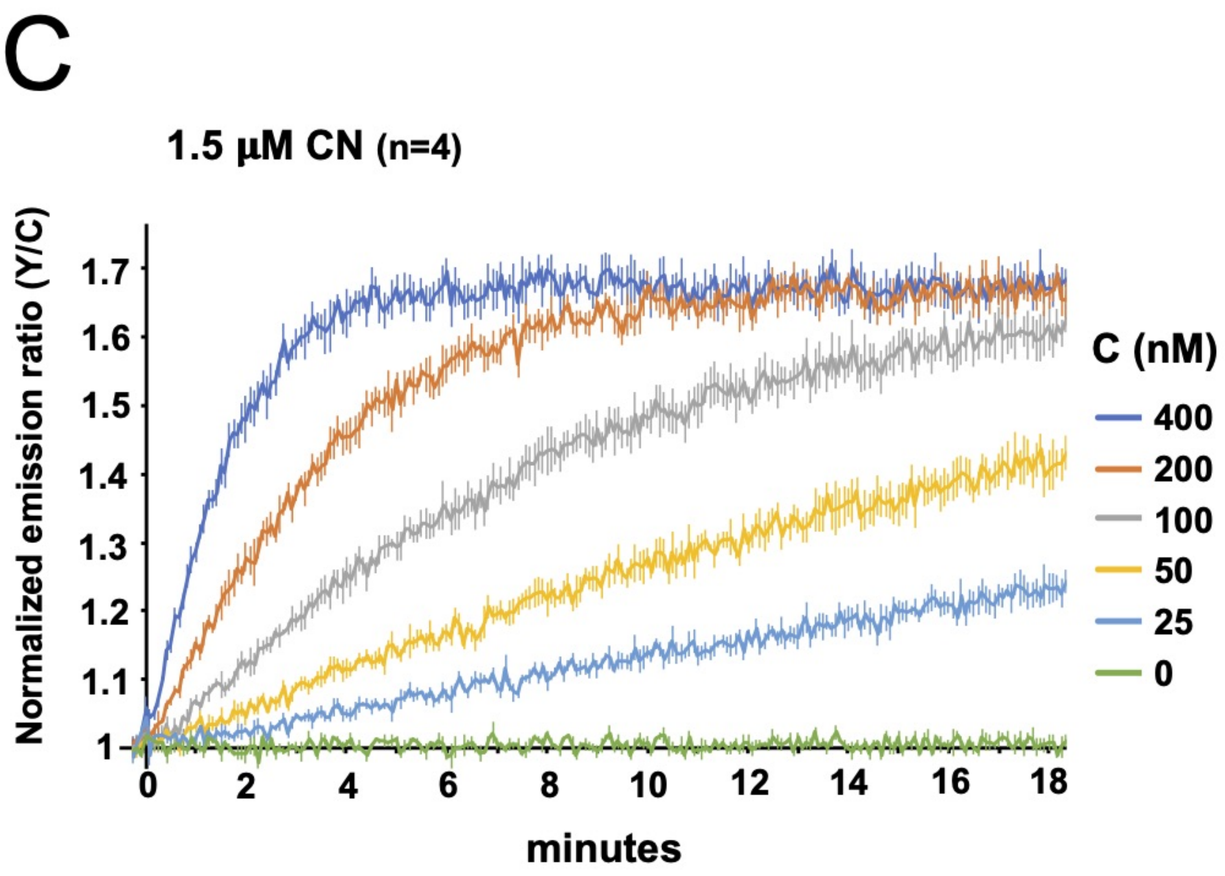

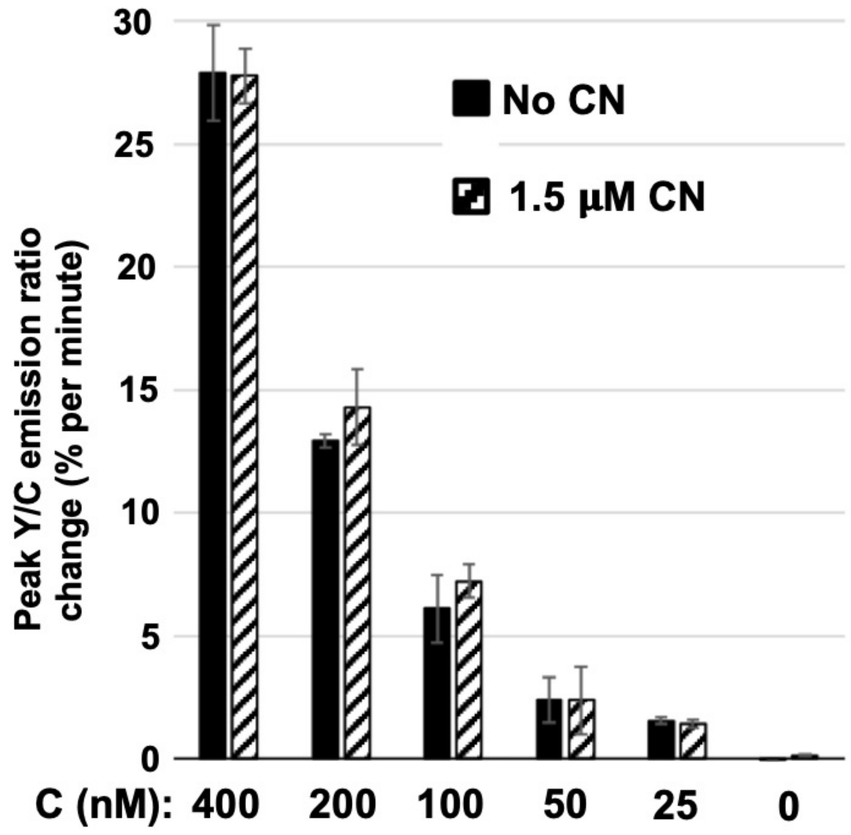

E **Maximal 520/485 nm emission ratio changes (% change min^{-1})**

	cAMP Concentration (nM)					
	0	**100**	**200**	**500**	**1000**	**2000**
Type II PKA only	0.46±0.33 (n=3)	1.67±1.11 (n=3)	4.58±3.40 (n=4)	12.92±5.51 (n=4)	20.31±0.63 (n=9)	28.70±0.49 (n=3)
Type II PKA + CN	0.34±0.15 (n=3)	0.78±0.44 (n=3)	3.75±1.93 (n=4)	11.39±4.94 (n=4)	16.26±0.48 (n=19)	27.04±1.88 (n=3)
Type II PKA + CN + AKAP79$_{c97}$	0.00±0.03 (n=3)	0.19±0.10 (n=3)	1.63±0.68 (n=4)	4.28±2.05 (n=4)	7.67±0.32 (n=25)	13.52±1.34 (n=3)

Figure 3-figure supplement 1

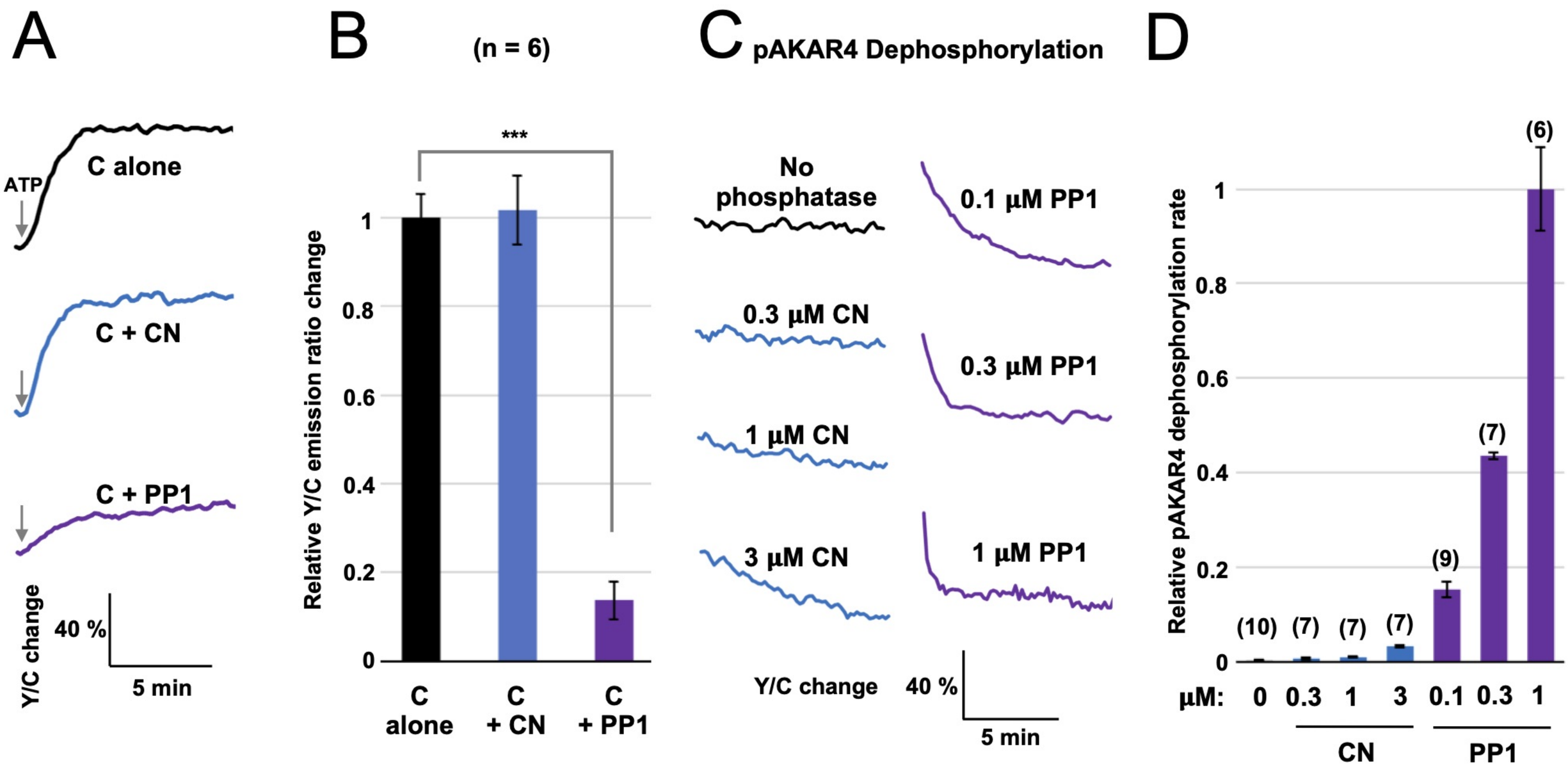

Figure 3-figure supplement 2.

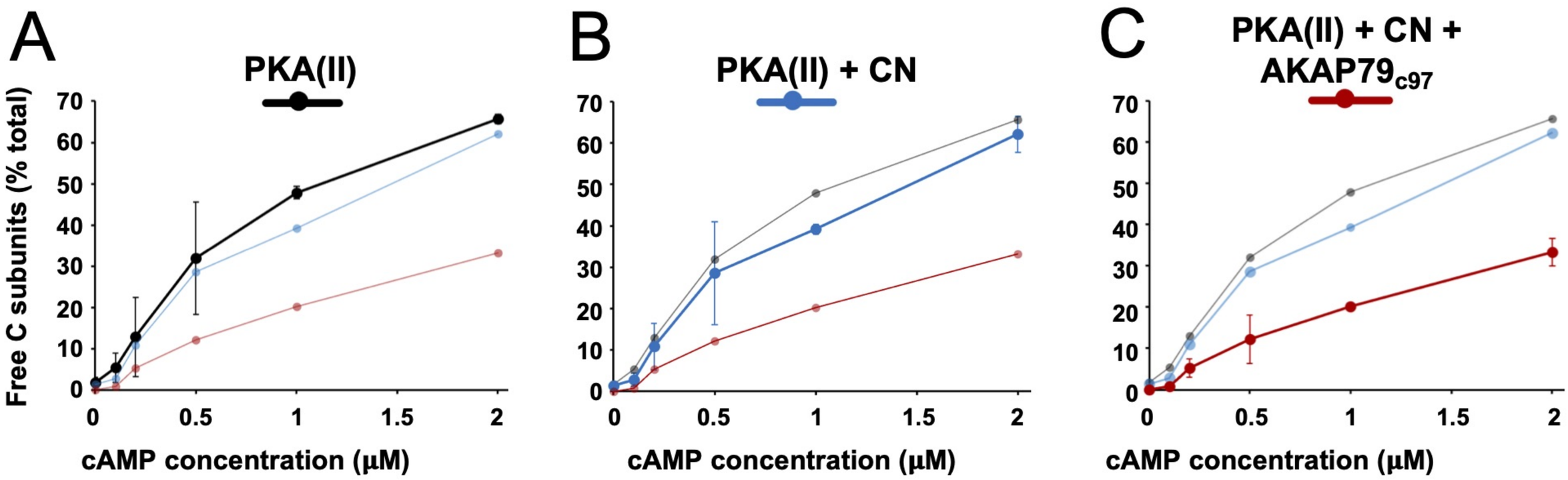
A
PKA(II)
Free C subunits (% total)
cAMP concentration (µM)
B
PKA(II) + CN
cAMP concentration (µM)
C
PKA(II) + CN + AKAP79c97
cAMP concentration (µM)

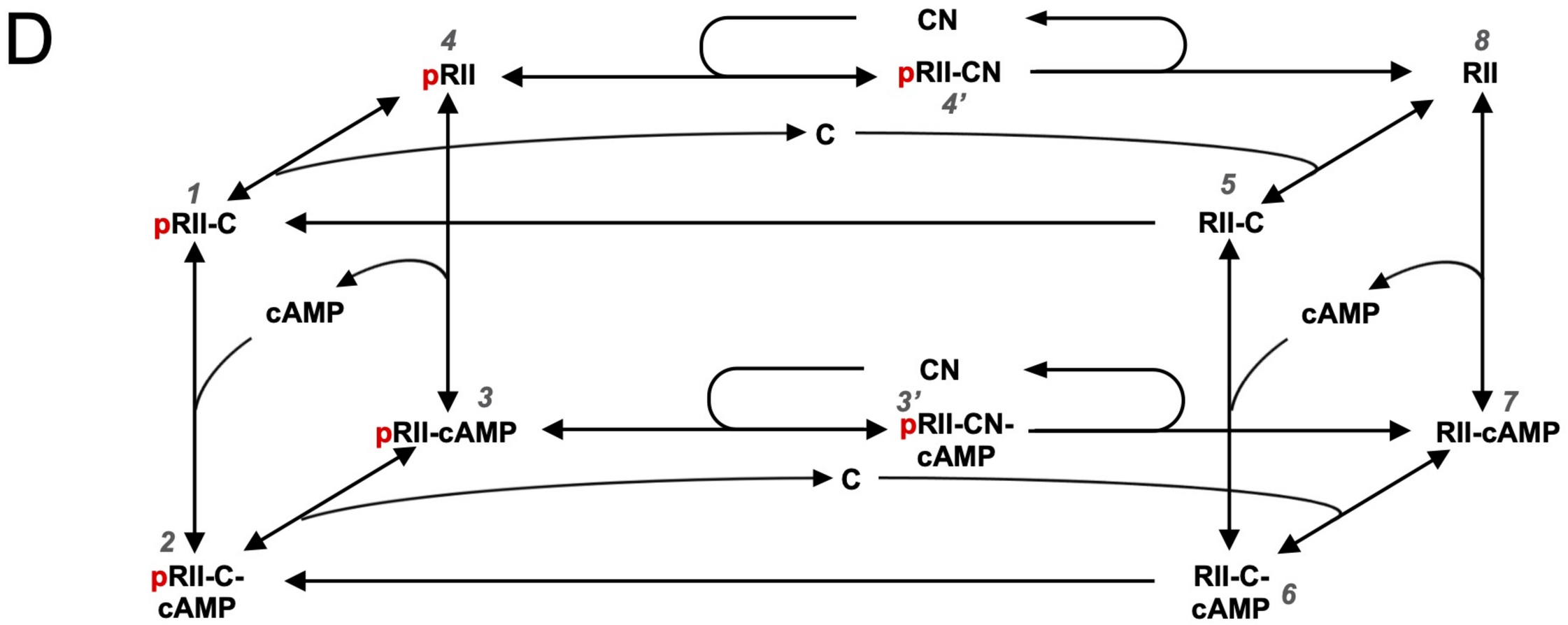
D
4
pRII
CN
pRII-CN
8
RII
4'
C
1
pRII-C
5
RII-C
cAMP
cAMP
CN
3
pRII-cAMP
3'
pRII-CN-cAMP
7
RII-cAMP
C
2
pRII-C-cAMP
RII-C-cAMP
6

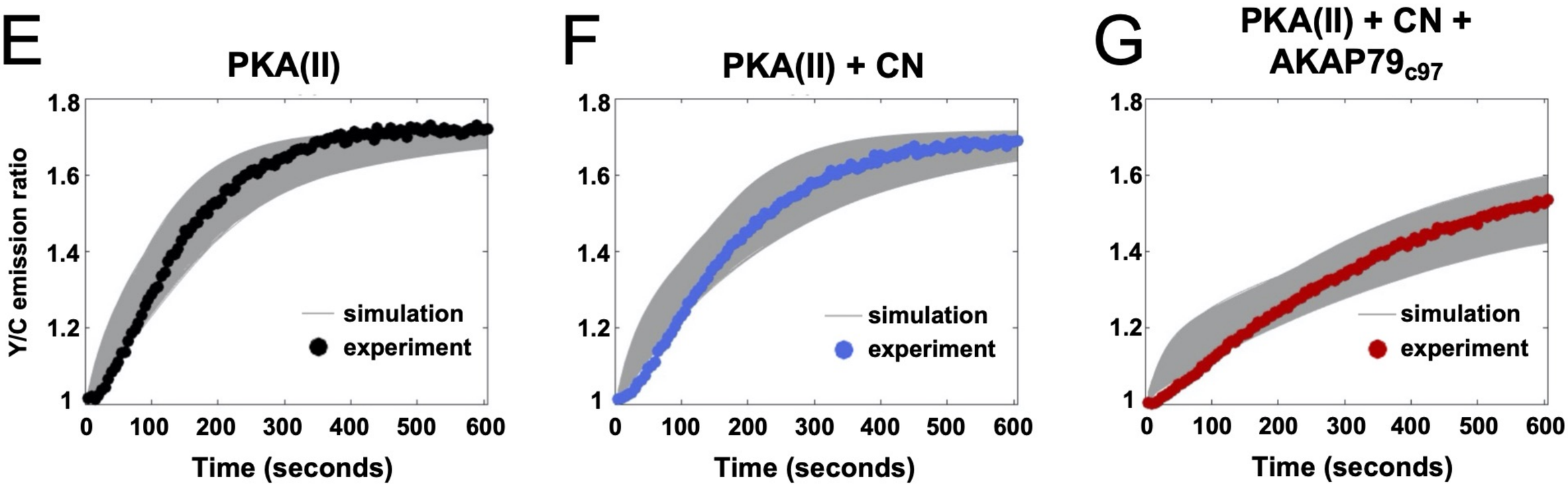
E
PKA(II)
F
PKA(II) + CN
G
PKA(II) + CN + AKAP79c97
Y/C emission ratio
simulation
experiment
Time (seconds)

Figure 4

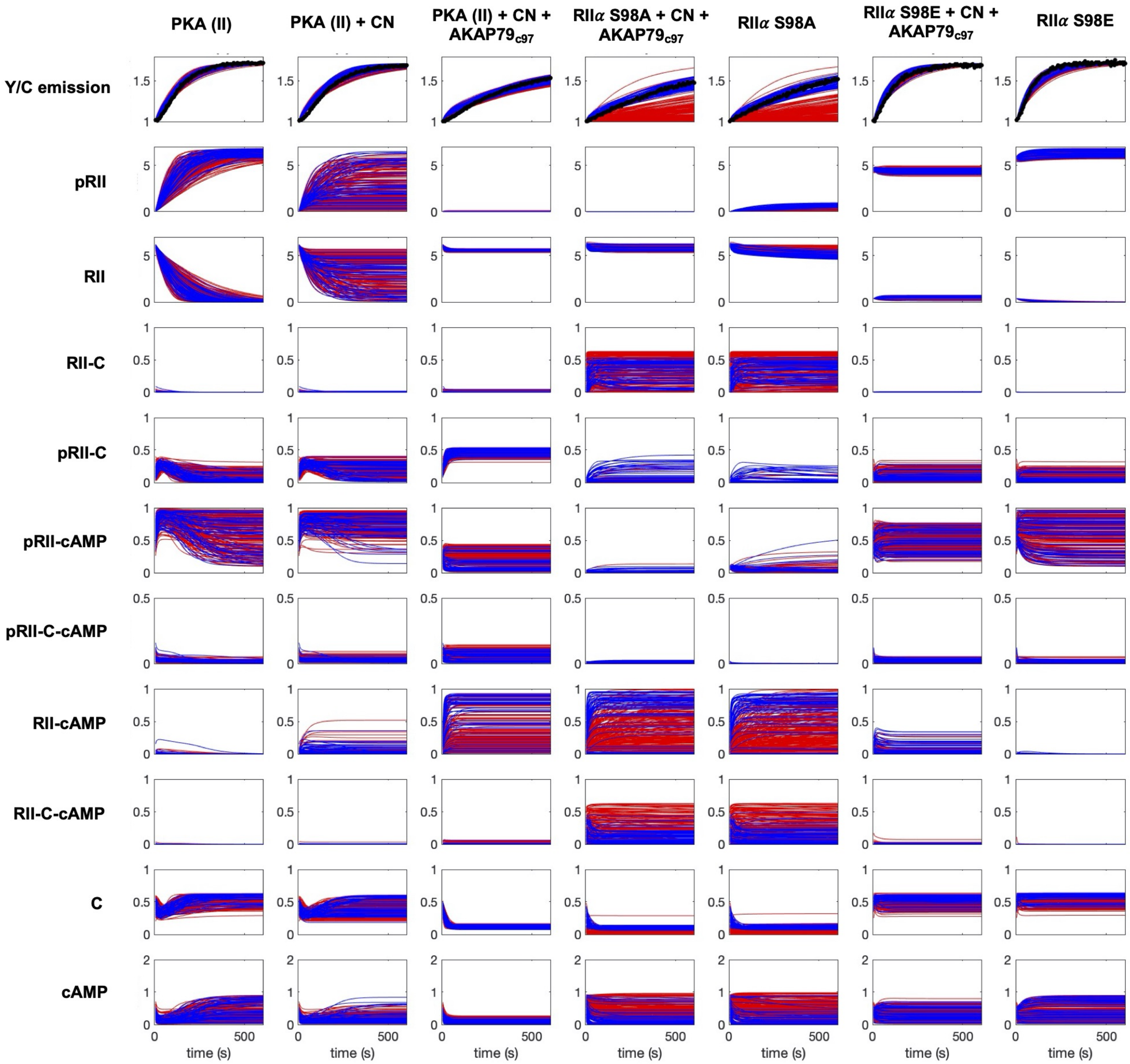

Fit Criteria

Parameter sets fitting all bar RIIα S98A data

Parameter sets fitting all data

Figure 4-figure supplement 1

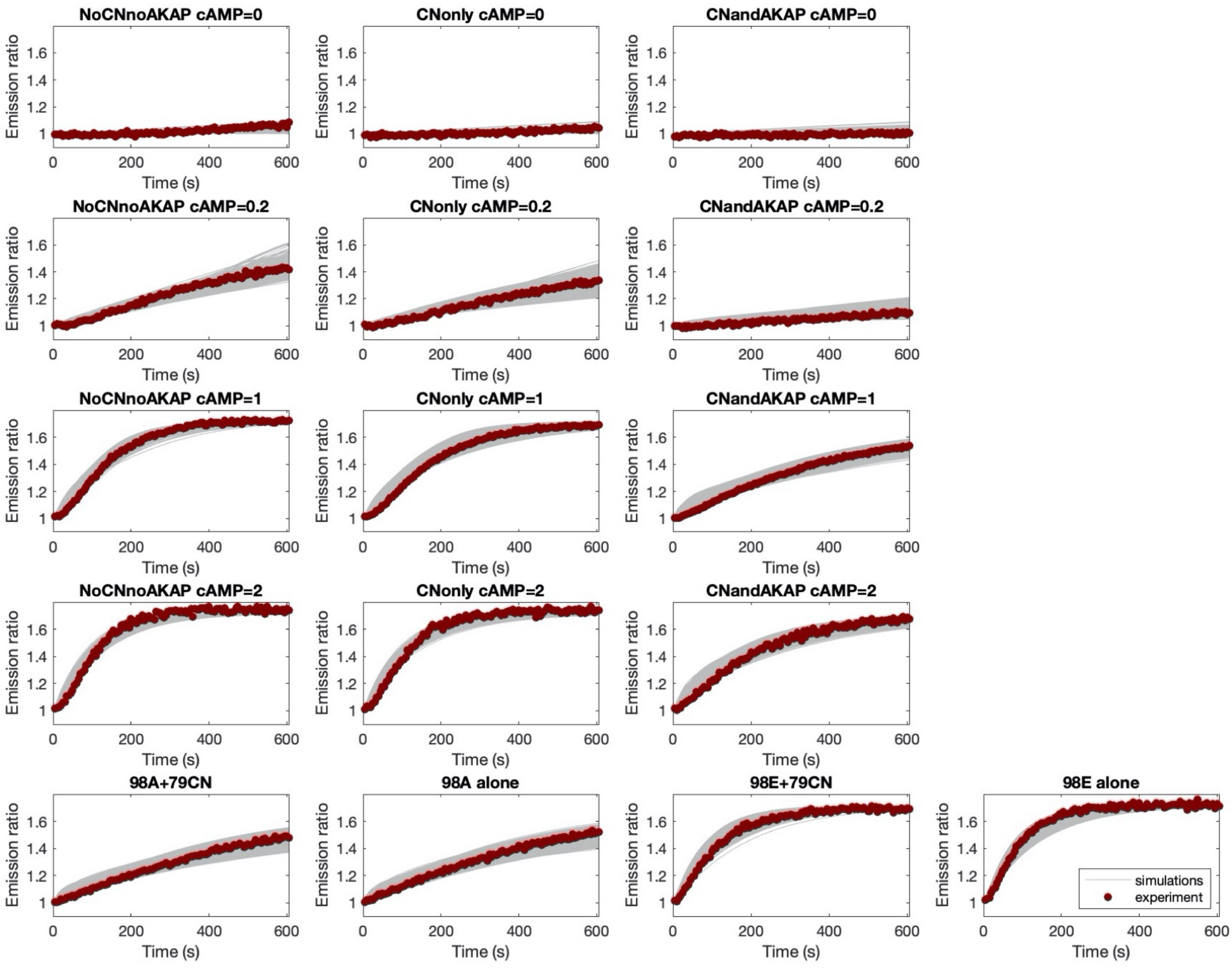

Figure 4-figure supplement 2

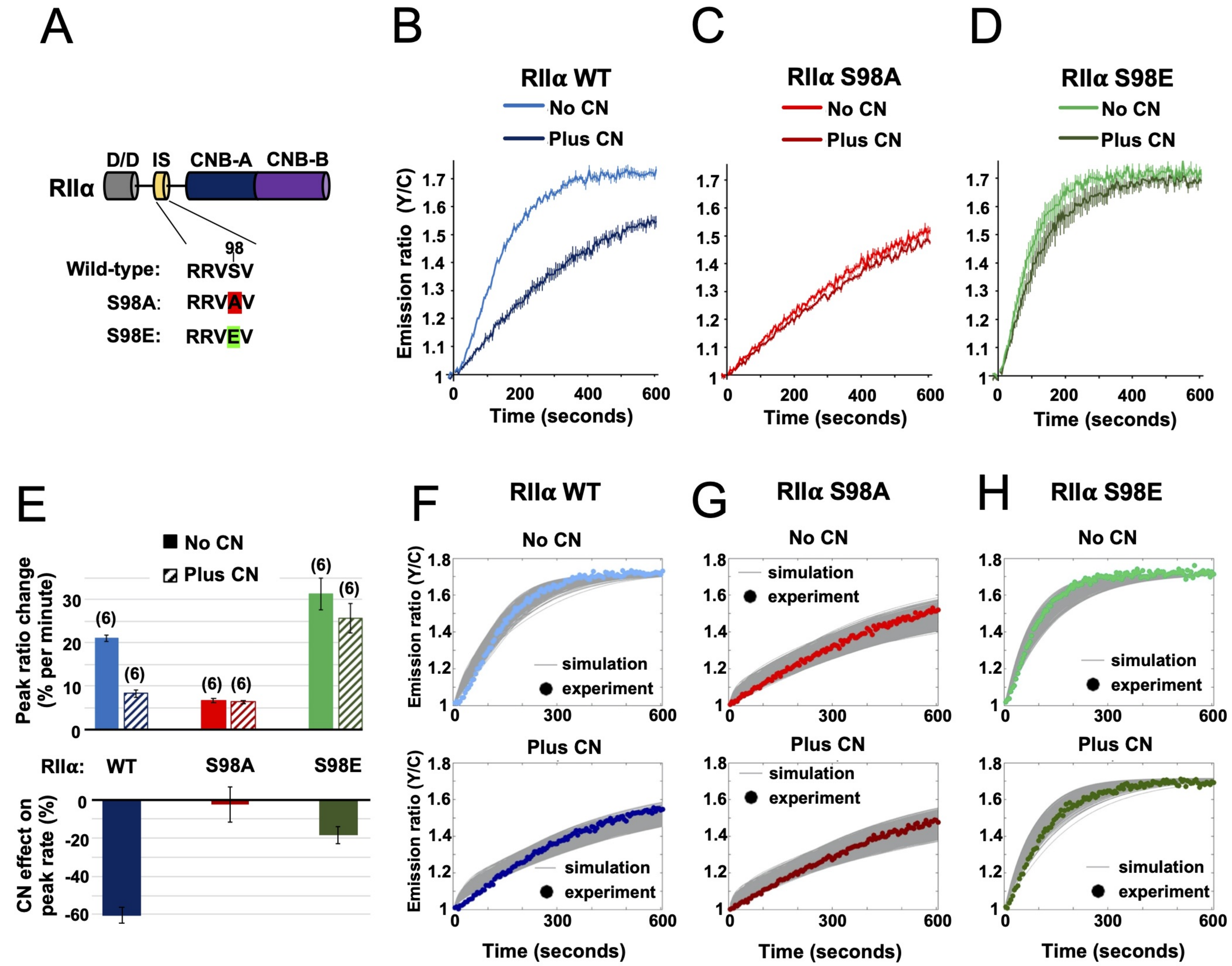
A
RIIα
D/D
IS
CNB-A
CNB-B
98
Wild-type: RRVSV
S98A: RRVAV
S98E: RRVEV
B
RIIα WT
No CN
Plus CN
Emission ratio (Y/C)
Time (seconds)
C
RIIα S98A
No CN
Plus CN
Time (seconds)
D
RIIα S98E
No CN
Plus CN
Time (seconds)
E
No CN
Plus CN
Peak ratio change (% per minute)
(6)
RIIα: WT S98A S98E
CN effect on peak rate (%)
F
RIIα WT
No CN
simulation
experiment
Plus CN
Emission ratio (Y/C)
Time (seconds)
G
RIIα S98A
No CN
simulation
experiment
Plus CN
Time (seconds)
H
RIIα S98E
No CN
simulation
experiment
Plus CN
Time (seconds)

Figure 5

A

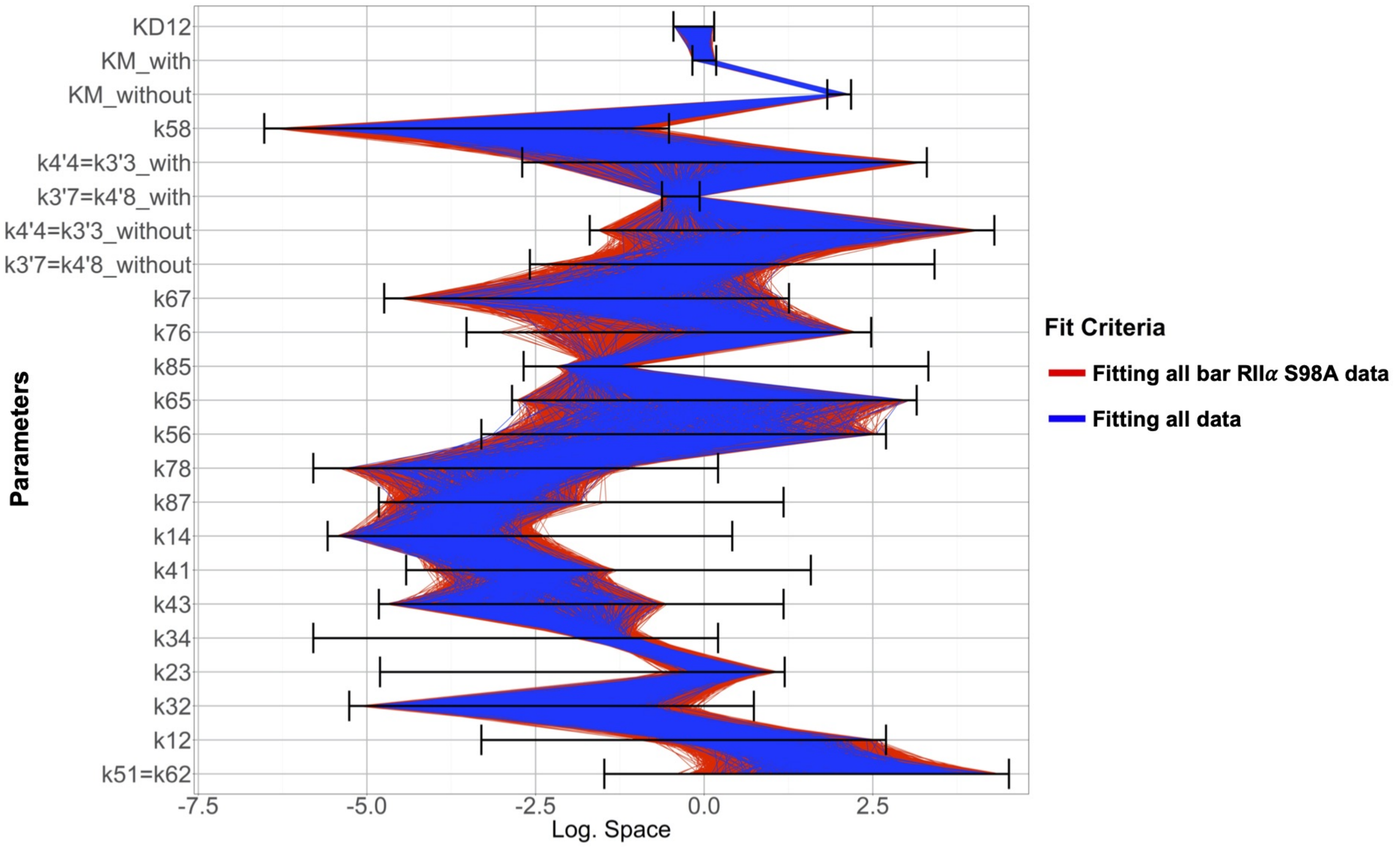

B

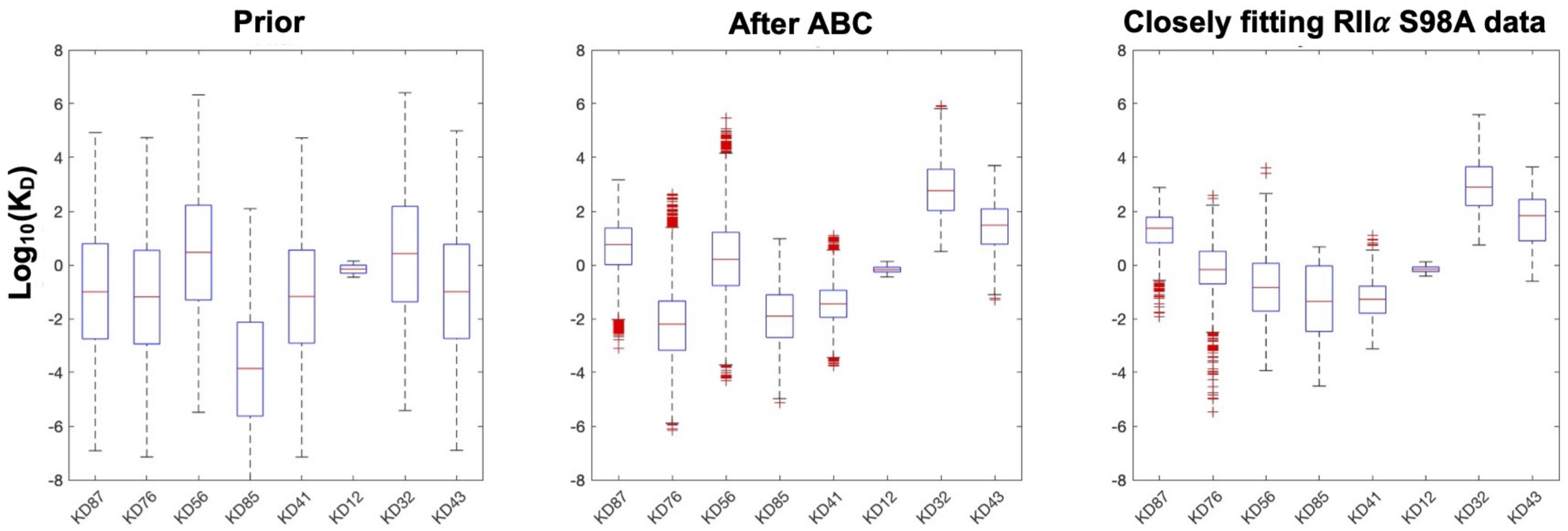

C

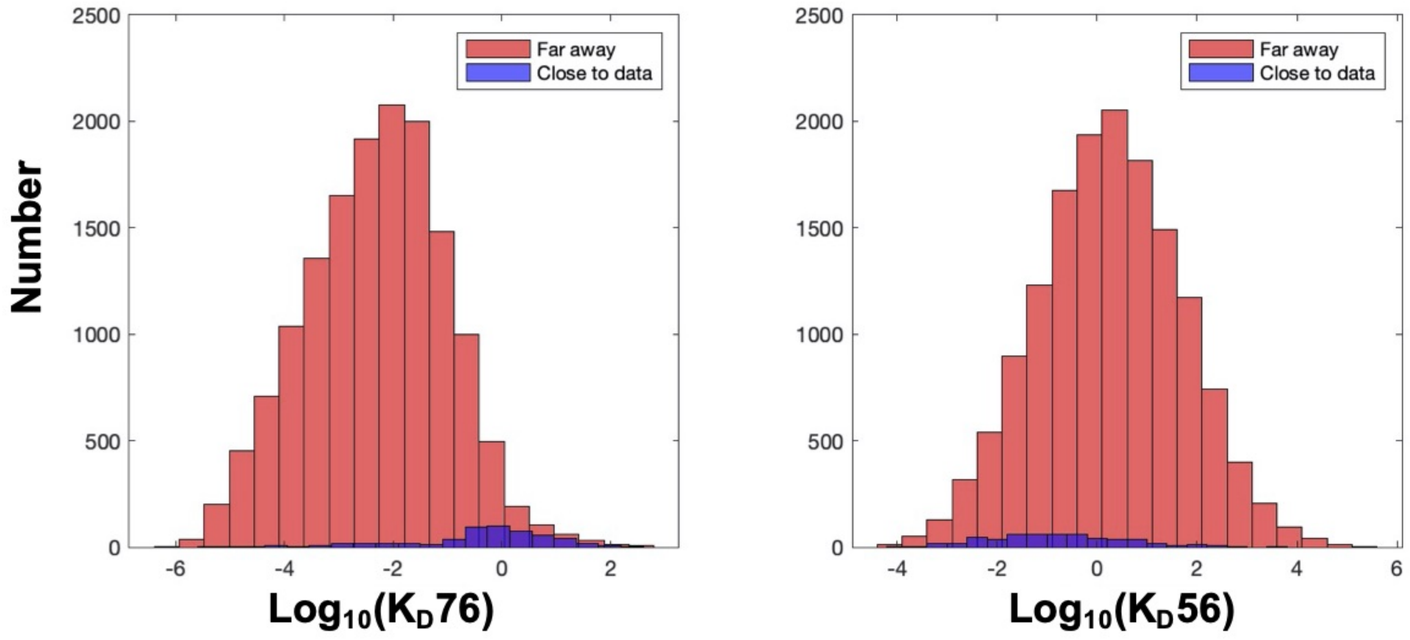

D

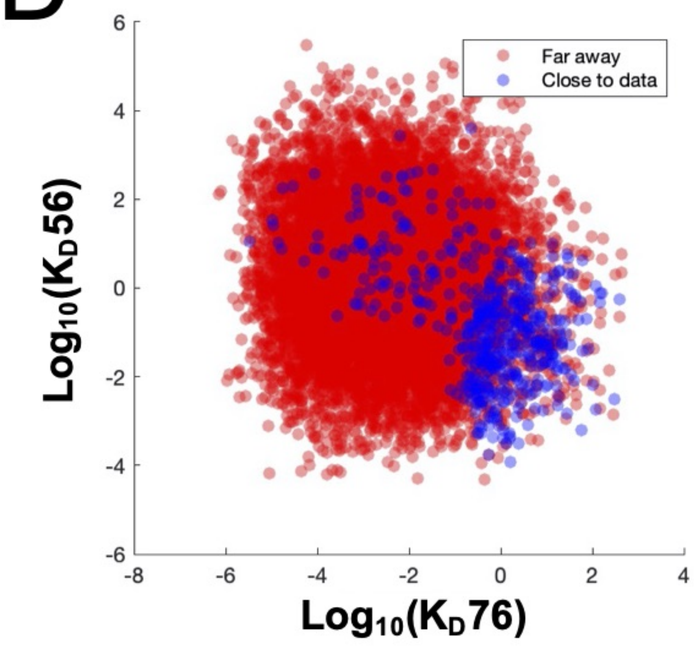

Figure 5-figure supplement 1

A

B

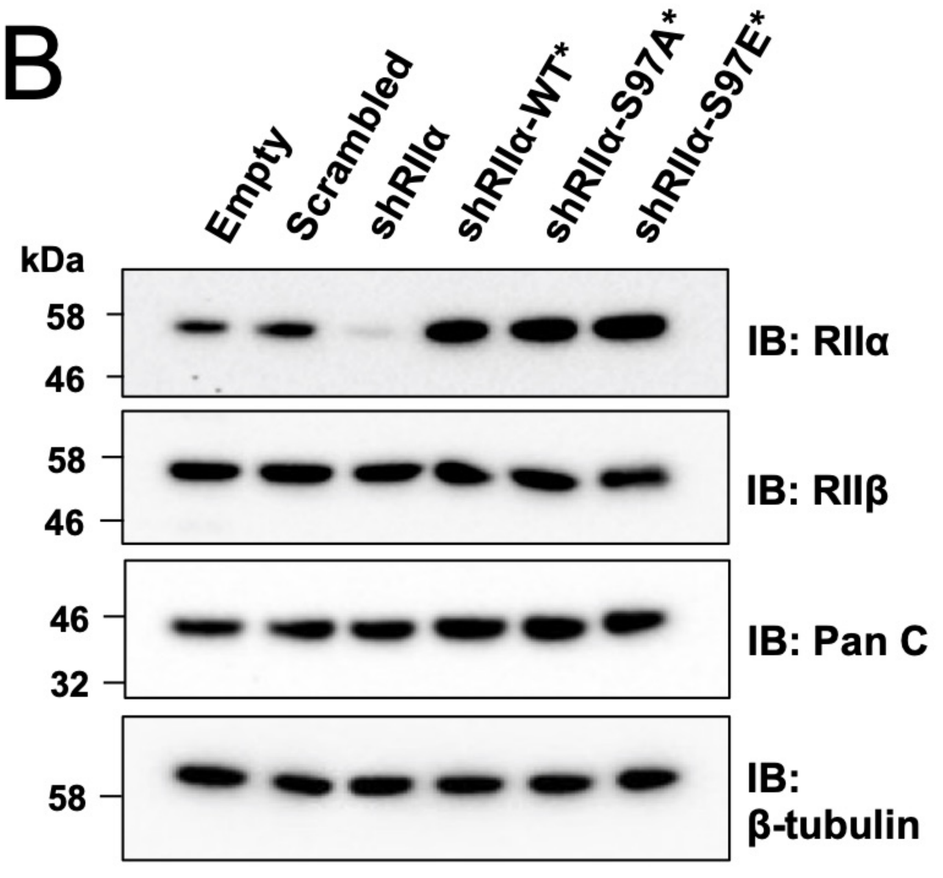

C

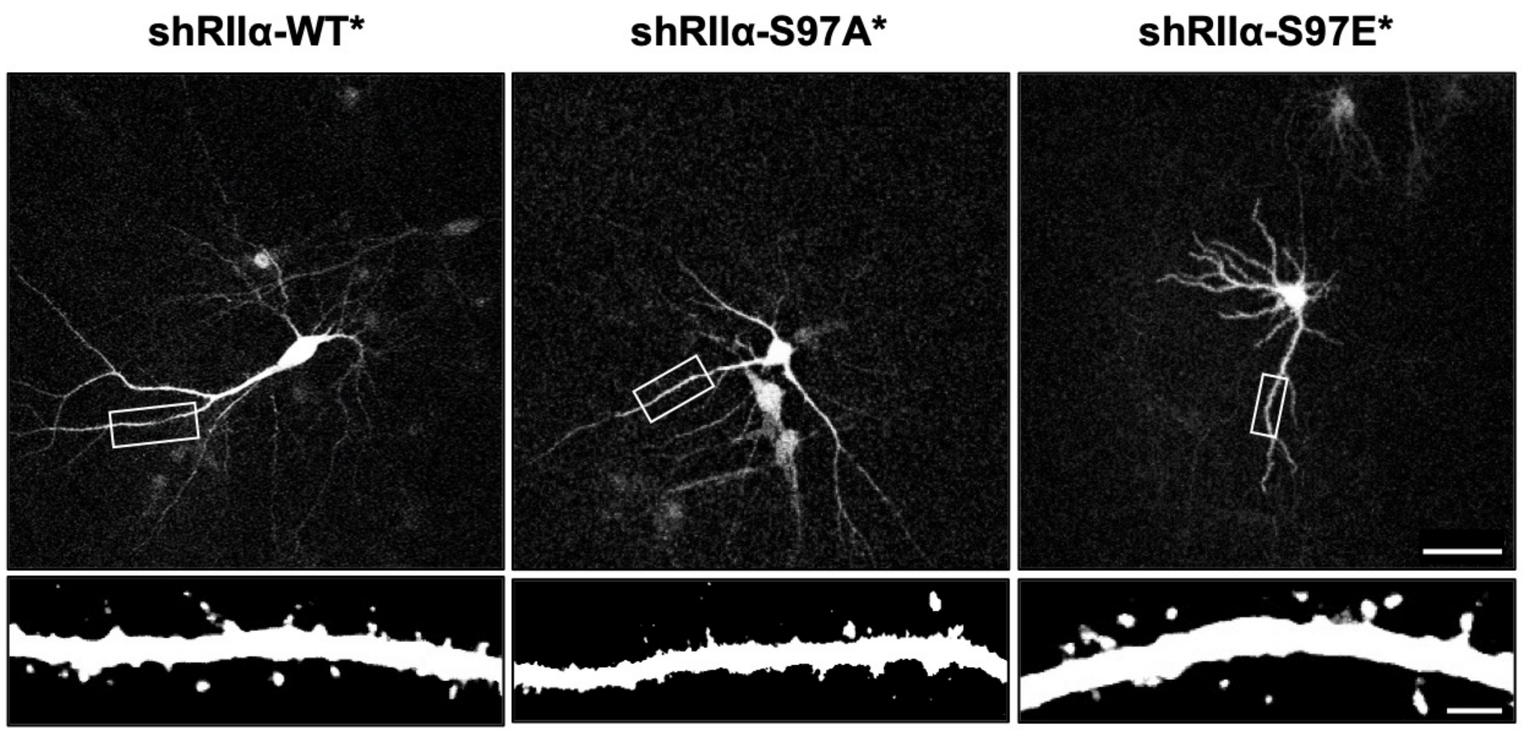

D

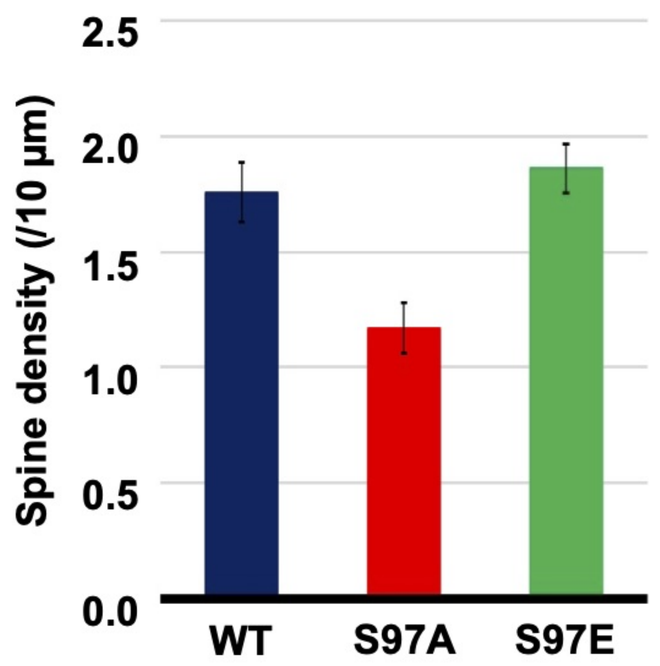

E

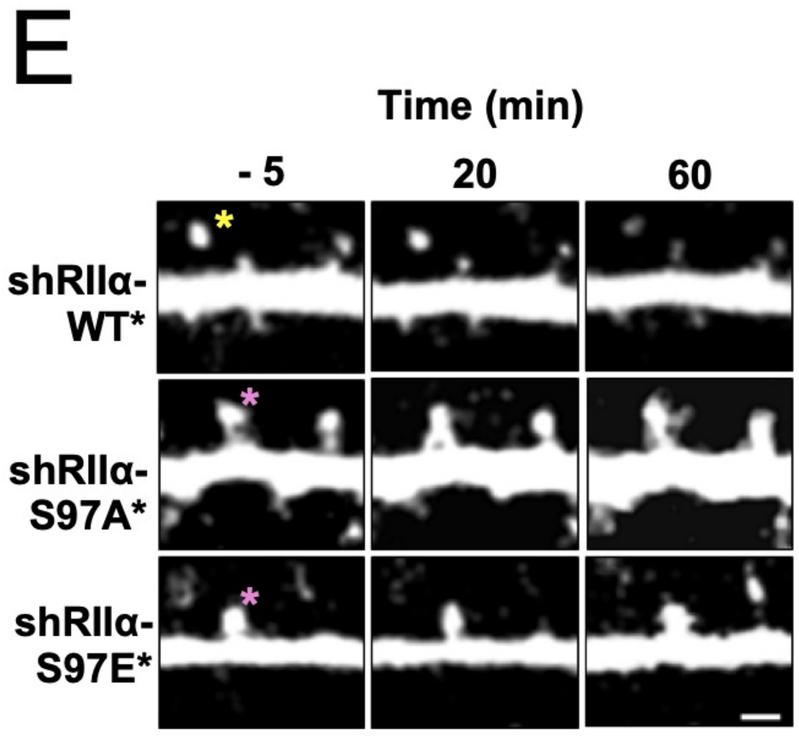

F

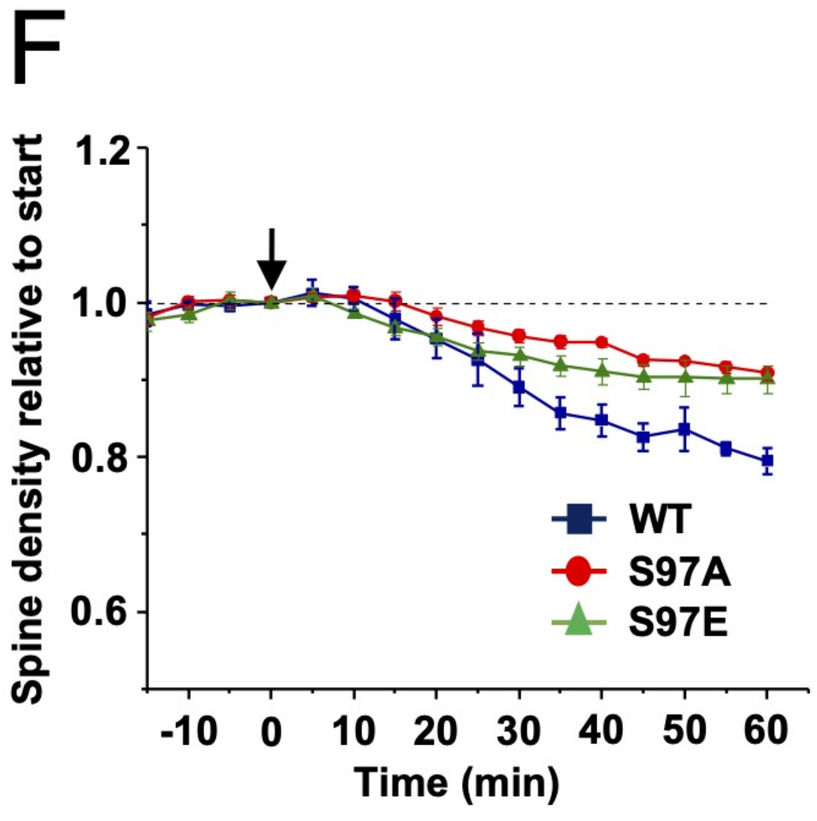

G

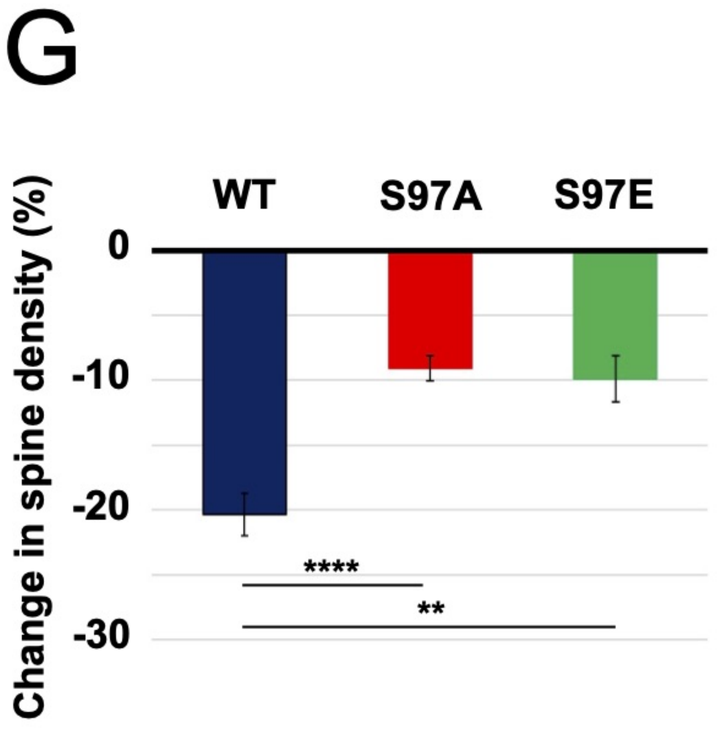

Figure 6

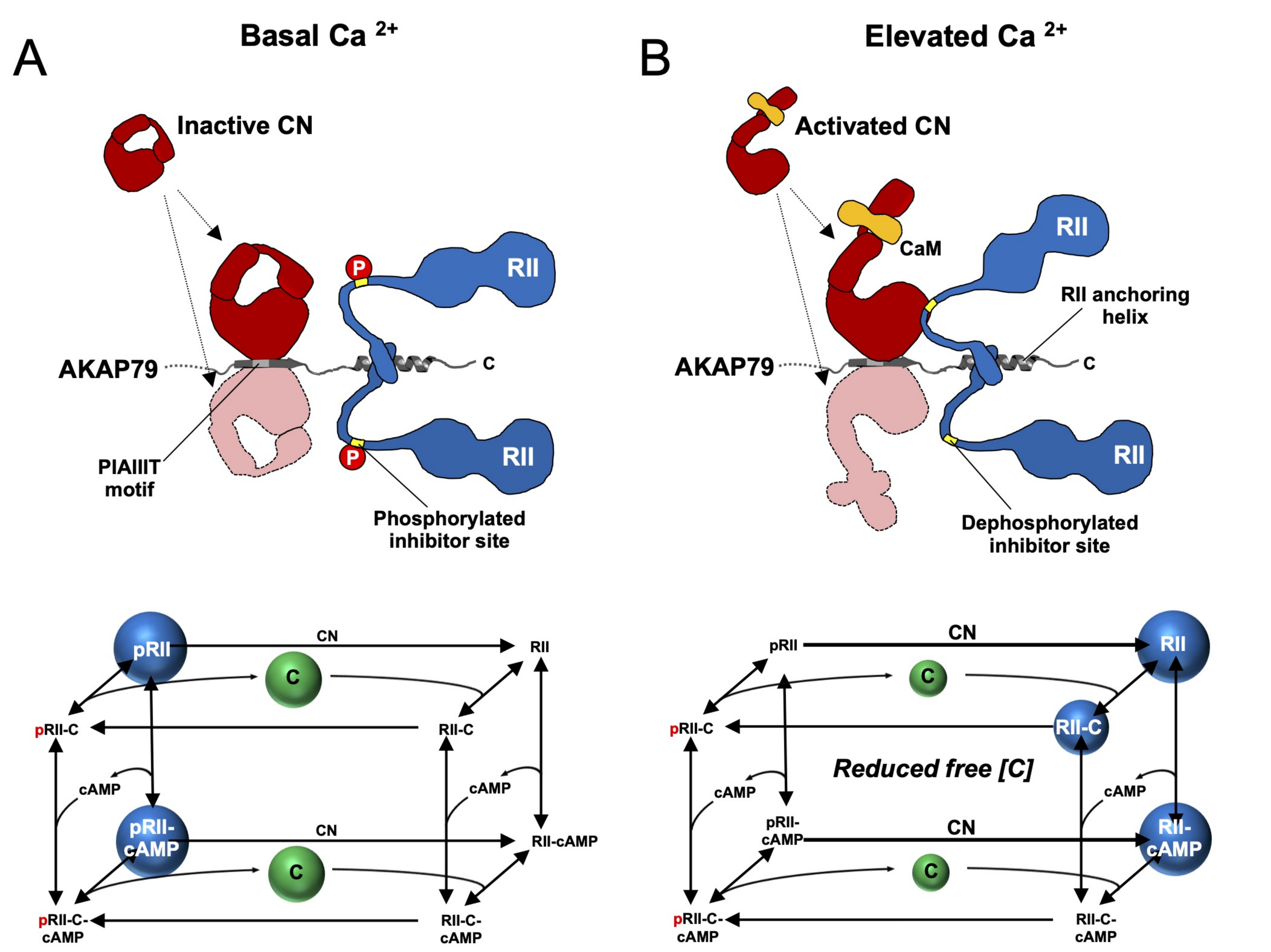
A
Basal Ca 2+
Inactive CN
AKAP79
C
RII
P
P
RII
PIAIIIT
motif
Phosphorylated
inhibitor site
B
Elevated Ca 2+
Activated CN
CaM
RII
RII anchoring
helix
AKAP79
C
RII
Dephosphorylated
inhibitor site
pRII
CN
RII
C
pRII-C
RII-C
cAMP
cAMP
pRII-
cAMP
CN
RII-cAMP
C
pRII-C-
cAMP
RII-C-
cAMP
pRII
CN
RII
C
pRII-C
RII-C
Reduced free [C]
cAMP
cAMP
pRII-
cAMP
CN
RII-
cAMP
C
pRII-C-
cAMP
RII-C-
cAMP

Figure 7